


Spring 5-13-2017

Feasibility of using 3D printed molds for thermoforming thermoplastic composites

Sunil Bhandari

University of Maine, sunil.bhandari@maine.edu

Follow this and additional works at: <http://digitalcommons.library.umaine.edu/etd>

 Part of the [Civil Engineering Commons](#), [Computer-Aided Engineering and Design Commons](#), [Manufacturing Commons](#), and the [Polymer and Organic Materials Commons](#)

Recommended Citation

Bhandari, Sunil, "Feasibility of using 3D printed molds for thermoforming thermoplastic composites" (2017). *Electronic Theses and Dissertations*. 2655.

<http://digitalcommons.library.umaine.edu/etd/2655>

This Open-Access Thesis is brought to you for free and open access by DigitalCommons@UMaine. It has been accepted for inclusion in Electronic Theses and Dissertations by an authorized administrator of DigitalCommons@UMaine.

**FEASIBILITY OF USING 3D PRINTED MOLDS FOR
THERMOFORMING THERMOPLASTIC
COMPOSITES**

By

Sunil Bhandari

A THESIS

Submitted in Partial Fulfillment of the
Requirements for the Degree of
Master of Science
(in Civil Engineering)

The Graduate School
The University of Maine

May 2017

Advisory Committee:

Roberto A. Lopez-Anido, Professor of Civil Engineering, Advisor

William G. Davids, Professor of Civil Engineering

Douglas J. Gardner, Professor of Forest Operations, Bioproducts, & Bioenergy

**FEASIBILITY OF USING 3D PRINTED MOLDS FOR
THERMOFORMING THERMOPLASTIC
COMPOSITES**

By Sunil Bhandari

Thesis Advisor:

Dr. Roberto A. Lopez-Anido

An Abstract of the Thesis Presented in
Partial Fulfillment of the Requirements for the
Degree of Master of Science
(in Civil Engineering)
May, 2017

This thesis presents a novel combined experimental and numerical mechanics approach for characterizing 3D printed thermoplastic materials by the fused deposition modeling process for thermoforming thermoplastic composites. The implications of this work are:

- a. a methodology for model-based performance evaluation of 3D printed structural parts,
and
- b. an improved design of 3D printed molds for composites manufacturing, which has
potential for material innovations and scaled-up applications in additive manufacturing.

The thesis formulates basic criteria for selection of thermoplastic polymer used for the 3D printed mold based on forming temperatures. The thesis creates a lattice and shell finite element model of the 3D printed part to characterize its linear elastic mechanical properties and validates this model by mechanical experiments on 3D printed coupons. The thesis studies the

thermomechanical and creep properties of a 3D printed polymer and implications of these behaviors on mold making. The thesis creates an idealized orthotropic solid finite element model for the lattice internal structure of 3D printed parts. The mechanical properties of this orthotropic solid are obtained from the virtual experiments carried out on the lattice and shell finite element model. This orthotropic solid finite element model is validated through mechanical experiment on 3D printed molds subjected to forming pressures. Finally, an optimization technique is outlined to create an optimal internal structure for the 3D printed polymer part.

ACKNOWLEDGEMENTS

I would like to thank my advisor and thesis committee for providing insight and direction for my work. This research was made possible by a grant from NIST Advanced Manufacturing Technology Consortia (AMTech) program, titled “Consortium for Manufacturing Innovation in Structural Thermoplastics (CMIST), Award No. 70NANB15H075. I would also like to thank the College of Engineering for awarding Correll Fellowship for the first year of my study and the University of Maine Graduate School for awarding Graduate Trustee Tuition Scholarship for the second year of my study. I would like to express a very heartfelt gratitude to Mr. David Erb at the Advanced Structures and Composites Center at University of Maine for his support, guidance, and suggestions during the research work. Finally, I would like to thank the staff and the students at Advanced Structures and Composites Center at the University of Maine for their help and guidance.

TABLE OF CONTENTS

ACKNOWLEDGEMENTS	ii
LIST OF TABLES	viii
LIST OF FIGURES	ix
CHAPTER 1: INTRODUCTION	1
1.1 Research Objectives	2
1.2 A discussion on terminology used	3
1.2.1 3D Printing	4
1.2.2 Fused Deposition Modeling.....	4
1.3 Time and cost required for manufacture of different molds	5
1.4 3D Printing Methods.....	7
1.5 Open Systems versus Closed Systems	9
1.6 Thermoplastic Composites Manufacturing.....	10
1.7 Organization of the Thesis Chapters.....	15
CHAPTER 2: 3D PRINTING AND MOLD MATERIAL SELECTION	16
2.1 Introduction.....	16
2.2 3D printing Process.....	17
2.3 Components of a 3D printer.....	17
2.4 Steps involved in 3D printing	20
2.5 The calibration process for 3D printer table and extruder head.....	26
2.6 Experimentation for proof of concept.....	27
2.6.1 The Mold	27
2.6.2 Material and Laminate Preparation	28

2.6.3 Heating Apparatus	31
2.6.4 Press	32
2.6.5 Procedure for forming the part	33
2.6.6 Thermoforming Results	34
2.6.7 Conclusions	36
2.7 Mold Material selection	37
2.7.1 Available materials and their properties	42
2.8 Conclusions.....	45
 CHAPTER 3: MOLD INTERNAL STRUCTURE AND QUASI-STATIC	
PROPERTIES	46
3.1 Internal Structure of the mold	46
3.2 Quasi static tests.....	48
3.2.1 Tension tests of the filament.....	49
3.2.2 Tension Tests of the printed material	51
3.2.3 Compression tests of the 3D printed test coupons.....	53
3.2.4 Shear tests of 3D printed specimens.....	53
3.2.5 Compression Tests of solid specimens	54
3.3 Experimental Results	58
3.3.1 Quasi Static Tests of samples with lattice internal structure	58
3.3.2 Quasi-static compression test of specimen with solid internal structure.....	58
3.3.3 Tension test of filaments.....	59
3.4 Discussion of Results.....	60
3.5 Conclusions.....	70

CHAPTER 4: CREEP AND THERMAL PROPERTIES	72
4.1 Theory	72
4.1.1 Mechanical Behavior of polymers with respect to temperature	72
4.1.2 Mechanical Behavior of polymers with respect to sustained loading	73
4.2 Experimental Procedure.....	77
4.2.1 Dynamic Mechanical Thermal Analysis (DMTA) of filaments to determine glass transition temperature	77
4.2.2 Creep tests of samples with lattice internal structure	78
4.3 Discussion of results	80
4.4 Determination of Creep parameters	84
4.5 Conclusions and recommendations.....	86
 CHAPTER 5: FINITE ELEMENT MODELING FOR ELASTIC RESPONSE OF 3D PRINTED PART WITH LATTICE INTERNAL STRUCTURE.....	 88
5.1 Finite Element Model	88
5.1.1 Symmetry and Boundary Conditions.....	90
5.1.2 Materials	90
5.1.3 Geometry and Sections	91
5.1.4 Compression in X direction	91
5.1.5 Compression in Z direction	92
5.1.6 Tension in X direction	92
5.1.7 Tension in Z direction.....	92
5.1.8 Shear in XY plane.....	93
5.1.9 Shear in XZ plane	93

5.1.10 Assembly, elements, and meshing	93
5.2 Results.....	95
5.3 Discussion of results	102
5.4 Conclusions and recommendations.....	103
CHAPTER 6: MOLD DESIGN AND MANUFACTURE.....	105
6.1 Mold Design.....	105
6.2 Finite element model.....	110
6.2.1 Determination of material properties for the orthotropic solid.....	110
6.2.2 Properties of the part skin.....	116
6.2.3 Finite element model of the mold assembly	116
6.2.4 Experimental verification of the strains.....	121
6.2.5 Comparison of results experiments and the finite element model.....	124
6.3 Conclusions and recommendations.....	127
CHAPTER 7: CONCLUSIONS AND RECOMMENDATIONS.....	128
7.1 Material Selection for 3D Printed Mold	128
7.2 Mechanical Properties of 3D printed Lattice Structure	128
7.3 Finite Element Modeling for internal structure	129
7.4 Suggested mold design process	129
7.5 Example of mold design Optimization process	132
7.6 Recommendations for Future work	135
7.6.1 Study of factors affecting the variability in 3D printing of parts with lattice internal structure	135
7.6.2 Creating a more versatile Finite Element Model.....	136

7.6.3 Automation of the mold optimization process.....	136
7.7 Final Conclusions.....	136
REFERENCES	138
APPENDIX : MATLAB PROGRAM FILES USED FOR ANALYSIS	142
BIOGRAPHY OF THE AUTHOR.....	146

LIST OF TABLES

Table 1.1: Time and cost of creating two different mold parts using different materials and different manufacturing techniques.....	6
Table 1.2: Prices of some common thermoset polymers compared with some common thermoplastic polymers [39, 40].....	13
Table 2.1: Materials considered for thermoforming with their melting temperature.	30
Table 2.2: Materials available in Stratasys Fortus 900mc for 3D printing.....	43
Table 2.3: Compatibility of available mold polymers for Fortus 900 mc with the parts that can be thermoformed.....	44
Table 3.1: Mechanical properties from quasi-static coupon tests with COV in parenthesis.	59
Table 5.1: Comparison of Elastic Modulus from FEM and Elastic Modulus from Experiments.....	96
Table 5.2: Total cross-sectional area for compression in Z-direction.	98
Table 5.3: Poisson's ratio from FEM compared to Poisson's ratio from experimental results. ...	102
Table 6.1: Table showing the mechanical properties of the orthotropic solid used to replace the internal cellular structure for the printing parameters used.....	116
Table 7.1: Properties of the equivalent anisotropic solid when air gap is changed from 2.0 mm to 1.0 mm.	134

LIST OF FIGURES

Figure 1.1: Different Additive Manufacturing Methods [10].	9
Figure 1.2: Forming methods for thermoplastic composites.	14
Figure 2.1: The Stratasys Fortus 900 mc 3D printer used for the study.	17
Figure 2.2: Extruder Head in the Stratasys Fortus 900 mc.	18
Figure 2.3: Motion table and extruder head as reference for Stratasys Fortus 900 mc.	19
Figure 2.4: Thermoplastic material spools in canister for Stratasys Fortus 900 mc.	21
Figure 2.5: Toolpath parameters that can be varied in the Stratasys Fortus 900 mc.	23
Figure 2.6: An example of overhanging region that requires support during printing.	26
Figure 2.7: Calibration Squares printed during calibration of Stratasys Fortus 900 mc.	27
Figure 2.8: An image for CAD 3D model of the shoe part mold.	28
Figure 2.9: The heating platen used for heating the prepreg tapes.	32
Figure 2.10: The press with wooden box frame, mold and silicone foam rubber.	33
Figure 2.11: The mold, wooden frame and the silicon foam rubber.	34
Figure 2.12: Bottom side of formed part with 25 layers of prepreg tapes.	35
Figure 2.13: Top side of formed part with 25 layers of prepreg tapes.	35
Figure 2.14: Cross-section of the formed part along straight section.	36
Figure 2.15: Cross-section of the formed part along curved section.	36
Figure 2.16: The method used for determining the thermal working range of the mold material for the thermoforming process.	39
Figure 3.1: The internal structure of the printed material in XY plane (two stacked layers).	47
Figure 3.2: Internal structure in XY plane.	48
Figure 3.3: Internal structure in XZ plane.	48

Figure 3.4: Test setup for tension tests of ULTEM 9085 filaments used for printing.....	50
Figure 3.5: Tension test specimen for ASTM D638[47].	52
Figure 3.6: Tension test setup for coupons with lattice internal structure printed using ULTEM 9085.....	52
Figure 3.7: Compression test specimen for ASTM D6641 [48].	53
Figure 3.8: Shear Test Specimen for ASTM D7078[49] shear test.	54
Figure 3.9: Shear Test setup of the specimen with lattice internal structures printed using ULTEM 9085.....	55
Figure 3.10: Samples showing shift and filament misplaced because of the to sudden shifting of layers as seen through the glass window of the 3D printer oven.	56
Figure 3.11: Coupons printed for compression tests showing shifting of alignment at certain layers.	57
Figure 3.12: Set-up for compression test of solid-fill sample.....	58
Figure 3.13: Stress Strain curves for samples with lattice internal structure under tension loading in the X-axis.	61
Figure 3.14: Stress-Strain curves for samples with lattice internal structure under tension loading in the Z-axis.	62
Figure 3.15: Stress-Strain Curves for samples with lattice internal structure under compression loading in the X-axis.....	62
Figure 3.16: Stress-Strain Curves for samples with lattice internal structure under compression loading in the Z-axis.	63
Figure 3.17: Failure of a sample loaded in compression with walls failed in buckling after crushing internal lattice structure.....	64

Figure 3.18: Stress-Strain curves for samples with lattice internal structure under shear loading in the the YZ plane.....	65
Figure 3.19: Stress-Strain curves for samples with lattice internal structure under shear loading in the XZ plane.....	65
Figure 3.20: Stress-Strain curves for samples with lattice internal structure loaded in shear in the XY plane.	66
Figure 3.21: Samples showing failure planes on shear loading for different specimen printed with internal structures with different orientation.	67
Figure 3.22: Stress-Strain curve for samples with solid internal structure loaded in compression in the Z-direction.	68
Figure 3.23: Stress-Strain curve for tension tests of filament.....	69
Figure 4.1: Temperature dependent behavior of polymers [46].	73
Figure 4.2: Relaxation test [46].	74
Figure 4.3: Creep Test [46].....	75
Figure 4.4: Maxwell form of Standard Linear Solid (SLS) model [46].	75
Figure 4.5: Four parameter fluid model [46].	76
Figure 4.6: DMTA equipment with filament positioned between fixtures.....	77
Figure 4.7: Creep test setup for samples with lattice internal structure loaded in compression in Z-direction.	79
Figure 4.8: Creep response at different stress level for samples with lattice internal structure.....	81
Figure 4.9: DMTA of ULTEM 9085 filaments.	82
Figure 4.10: Creep Test results from each of individual nine tests.	83

Figure 4.11: Typical creep curve for polymers [47].	84
Figure 4.12: Curve fitting for three parameter solid model.	85
Figure 4.13: Curve fitting for four parameter fluid model.	85
Figure 5.1: Schematic of 3D space frame on the left and shells surrounding the space frame on the right.	89
Figure 5.2: Sketch of the unit cell of internal structure and its representation in finite element model.	91
Figure 5.3: FEM element mesh for compression test coupon gage section (Loaded in Z- direction).	94
Figure 5.4: Displacements with compression loading in Z direction.	99
Figure 5.5: Displacements with compression loading in the X direction.	99
Figure 5.6: Displacement in the Z direction for the Finite Element Model loaded in tension.	100
Figure 5.7: Displacement in the X direction for the Finite element model loaded in tension.	100
Figure 5.8: Shear Strains in the XY plane for the Finite Element model loaded in shear.	101
Figure 5.9: Shear Strain in the XZ plane for the Finite Element model loaded in shear.	101
Figure 5.10: Convergence plot for E_z in compression.	103
Figure 6.1: A beam with sine wave web printed using Stratasys Fortus 900 mc printer.	106
Figure 6.2: Typical setup for dry-run experiments.	107
Figure 6.3: Bending at center during stamping of unheated prepreg tape stack.	107
Figure 6.4: Female mold with design features.	108
Figure 6.5: Male mold with design features.	108

Figure 6.6: Bending reduced due to reinforcements in male mold.....	109
Figure 6.7: Finite element model to determine E_z and ν_{zy}	110
Figure 6.8: Calculation of poissions ratio of internal structure using the lattice structure finite element model for ν_{xy}	112
Figure 6.9: Finite element model for calculation of G_{xy}	114
Figure 6.10: Figure showing variables for shear modulus calculation.	115
Figure 6.11: Finite Element Model of the mold assembly.....	117
Figure 6.12: Major in-plane strain for sinusoidal part of the male mold.....	118
Figure 6.13: Strain of the finite element model in the Y direction.	119
Figure 6.14: Convergence plot the finite element model of the mold.	120
Figure 6.15: Setup for experimental verification of the finite element model.....	121
Figure 6.16: The formed part stuck to the male mold after pulling the mold to the top.....	123
Figure 6.17: Parts formed with increasing thickness from right to left.	124
Figure 6.18: Max In-Plane Principal Strains on the central part of the mold.	125
Figure 6.19: Comparison of the Major in-plane strain from the FE model to those observed experimentally.....	125
Figure 6.20: Maximum In-Plane Principal Strains on the central part of the mold from experiments.	126
Figure 7.1: Flowchart describing the mold design process - part 1.....	130
Figure 7.2: Flowchart describing the mold design process – part 2.	131
Figure 7.3: Deformations predicted in rubber stamp forming of the mold.....	133
Figure 7.4: Finite Element model E_z and ν_{zx} for internal structure with reduced air gap.	133
Figure 7.5: Deformations predicted with the new internal structure.	135

CHAPTER 1

INTRODUCTION

Various forming techniques exist to create parts using reinforced polymer composite materials, both thermoplastic and thermosets [1]. These methods include stamp forming, vacuum forming, vacuum assisted resin infusion molding (VARIM), and vacuum assisted resin transfer molding (VARTM) among others. Some methods like stamp forming and vacuum forming are more useful for thermoplastic composites whereas others like VARTM are useful for thermosets. In all these methods, molds are of central importance. Molds provide the framework for creating the part with the desired shape and size [2].

Molds have conventionally been made of metals using subtractive manufacturing methods. In these methods, suitable metal is cast into a block of approximate shape and size. Portions of such blocks are removed using computer numerically controlled (CNC) drill bits and/or sanders. The final product is the mold of required geometry [3, 4] .

The initial cost of using metallic mold for manufacturing process is high. Metallic molds also require a long time to manufacture [5].

Table 1.1 shows the costs and time of making metallic molds compared to that of molds made by fused deposition modeling (FDM). Compared to molds manufactured by using CNC machining, which is common with metallic molds, FDM offers faster and lower cost solutions. This high cost and time required for manufacturing metallic molds directs us to search for alternative molds. In stamp forming where new parts with different geometries need to be manufactured frequently thermoplastic molds created by additive manufacturing, also known as 3D printing,

offer a viable alternative to metallic molds. There are 3D printer systems that can create parts with high temperature thermoplastic materials like polyetherimide (PEI) and polyetheretherketone (PEEK). Molds can be made using these systems in very short times at low costs [6]. Such molds are already being used in injection molding processes [7, 8]. Furthermore, attributable to the cellular structure that these parts use, these molds are lightweight and require less material. In addition, the mold is recyclable because it is made from thermoplastics [9]. The study of the feasibility of using a 3D printed thermoplastic mold for stamp forming of thermoplastic composites is thus warranted.

1.1 RESEARCH OBJECTIVES

The primary objective of this research is to explore the feasibility of using 3D printed thermoplastic molds using FDM to form thermoplastic composite materials.

1. The first objective of this investigation is to formulate basic criteria for selection of thermoplastic polymer used for the 3D printed mold based on forming temperatures.
2. The second objective is to create a lattice and shell finite element model of the 3D printed part to characterize its linear elastic mechanical properties and validate these properties experimentally. A linear elastic lattice and shell model represents the basic structure of 3D printed part. This model would serve as a good starting point and can later be extended to model the behavior of more complex geometries and nonlinear behavior of the 3D printed material, if necessary. Once validated, this lattice and shell model can also be used to determine the properties of 3D printed material with different lattice configurations via virtual experiments.

3. The third objective is to study the mechanical behavior of the 3D printed material under elevated temperatures and sustained loads. During thermoforming, the elevated temperatures and sustained loads increase the strain on the material. It is necessary to understand how these strains evolve over time and could affect the overall thermoforming process.
4. The fourth objective is to use this use this lattice and shell finite element model to define an orthotropic solid finite element model that would be used in thermoforming simulations and to validate this orthotropic solid finite element model. A lattice and shell model is useful to generate the coupon level properties. However, as the mold size gets larger, a lattice and shell need more computational resources. A computationally inexpensive orthotropic solid model is necessary to model the larger molds, especially when the finite element model needs to be solved repeatedly during optimization procedures.
5. The final objective of this research work is to formulate a process to optimize the internal structure of a 3D printed mold for given mold geometry and loading conditions.

1.2 A DISCUSSION ON TERMINOLOGY USED

As a growing and rapidly changing field of technology, many new terms are introduced to describe techniques and processes used in additive manufacturing. Some terms are used in academia, while others are used in magazines and newspapers, and manufacturers of these machines for promotion use some of the terms. A brief discussion is considered necessary to define the terminologies used in this thesis.

1.2.1 3D Printing

The term additive manufacturing is used in academia to define the process whereby layers of materials are added one over another to create a part of required geometry. However, the term “3D-printing” has been found to be commonly used to describe additive manufacturing process. Although Wendel et. al [10], use the term “3D printing” to describe a process commonly described as binder jetting, in general, the term 3D printing is exchangeable with additive manufacturing. Ladd et. al. [11], in their paper, mention how many 3D printers extrude molten polymer that quickly cools and solidifies. Ladd et. al.[11] also describe their process of creating liquid metal microstructures as 3D printing. Lipson and Kurman[12] in their book *Fabricated: The New World of 3D Printing*, use the term “3D-printing” to describe all technologies ranging from binder jetting and polymer extrusion to biological additive manufacturing of a living tissue. Kenny et al [13] use 3D printing synonymously with 3D printing. Appleton [14] prefers the use of the term 3D printing and discusses that these terms are usually used interchangeably but acknowledges that there are some authorities who try to separate them, sometimes reserving 3D for the home printers and A/M for industrial uses. Appleton [14] also mentions that even though ASTM standard directs the term Additive Manufacturing, there is no mutual agreement and most practitioners use whichever term seems most convenient at the moment. In this thesis, the term 3D printing and additive manufacturing are used interchangeably.

1.2.2 Fused Deposition Modeling

Manufacturing companies, including Stratasys, RepRap and Makerbot, attribute the term 3D printing to what is described as Fused Deposition Modeling (FDM) of thermoplastic polymers by

Wendel et al [10] and categorized as material extrusion by ASTM. Fused deposition modeling (FDM) particular 3D printing technique used for the research work.

1.3 TIME AND COST REQUIRED FOR MANUFACTURE OF DIFFERENT MOLDS

As mentioned in Section 5, Table 1.1 compares the cost and the time required to manufacture metallic molds, which is compared with those required to manufacture an ULTEM 9085 polymer mold using the additive manufacturing technique. In Table 1.1, “manufacturer 1” is Xometry, 7951 Avenue, Gaithersburg, MD 20879, “manufacturer 2” is University of Maine Advanced Manufacturing Center and Advanced Structures and Composites Center, Orono, ME 04469, and “manufacturer 3” is Partsbadger LLC, 10555 N. Port Washington Rd. #204, Mequon, WI 53092. Similarly, part 1 is a male mold of size 279.4mm x 98.4mm x 34.9 mm, and part 2 is a female mold of size 279.4mm x 98.4mm x 38.1 mm. From Table 1.1, it can be seen that the cost of manufacturing thermoplastic molds is generally lower than that compared to the cost of manufacturing metallic molds. Aluminium molds are comparatively lower in pricing compared to stainless steel molds because aluminium metal itself is cheaper and aluminum is softer and easier to work with. Aluminium molds are generally used in prototyping for research and development purposes while stainless steel molds are used for production of large number of parts. The ULTEM 9085 mold with lattice internal structure is seen to be comparatively cheaper and faster to manufacture using additive manufacturing technology. The advantages of using additive manufacturing is more pronounced when the parts made are more complex features like radiator fins and release pins; as the complexity of the mold increases, the cost and time difference gap is widened between metallic molds and 3D printed thermoplastic molds.

Table 1.1: Time and cost of creating two different mold parts using different materials and different manufacturing techniques.

Manufacturer	Part	Material	Process	Cost (\$)	Time
Manufacturer 1	Part 1	Aluminium 6061	CNC machining	508.53	9 days
	Part 1	Stainless Steel 304	CNC machining	1841.16	14 days
	Part 2	Aluminium 6061	CNC machining	418.99	9 days
	Part 2	Stainless Steel 304	CNC machining	1645.06	14 days
	Part 1	ULTEM 9085	FDM	384.47	4 days
	Part 2	ULTEM 9085	FDM	305.20	4 days
Manufacturer 2	Part 1	Aluminium 6061	EDM wire	705.90	18 hours
	Part 1	Stainless Steel 304	EDM wire	1018.80	27 hours
	Part 2	Aluminium 6061	CNC machining	1647.10	42 hours
	Part 2	Stainless Steel 304	CNC machining	2377.20	63 hours
	Part 1	ULTEM 9085	FDM	186.52	6 hours
	Part 2	ULTEM 9085	FDM	200.32	6 hours

Manufacturer 3	Part 1	Aluminium 6061	CNC machining	189.94	14 days
	Part 1	Stainless Steel 304	CNC machining	520.99	14 days
	Part 2	Aluminium 6061	CNC machining	239.96	14 days
	Part 2	Stainless Steel 304	CNC machining	833.82	14 days

The Advanced Manufacturing Center at University of Maine provided an estimate of \$ 2354 for the aluminium 6061 mold assembly with \$121.90 for materials, \$800.00 for manufacturing costs, and \$1432.00 for labor. The Advanced Manufacturing Center also provided an estimate of \$351.90 for materials, \$1200.00 for manufacturing costs, and \$1844.00 for labor. It can be seen that the difference in costs for the molds made from these two materials comes mainly from the manufacturing and labor costs.

Even though the quotations from different manufacturers vary, it is observed that in general the 3D printed thermoplastic molds cost less to produce. These 3D printed molds were also comparatively faster to manufacture. 3D printed molds would be suitable for prototyping purposes for creating parts with lower production cycles compared to aluminium molds.

1.4 3D PRINTING METHODS

Additive manufacturing presents a paradigm shift in manufacturing. Compared to subtractive manufacturing, whereby a CNC machine is used to remove layers of material to get the part of desired shape and size, additive manufacturing adds layers of material one over other create

parts. Depending upon the method used to add materials, ASTM has categorized additive manufacturing into the following [15]:

1. In binder jetting method, liquid bonding agent is selectively deposited to join powder materials
2. Directed energy deposition uses focused thermal energy to fuse materials by melting as they are deposited
3. Material extrusion whereby material is selectively dispensed through a nozzle or orifice.
4. Material jetting selectively deposits droplets of build materials.
5. Powder bed fusion uses thermal energy to selectively fuse regions of a powder bed.
6. Sheet lamination, as the name suggests, bonds sheets of material to form an object
7. Vat photopolymerization, whereby, liquid photopolymer in a vat is selectively cured by light-activated polymerization.

The most common method for producing thermoplastic parts is material extrusion. Fused Deposition Modeling is the proprietary method employed by Stratasys in 3D printing of thermoplastic materials.

The FDM process is similar to other additive manufacturing processes in that a computer 3D model is made for the part to be manufactured. The model is then converted to an STL format and further processed by using another software program. This STL software slices the model into many layers of fixed heights. The outer boundaries, or contours, define the envelope of the part to be manufactured. The volume inside this boundary can be filled as necessary with sparse (with air gaps) or dense (without air gaps) internal structure. A toolpath is created by the software, which defines the movements that needs to be made by the CNC (Computer Numerical

Control) gantry in the 3D printer. The CNC gantry moves the extruder at the specified location for each these layers. The extruder places layer upon layer of molten filament according to the toolpath defined to create the required part [16, 17].

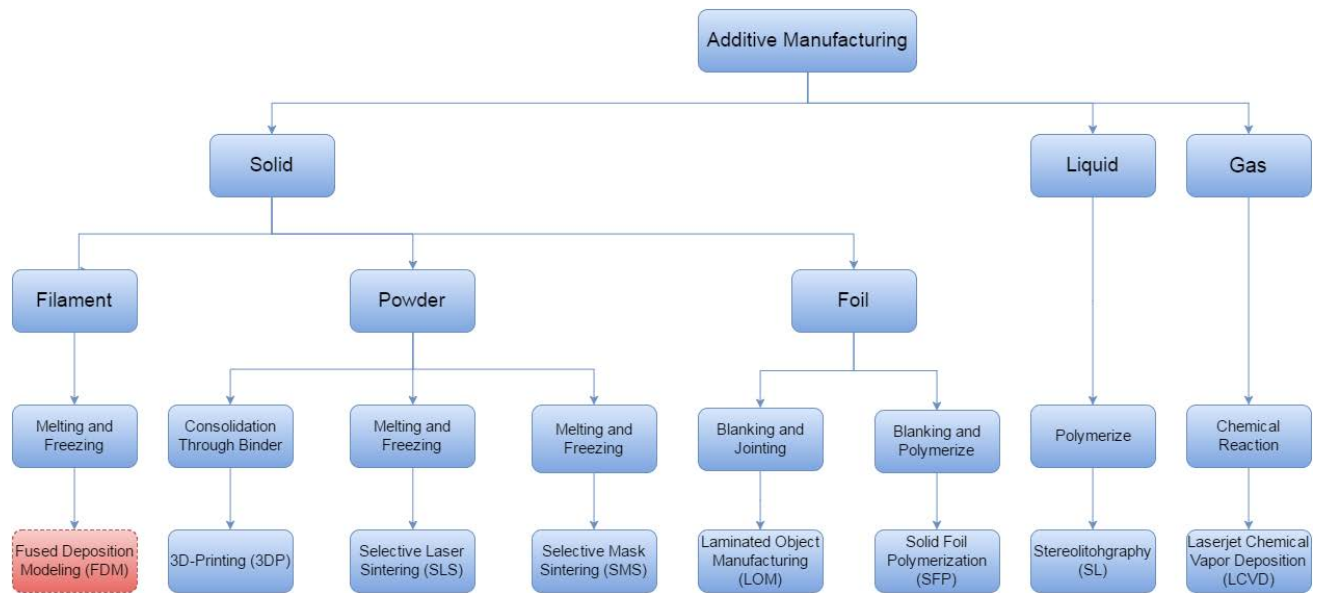


Figure 1.1: Different Additive Manufacturing Methods [10].

1.5 OPEN SYSTEMS VERSUS CLOSED SYSTEMS

Open systems are those systems that allow for the observation and modification of the internal processes in the 3D printer. The 3D printers manufactured by the RepRap and the earlier models of Makerbot systems serve as examples of open system 3D printers. In these systems, the user has the liberty to use custom material. The system lets the user modify the printing parameters like temperature, print speed and extrusion rate with ease. These systems are useful for research oriented towards printing new materials and optimizing the printing process for newer materials [18, 19].

Closed systems are those systems that allow very limited, if any, observation and modification of the internal processes in the 3D printer. The Fortus systems from Stratasys are examples of this type of system. The materials that can be used are fixed and the process parameters for these materials are pre-defined. The system allows for minor modifications in process parameters but the major parameters like extrusion temperature and printing speed are fixed. However, these systems provide higher reliability and reduced production times. These systems are useful for research that focus more on structures produced by 3D printing process rather than on the printing process itself. These systems are also useful for manufacturing production grade parts.

1.6 THERMOPLASTIC COMPOSITES MANUFACTURING

Thermoplastic composites have several documented advantages over thermosets. It is possible to melt and solidify thermoplastic materials without significantly changing their mechanical and chemical properties. This creates various opportunities for processing these materials.

Thermoplastic composite parts can be joined together just by heating and cooling without application of chemical adhesives [20]. These composites can be easily recycled and repaired.

Thermoplastic composites are also tougher compared to thermosets [21].

There are two major problems related to thermoplastic composites, which limit their use in industry. The first problem is that the raw materials for thermoplastic composites are more expensive compared to their thermoset counterparts. The price difference for the raw materials is expected to decrease with time and wider use. More efficient manufacturing techniques and economies of scale would result in the decrease of price for thermoplastic materials [22].

The second major problem related with thermoplastic composites is related to manufacturing. Thermoplastic materials are inherently more viscous compared to thermoset resins. The viscosity of thermoplastic composites is in the range of 500-1000 times that of thermoset resins. This renders use of certain manufacturing techniques like resin infusion and resin transfer infeasible. These techniques depend on flow of the polymer resin and polymers with high viscosity do not flow very well [23, 24].

Thermoplastic composites parts are manufactured using melt processing techniques. In melt processing, the thermoplastic polymer in the matrix is heated up to its melting point. This molten part is given required shape by the use of the molds. The part is cooled down until it solidifies and it is demolded. Application of pressure on the molten part during melt processing can be done either by using a press by using the “stamp forming” method or by using vacuum using “vacuum forming” method [25, 26].

The amount of pressure that can be applied using vacuum is theoretically limited to 0.1013 MPa (1 atm). In practice, the maximum vacuum pressure that can be applied is lower than this theoretical value. This limits the maximum thickness of the parts that can be formed by vacuum forming. The advantage of this technique is that it is relatively easy and fast compared to stamp forming. It also does not require press or other heavy and expensive equipment. Vacuum forming requires only one mold as opposed to stamp forming which requires matched male and female molds [27].

New techniques have been developed for manufacturing thermoplastic composites whereby different monomer components of low viscosity are mixed and the reinforcement material laid

out in required shape is infused with this mixture [28]. The resulting material is then cured so that the polymerization of the component monomers can take place. This process closely follows the manufacturing techniques of thermoset composite materials [29]. This process has been developed for only a few thermoplastics namely anionic polyamide (APA) and cyclic butylene terephthalate (CBT). The process requires higher processing temperature (150° C – 200 °C) compared to similar process for thermosets. The part also needs to be rapidly cooled down once the processing is complete to avoid voids and cracks running through resin rich areas [30].

Commercial thermoplastics with proprietary technology that can be processed at room temperature are also available [31]. Advances in this technology are expected to enable manufacturing of even thicker parts than those can be manufactured by stamp forming at lower costs [32, 33].

Molds made using 3D Printing offer advantages to all these forming processes. Some of the advantages are:

1. The manufacturing is fast and precise. Using additive manufacturing, prototypes can be manufactured faster and time to create the final product for the market can be reduced [34].
2. The manufacturing process produces little waste and thus saves material and production costs [35-37].
3. The process allows for mass customization of products without increasing the cost of each different item.
4. Additive manufacturing can be useful for ‘one-off’ or short run productions thus saving additional tooling and setup.

5. It allows complex parts to be produced with relative ease.
6. The part produced can be optimized to a greater degree. This can be used to create stronger and lighter parts [14].
7. Cooling or heating channels can be incorporated into the molds relatively easily [38].
8. For vacuum forming, pores can be incorporated inside the molds during manufacturing unlike in conventional metallic molds in which pores are drilled later.

Table 1.2: Prices of some common thermoset polymers compared with some common thermoplastic polymers [39, 40].

Polymer	Type	Price(\$/lb)
Epoxies	Thermoset	1.00 - 1.12
Polyesters	Thermoset	1.74 - 1.95
Vinyl esters	Thermoset	2.04 - 2.37
Phenolics	Thermoset	0.75 - 0.85
Polyethylene (HDPE)	Thermoplastic	1.04 - 1.15
Polypropylene	Thermoplastic	1.11 – 1.18
Polystyrene	Thermoplastic	1.26 – 1.50
Nylon	Thermoplastic	1.80 – 1.99

Additive manufacturing, however, has some limitations as well [41].

1. The maximum size of the parts produced is limited by the build envelope of the machine (printer).
2. Capital costs are high as modern 3D printers capable of manufacturing quality parts are expensive.
3. The price for mass manufacturing is comparatively higher as economy of scale has only small effects on additive manufacturing at its current state.

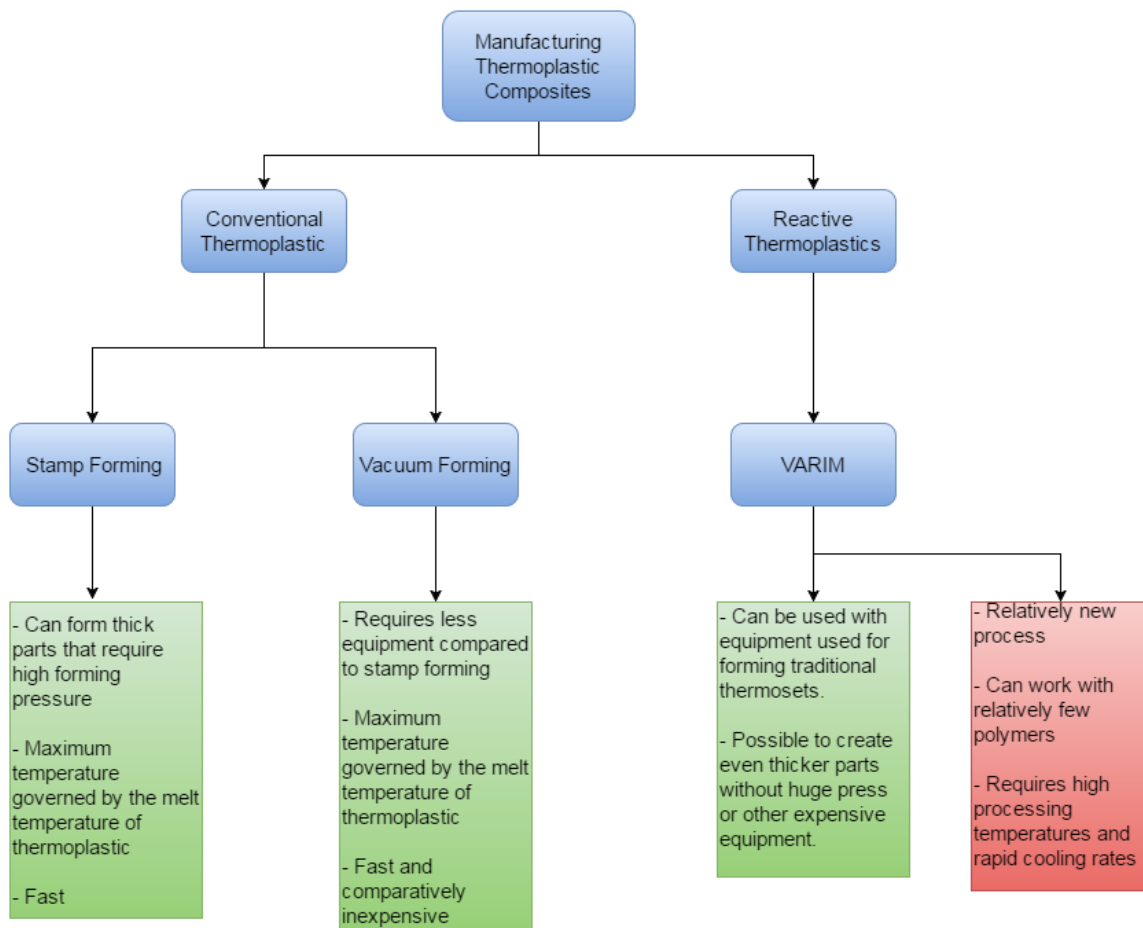


Figure 1.2: Forming methods for thermoplastic composites.

1.7 ORGANIZATION OF THE THESIS CHAPTERS

The thesis chapters are organized as follows:

1. The first chapter provides an introduction to the thesis, overviews the progress that has been made so far in this field and discusses what this research work covers.
2. The second chapter gives an overview of 3D printing process, with focus on fused deposition modeling. It goes through the preliminary test carried out to determine the decision-making criteria for testing the suitability of the molds for forming glass fiber reinforced polypropylene parts. It also presents a general method to determine the suitability of particular 3D printed material as mold for thermoforming another thermoplastic material.
3. The third chapter presents different quasi-static tests carried out on the 3D printed samples with lattice internal structures as well as the quasi-static tests carried out on the filament material. It discusses the observations that could be significant for the use of 3D printed structure as mold.
4. The fourth chapter presents the results from creep tests on the 3D printed lattice structure and the dynamic mechanical thermal analysis carried out on the filament material. The chapter discusses how these properties could be used in the process of mold design.
5. The fifth chapter offers a finite element model to predict the elastic response of the material. It discusses how this model could be used to speed up the mold design process.
6. The sixth chapter documents the optimization of a part to be formed by thermoforming. It also shows how a 3D printed mold was created for forming this part.
7. The seventh chapter outlines the conclusions drawn from the thesis work and recommendations for future work.

CHAPTER 2

3D PRINTING AND MOLD MATERIAL SELECTION

2.1 INTRODUCTION

The first step to determining the feasibility of using 3D printed thermoplastic materials is to understand the 3D printing process itself for thermoplastic materials. The most widely used method for 3D printing of thermoplastic materials is fused deposition modeling (FDM), whereby a molten filament of thermoplastic material is deposited one layer upon another to create a part of desired geometry. This chapter explores various steps in the FDM process and highlights the important steps that might have significant effects in the mechanical properties of the part created. This chapter also highlights the various parameters that define the geometry of the internal lattice structure of the 3D printed material. The parameters that can be controlled in the Stratasys Fortus 900mc 3D printer system have been focused because Stratasys Fortus 900 mc 3d printer system has been used for the study.

The preliminary tests carried out to determine the feasibility criteria to use the material as a mold are discussed in this chapter. The tests were carried out to determine the feasibility criteria for forming parts with polypropylene reinforced with glass fiber. The temperature and pressure withstood by the mold to form a good quality part is taken as the feasibility criteria.

A general method that can be used as a rule of thumb to determine the suitability of mold material based on glass transition temperature and melting temperature of the mold material and part material respectively is discussed in this chapter.

2.2 3D PRINTING PROCESS

3D printing, also known as additive manufacturing, is one of the newer manufacturing processes. It employs computer numerically controlled (CNC) mechanism to deposit layers of material in a series of steps to form a part of defined geometry. A variety of materials has been used for additive manufacturing, including metals, mortar and plastics [42].



Figure 2.1: The Stratasy Fortus 900 mc 3D printer used for the study.

2.3 COMPONENTS OF A 3D PRINTER

All FDM based 3D printers have a common set of parts that enable them to carry out the printing process. Some of the most significant parts are discussed in this section.

a. Computer numerically controlled (CNC) extruder head:

The CNC extruder head has two degrees of freedom. It can move in global X and Y directions in the horizontal plane. The extruder head has a heated tip to melt the thermoplastic material. The computer controlling the system moves the head to correct position, heats up the material loaded at the tip and extrudes necessary amount of material to deposit the required height and width.

The tip attached to the head and the flow rate of the extrudate controls the width of the deposit partially.

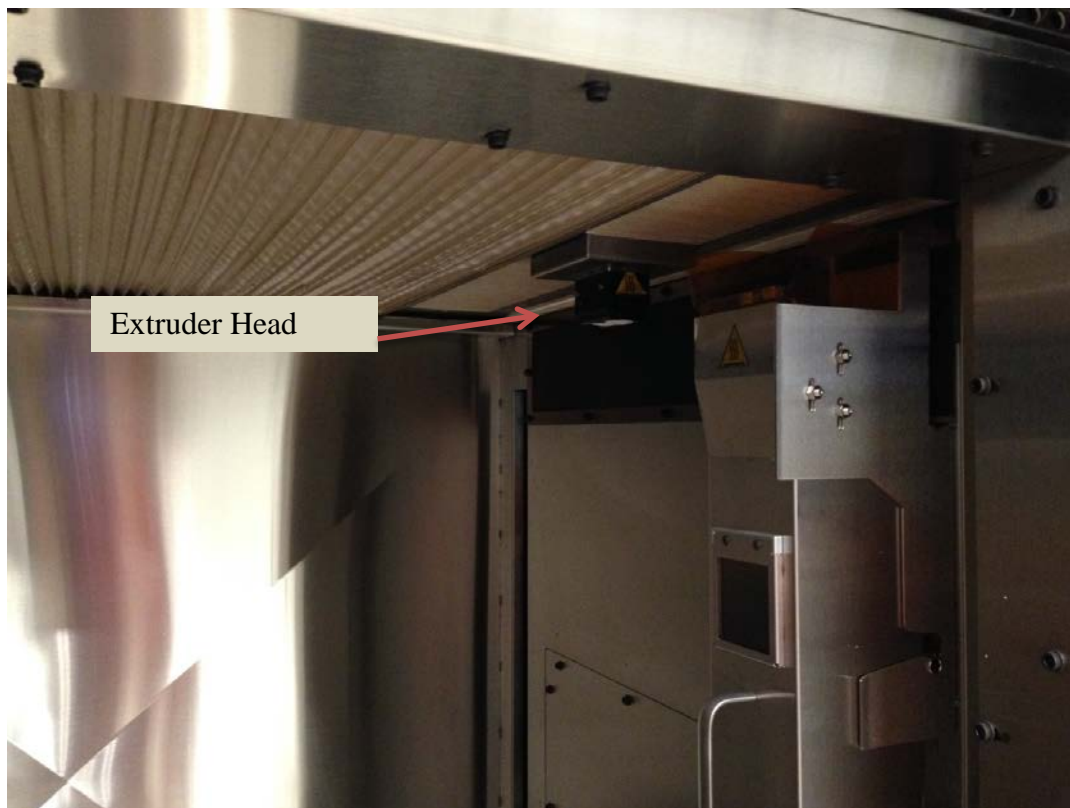


Figure 2.2: Extruder Head in the Stratasys Fortus 900 mc.

b. Motion table:

The motion table is free to move in Z direction and thus has one degree of freedom. The computer moves the table to the required height for deposition during manufacturing. A build sheet, which is a thin sheet (2 mm) of plastic (proprietary material sold by Stratasys) over which the first layers of deposits are made, is secured by the vacuum being applied through the holes on the table.

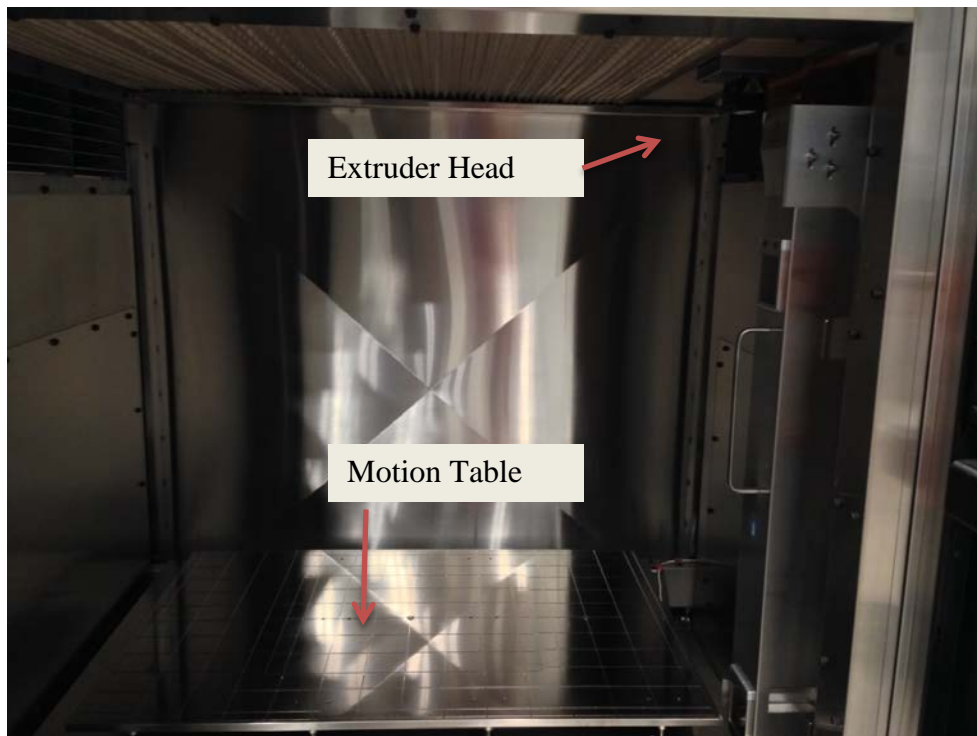


Figure 2.3: Motion table and extruder head as reference for Stratasys Fortus 900 mc.

c. Thermoplastic material spools (Canisters):

The polymer material to be loaded are loaded in canisters. The material is in the form of filaments of 1.70 mm diameter is rolled into a canister. These filaments are pulled to the extruder head as required.

d. Vacuum Pump:

The function of the vacuum pump is to create a vacuum inside the printer for stable operating environment. It also helps to secure the build sheet on the table.

e. Oven:

The oven raises the temperature inside the manufacturing area of the printer. This creates the thermal stability, which helps in manufacturing the parts with high precision. All FDM based 3D printers do not have an oven for controlling temperature, but the one used in this study was equipped with an oven.

f. Human Computer Interface:

The human computer interface enables interaction with the machine on a hardware level. It allows the user to calibrate the machine, get data from sensors pertaining to temperature, material available, or any problem encountered in printing, and carry out various other utility related functions.

2.4 STEPS INVOLVED IN 3D PRINTING

The process of 3D printing (additive manufacturing) involves two steps:

1. Software based steps, and

2. Hardware based steps

❖ Software based steps

These software-based steps constitute the definition the part geometry to be 3D printed and the print parameters that define the sequence and dimension of deposition of the material that form the 3D printed part.

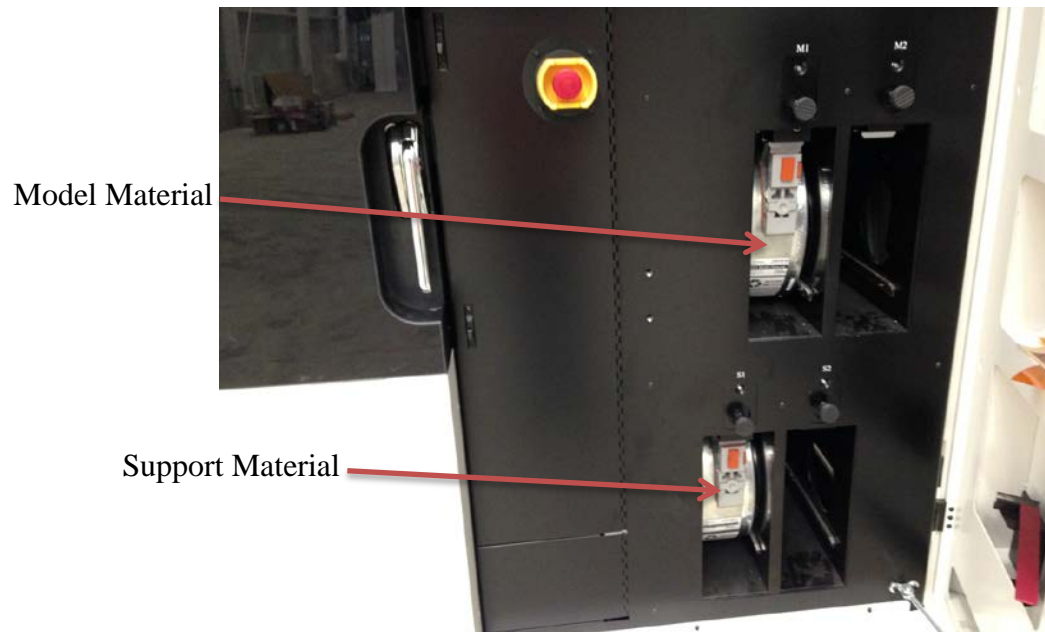


Figure 2.4: Thermoplastic material spools in canister for Stratasys Fortus 900 mc.

The geometry is modelled using 3D modelling software like Solidworks, NX, and CATIA. The geometry model is exported as a STL (sterolithography) file. The STL file uses triangles to approximate the surface of the solid model. The file contains a list of the three vertices. The surface is defined by triangle formed by the three vertices and a unit normal. The scaling is not included in this file so the dimensions are arbitrary. The consistency of modelling and manufacturing dimensions needs to be maintained when using the STL file.

The printing parameters constitute the sequence of deposition, the path to be followed during deposition, the dimensions of the deposited material, and some properties of the material that is being deposited. Based on these parameters, the proprietary software for the 3D printer determines the movement path for the extruder head and the motion table, as well as the height of deposition and the correction for shrinkage of the material.

Some of the important printing parameters that have significant effect on the mechanical properties of the part to be printed are listed.

i. Slice Height:

It is the height of each layer of the deposited material. Increasing the slice height decreases the number of deposition layers, and hence decreases the number of layers that need to be fused together. The plane of fusion is a plane of weakness where the material is likely to fail. So, a part with greater slice height would be expected to exhibit better mechanical performance compared to a part with smaller slice height. On the other hand, if the slice height is too high, the molten deposition layer deforms under its own weight and does not conform with the required geometry, creating improper bonding between the layers. As a result, the slice height needs to be within a specified range to get optimum mechanical performance from the 3D printed material [43].

Also, increasing the slice height decreases the time required for 3D printing the part. However, increasing the slice height lowers the precision of 3D printed part if the part has a geometry that is curved along the Z-axis of the printer.

ii. Toolpath parameters:

These parameters are used by the proprietary software to calculate the actual path moved by the extrusion head for deposition of thermoplastic material during manufacturing. The toolpath parameters used for 3D printing are listed shown in Figure 2.5. Some of the important toolpath parameters are:

▪ Contours:

Contours are closed curves that define the boundaries of the parts to be manufactured. These

are curves created by intersection of plane at specified height with the surfaces defined by the STL file.

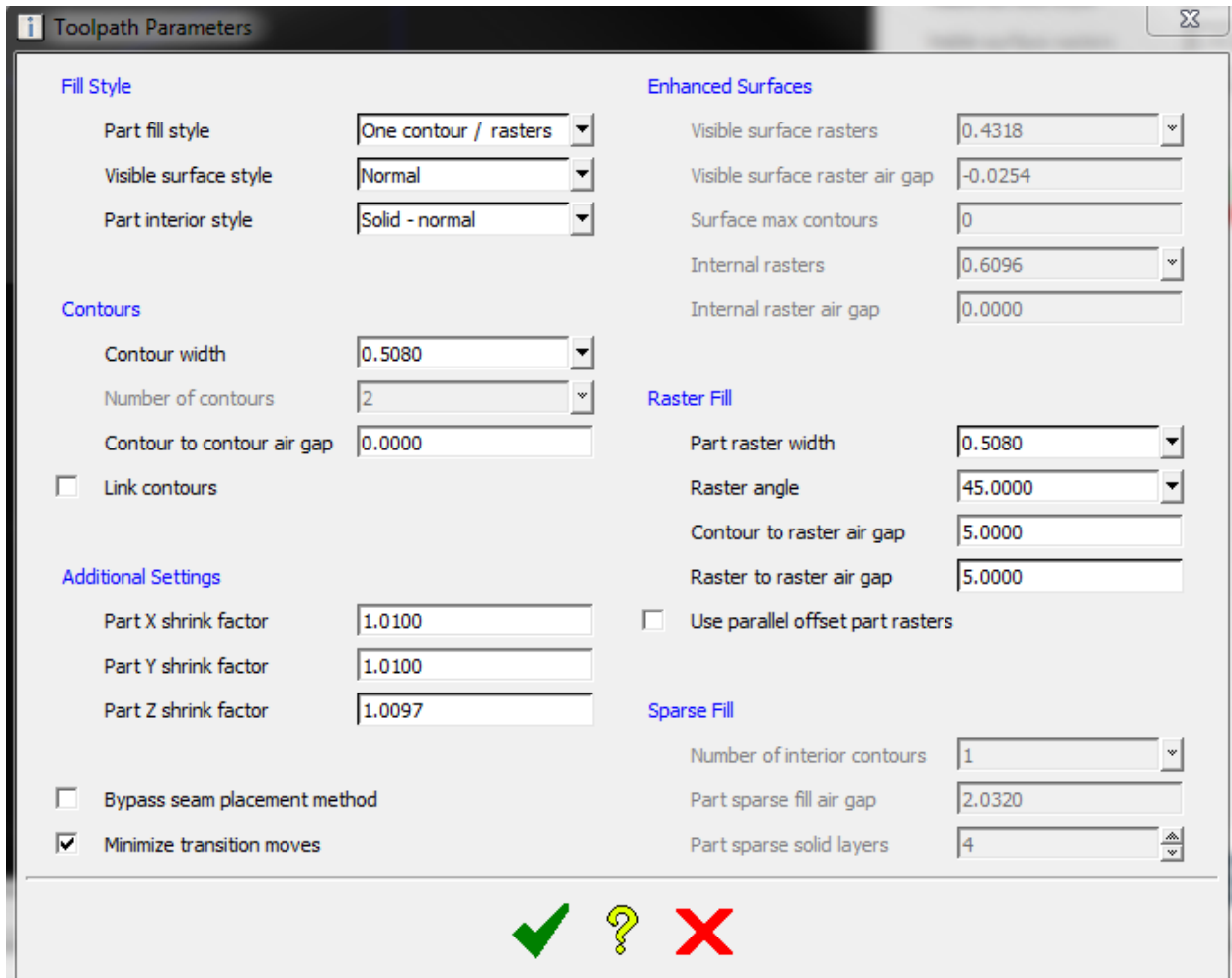


Figure 2.5: Toolpath parameters that can be varied in the Stratasys Fortus 900 mc.

- Internal fill (Fill Style):

These parameters define the fill inside the perimeter defined by the contours. The inside area can be completely filled with the thermoplastic material, which is called solid fill.

Alternatively, it can be partially filled with air gaps, which is called sparse fill by Stratasys.

This essentially creates a material with lattice internal structure.

A completely filled part is stronger and has higher elastic modulus compared to a part partially filled with air. However, a part partially filled with air is faster to 3D print and offers opportunities to minimize material use while optimizing the mechanical properties.

The internal fill is further defined by fill type, raster angle and air gap.

There are various ways to fill the area bounded by the perimeter of the contour. Rectangular sparse fills, rectangular double sparse fills, hexagonal fills, porous hexagonal fills, and sawtooth fills are some of the fills that can be used in the 3D printer system used for this study. Open systems allow for direct control of toolpath which allows for infinite number of ways to fill the area bounded by the perimeter of the contour.

The raster angle is the angle at which the internal fill is oriented with respect to the X-axis of the printer. The air gap defines the distance between the two internal fill rasters. For this study, rectangular sparse fills were chosen because it results in faster 3D printing. In this fill style, the extruder head moves across the area defined by the contour in a straight line at an angle defined by the raster angle. The extruder head then shifts a distance along X-axis defined by the air gap and deposits the material along another straight line. These processes are repeated until the area in the given level is covered. For the next layer, the same processes are repeated but an angle of 90 degrees is added to the previous raster angle. This fill style is faster than other fill styles because the transitions in movement of extruder head are minimized.

It has to be noted that these are the terminologies used by Stratasys. The internal structure is referred to as lattice structure throughout the thesis from hereafter.

- Shrink Factors:

These are material properties that depend upon the material being used and other process parameters. These parameters determine the correction in the measurements so that the part has correct dimensions when cooled down. The toolpath parameters that can be modified in Fortus 900mc 3D printer used for this study are shown in Figure 2.5.

- ❖ Hardware based steps (physical steps):

After the 3D model is created, the model is passed to the proprietary software as a STL file, the printing parameters are defined, and the part is ready to be printed.

The first layer to be printed is a layer of support material. This is done so that the part can be removed easily after it has finished printing. After the layer of support material is deposited, the first layer of the part is deposited over the support material layer. A new layer is deposited one after another until the final part is ready. The molten new layer easily sticks with the previous layer because the material being used is thermoplastic material and the application of adhesive between the layers is not necessary. There are regions of overhang that require support.

Overhang regions can be visualized as the regions that have cantilevered out of the part. The molten material does not have necessary strength to support those parts. These parts are supported by making a supporting structure out of support material. After the part is completely manufactured and cooled down, the support structure can be broken down or dissolved chemically, depending upon the thermoplastic material used.

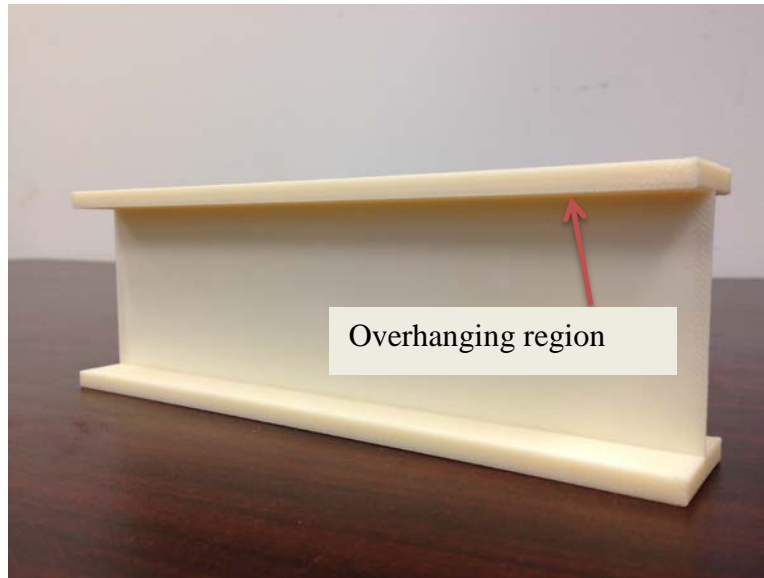


Figure 2.6: An example of overhanging region that requires support during printing.

2.5 THE CALIBRATION PROCESS FOR 3D PRINTER TABLE AND EXTRUDER HEAD

Calibration is an essential process in 3D printing. This ensures high degree of accuracy during printing. This is done by printing a test square. Each edge of the test square has two guiding lines with numbers marked on side. A thin thread is printed such that it is in between the two guiding lines. The test square is then examined under a magnifying glass. The number in the area where the thread is exactly in the middle of the two guiding lines is the correction necessary. If the thread is exactly in the middle of the two guiding lines for the whole length, no further correction is necessary. This is observed if the test square is printed again after the calibration is complete.



Figure 2.7: Calibration Squares printed during calibration of Stratasys Fortus 900 mc.

2.6 EXPERIMENTATION FOR PROOF OF CONCEPT

Preliminary tests were carried out to prove the concept of using 3D printed mold for forming thermoplastic composites. The suitable temperature and pressures for forming a thermoplastic composite part were determined. Polypropylene reinforced with E-glass fiber tape was used to make parts for the study because of its low melting point temperature requirements.

2.6.1 The Mold

The mold was manufactured by Stratasys as a demonstration for the capabilities of the Fortus 900 mc 3D printer system. The mold was 3D printed using ULTEM 1010 material.

The mold was designed to create a part with the geometry for the sole of a shoe using compression molding process. The mold was part of a matched mold system. The male part of the matched mold system was used as the mold for this experimentation for the proof of concept. The shoe part mold had a planar dimension of 305 mm x 152 mm (10in x 5 in). The internal core of the mold had a cellular structure with slice height of 0.25 mm (0.01 in), contour width of 0.51 mm (0.02 in), raster angle of 45 degrees, and internal air gap of 2.54 mm (0.1 in).

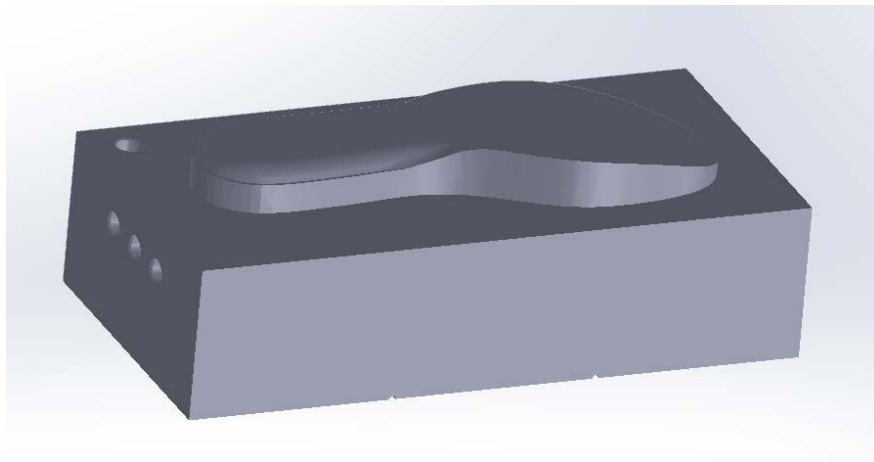


Figure 2.8: An image for CAD 3D model of the shoe part mold.

2.6.2 Material and Laminate Preparation

Among the various thermoplastic materials considered for this proof of concept tests with their respective melting point temperatures are listed in Table 2.1.

The selection of the thermoplastic material for thermoforming was limited mostly by the fact that the glass transition temperature of ULTEM 1010 was 217 °C. The thermoplastic material needed to have melting point that is significantly below this temperature. The melting point of polypropylene ranges between (130 °C - 170 °C) depending upon the molecular weight and

crystallinity of the propylene used. Polypropylene with even the highest degree of crystallinity had a melting point significantly below the glass transition temperature of ULTEM 1010.

The selection of the thermoplastic material for thermoforming was limited mostly by the fact that the glass transition temperature of ULTEM 1010 was 217 °C. The thermoplastic material needed to have melting point that is significantly below this temperature. The melting point of polypropylene ranges between (130 °C - 170 °C) depending upon the crystallinity of the propylene used. Polypropylene with even the highest degree of crystallinity had a melting point significantly below the glass transition temperature of ULTEM 1010.

As a result of this polypropylene was chosen as the material to be thermoformed. Unidirectional prepreg PP/GF tapes were laid up in following sequence:

- a) $[\pm 45]_6$ (12 layers)
- b) $[0/90]_6$ (12 layers)
- c) $[(0/90)_{12}/0]$ (25 layers)
- d) $[(0/90)_{25}]$ (50 layers)

Table 2.1: Materials considered for thermoforming with their melting temperature.

Thermoplastic Material	Melting Point (°C)
Polyetheretheretone (PEEK)	382
Polyetherimide (PEI)	371
Polysulfone	371
Polycarbonate (PC)	288
Polyethylenerephthalate (PET)	282
Polybutylenerephthalate (PBT)	260
Polyethylene	204 - 163
Polyvinylchloride(PVC)	177
Polypropylene(PP)	130-170

The planar dimensions of the layup were 305 mm x 152 mm (12 in x 6 in). The thickness of prepreg tape was 0.25 mm (0.01 in). The layup was covered by Teflon sheet of thickness 0.005 mm (0.02 in). The Teflon sheet acted as a mold release layer.

The layup with maximum number of layers (50 layers) was chosen so that sum of the thickness of the tapes would be 13 mm (0.5 inches) which is common for plates. This would provide a good idea about the quality of part made after stamping just by observation because any

malformation or wrinkling would be easy to notice. The other thinner layups were used to verify if the high pressure used for thick part would negatively affect the thin parts. A $[\pm 45]_6$ layup was made to see if alternative layup would cause any unanticipated problems in stamp forming process.

2.6.3 Heating Apparatus

A heated platen developed for forming of consolidated PET plates [44] was used. The platen was made up of 1020 mild steel with following dimensions were used: 0.61 m (24 in) wide, 0.864 m (34 in) long, and 0.076 m (3 in) thick. The heating of the plate was carried out using twelve 0.61 m (24 in) long, 3500 watts, 480 volt, swaged cartridge heaters, totaling 42kW of available input energy. The heaters were evenly spaced. The cartridge heaters were arranged in three zones of four cartridge heaters. The inner four heaters were placed on zone 1, the outer two on either side on zone 2, and the remaining four heaters on zone 3. A Watlow EZ-Zone Express PID controller with a 3-phase 480V input power source controlled each heating zone. The plate is capable of heating at a rate of $16^{\circ}\text{C}/\text{min}$ ($30^{\circ}\text{F}/\text{min}$). The maximum working temperature of the heated plate is 400°C (750°F).

The heated plate in the laboratory is shown in Figure 2.9. A piece of fiberglass insulation board was spaced 2.54 cm (1 in) from the bottom of the plate under the plate to help insulate the base of the heated plate, as seen in Figure 2.9. The 2.54 cm (1 in) gap was filled with high temperature fiberglass insulation.

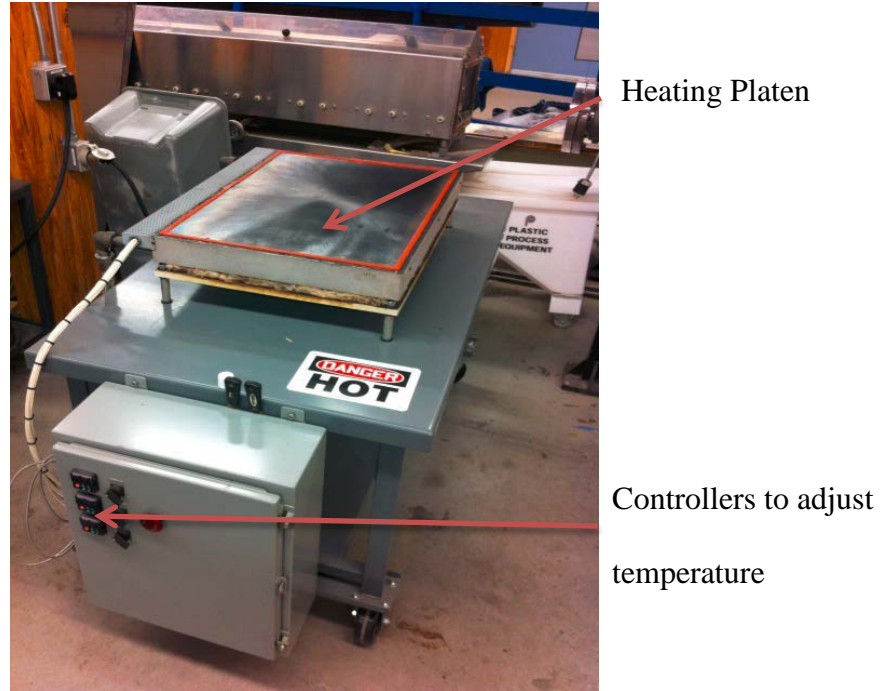


Figure 2.9: The heating platen used for heating the prepreg tapes.

2.6.4 Press

A 50-ton hydraulic press was used to apply pressure on the specimen. The upper platen of the press was mobile while the lower platen was fixed. The pressure on the mold specimen of size 12"x6" was calibrated using the calibration table of the press. A 25.9 MPa (3750 psi) gauge on press corresponded to a pressure of 3.45 MPa (500 psi) on the mold. The height of lower platen of the press was adjusted so that the mold would be in contact with the specimen when upper platen comes down. The male mold was attached to the top of the press using a double-sided tape. A wooden deckle-box frame conforming to the size of the mold was made. The frame was fitted with four layers of silicon foam of thickness 1 inch each. The mold was aligned with the wooden frame such that the mold fit within the wooden frame when pressed. The press used is shown in Figure 2.10.



Figure 2.10: The press with wooden box frame, mold and silicone foam rubber.

2.6.5 Procedure for forming the part

The sample of stacked prepreg tapes was placed above the platens for heating. The sample was covered with glass wool to reduce heat losses through conduction and convection. The temperature was monitored using the electrical thermometer. The thermometer was placed at the top of the PP/GF layup specimen.

A fixed temperature of 130 °C was chosen because it is the known melting temperature of the polypropylene used. Trials at temperatures higher than 130 °C (140 °C and 150 °C) were done but no significant difference in the formed part was found. Trials at temperature lower than 130 °C (120 °C) resulted in improper bonding between the layers. A pressure of 3.45 MPa was determined to provide proper part consolidation after few trials at pressures ranging from 2.07

MPa (300 psi) to 3.45 MPa(500 MPa) did not give satisfactory results for the thickest layup. After the temperature reached 130°C (266°F), the sample was placed in the press and pressure was applied at 3.45 MPa (500 psi). Pressure was maintained for 1 minute so that the specimen could conform to the shape of the mold and cool down. The pressure was released and the upper platen was retracted to obtain the formed composite part.

2.6.6 Thermoforming Results

The composite specimen appeared to conform closely with the contours of the mold for all specimens except the 50 layer thick specimen. The consolidation of the part with 50 layers of tape was satisfactory in the areas where the part was flat. The individual prepreg tape layers had a thickness of 0.25 mm. For 50 layers of tape, the thickness was expected to be less than the sum of thicknesses of the individual tapes, i.e., less than 12.5 mm. The final part thickness was found to be 11.9 mm. The tapes were brought down to 95.2% of the sum of their original thicknesses. As the tapes used were pre-consolidated tapes, the final part thickness was expected to be very close to the sum of the thicknesses of tape layers.

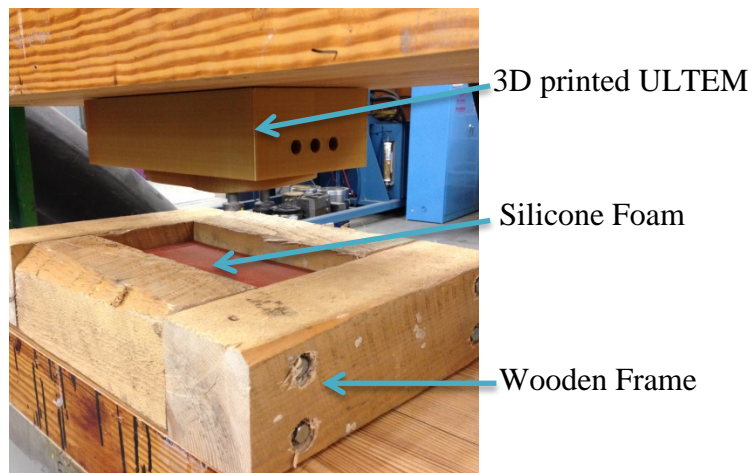


Figure 2.11: The mold, wooden frame and the silicon foam rubber.

Hence, the part was considered to have satisfactory consolidation. Similarly, for parts with 25 layer tapes, the expected final thickness was 6.25 mm. The final thickness obtained was 6.08 mm. The tapes were brought down to 97.3% of the sum of their original thicknesses. The final consolidated parts for the 25-layer layup are shown in Figure 2.12, Figure 2.13, Figure 2.14, and Figure 2.15.

However, in the region with curvatures, the part did not conform readily to the geometry of the mold and showed visible signs of wrinkling. The thinner parts formed more easily and conformed to the mold shape more readily compared to the thicker parts. This could be attributable to the non-uniform heating of the thicker parts. The fact that the difference in curvature of the surface in contact with the mold compared to the curvature of the surface farthest from the mold would have created high stress through the thickness, causing the material to wrinkle.



Figure 2.12: Bottom side of formed part with 25 layers of prepreg tapes.



Figure 2.13: Top side of formed part with 25 layers of prepreg tapes.

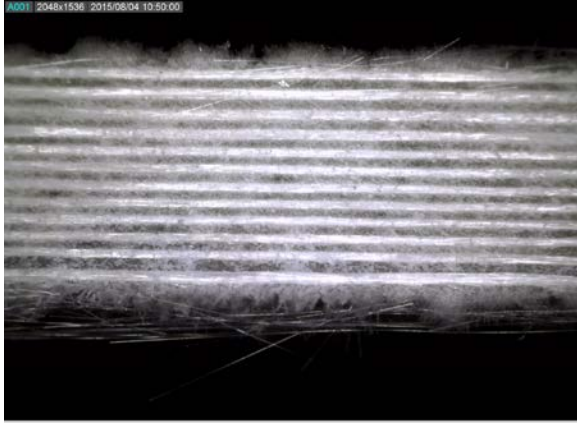


Figure 2.14: Cross-section of the formed part along straight section.



Figure 2.15: Cross-section of the formed part along curved section.

2.6.7 Conclusions

From the preliminary experimentation, it was concluded that a forming pressure of 3.45 MPa (500 psi) and a temperature of 130 °C was suitable for thermoforming E-glass fiber reinforced polypropylene parts. This pressure and the temperature were determined as the process variables required to be used for thermoforming glass fiber reinforced polypropylene parts. In areas of high curvature, wrinkling was observed in thick samples (with 50 layers). For thin samples (with 25 layers and 12 layers), the areas of higher curvature had smaller thickness compared to the areas of lower curvature. The flat areas had uniform thickness and no wrinkling for both thin and thick samples.

2.7 MOLD MATERIAL SELECTION

The choice of several thermoplastic materials is available for printing with the Fortus 900 mc 3D printer. The stiffness, strength and temperature requirements limit the choice of material to be thermoformed. A simple method based on a few basic assumptions can be employed to calculate the range of thermoplastics that can be formed with a mold made of a given thermoplastic material.

Equation (1) needs to be satisfied by the mold and the part for the thermoforming process to be viable. Equation (1) looks similar to the equation used in operational temperature range of hot melt adhesives. Pocius [45] uses a similar equation to define the active range of hot melt adhesives. However, the equation used by Pocius [45] considers melting temperature and glass transition temperature of the hot melt adhesive, whereas in Equation (1), the glass transition temperature of mold polymer is compared with the melting temperature of the part polymer.

$$T_{g,mold} = T_{m,part} + \Delta T \quad (1)$$

$T_{g,mold}$ = Glass transition temperature of mold material

$T_{m,part}$ = Melting temperature of material to be thermoformed

t = time of contact

t_{eq} = time required for the layer of unit depth to reach thermal equilibrium with part

κ = thermal conductivity of the interface

A = area of the interface between mold and part

C_m = specific heat capacity of the mold material

$T_{i,mold}$ = initial temperature of the mold material

Δd = unit depth

ρ_m = density of the mold material

ΔT = minimum temperature differential

Figure 2.16 shows the curve for storage modulus (E) vs the temperature for two amorphous materials. The solid blue curve shows the behavior of the mold material and the dotted black curve shows the behavior of material to be thermoformed. Both materials show significant loss in storage modulus (and hence the stiffness) after reaching the glass transition temperature [46]. The graph shows the difference between the glass transition temperature of the mold material and the melting temperature of thermoplastic part material as ΔT . If the part material was semi-crystalline, or crystalline, the curve would be different but the melting temperature of the part polymer would be considered for equations in this method. This method considers amorphous polymers only for the mold.

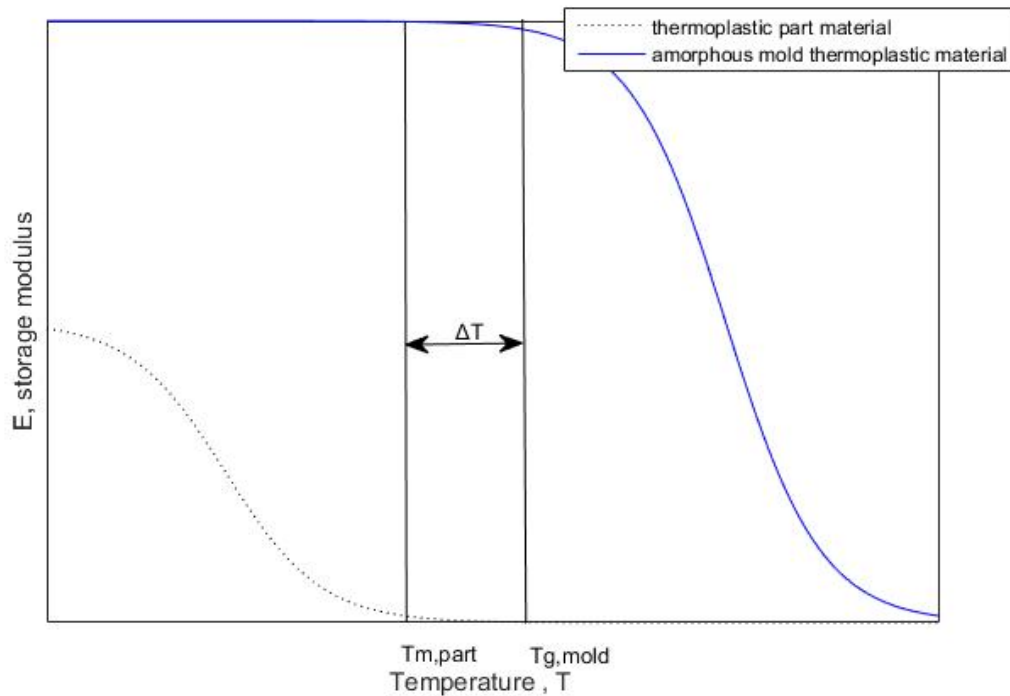


Figure 2.16: The method used for determining the thermal working range of the mold material for the thermoforming process.

Assuming the following:

1. The temperature is uniform throughout the contact area.
2. The temperature across unit depth (Δd) region is equal. Δd is considered small.
3. Time of contact is less than time required for the unit depth region considered to reach thermal equilibrium with the molten part to be thermoformed.
4. The temperature of mold material rises linearly with time when in contact with molten part material.
5. Heat transfer is linear across the contact area.

Considering the initial temperature of the mold as $T_{i,mold}$ and a unit depth of mold material, for the final temperature of the mold to be the glass transition temperature of the mold material,

$$T_{g,mold} > T_{i,mold} + \frac{Q}{C_m \rho_m A \Delta d} \quad (2)$$

where,

the heat that raises the temperature of the mold is the heat that is transferred from the molten thermoplastic through the interface

$$Q = \frac{t}{t_{eq}} C_m \rho_m A \Delta d (T_{m,part} - T_{i,mold}) \quad (3)$$

Where,

$$t_{eq} = \frac{C_m \Delta d^2 \rho_m}{\kappa} \quad (4)$$

Hence,

$$T_{m,part} + \Delta T > T_{i,mold} + \frac{t}{t_{eq}} (T_{m,part} - T_{i,mold})$$

$$\Delta T > T_{i,mold} + \frac{t}{t_{eq}} (T_{m,part} - T_{i,mold}) - T_{m,part} \quad (5)$$

From equation (5), we can see that ΔT depends upon the contact time and the heat conductivity of the interface. This ΔT value can be reduced by using a thin insulation between the material and the mold such that it does not affect the geometry or integrity of the mold significantly. In addition, for the thermoforming processes the contact time necessary for the stamp-forming process is usually 3 to 5 seconds.

By using a material with suitable heat conductivity and contact time, the ΔT value could effectively be reduced to zero or even made negative. This means that a higher temperature thermoplastic can potentially be stamp-formed using a lower temperature thermoplastic. Further investigation is necessary to study such possibilities.

The following numerical example shows the use of the above equation for determining the suitability of a material as a mold. Considering a mold of polyetherimide (PEI) and a part of polypropylene, with mold initially at room temperature of 23 °C and polypropylene at its melting point of 130 °C, the following values are assigned:

- Glass transition temperature of the mold material, $T_{g,mold} = 217$ °C
- Melting temperature of part material, $T_{m,part} = 130$ °C
- Time of contact (assumed), $t = 5$ seconds
- Time required to reach thermal equilibrium for unit depth, $t_{eq} = 11.5$ sec
- Initial temperature of the mold, $T_{i,mold} = 23$ °C
- Unit Depth, $\Delta d = 1$ mm = 0.001m
- Specific heat capacity of the mold material (assuming solid fill),

$$C_m = 2000 \text{ J } ^\circ\text{C}^{-1} \text{ kg}^{-1}$$

- Thermal conductivity of the interface (assuming solid fill for PEI),

$$\kappa = 0.22 \text{ W m}^{-1} \text{ }^{\circ}\text{C}^{-1}$$

We have,

$$T_{i,mold} + \frac{t}{t_{eq}}(T_{m,part} - T_{i,mold}) - T_{m,part} = -60.61 \text{ }^{\circ}\text{C}$$

Also,

$$\Delta T = T_{g,mold} - T_{m,part} = 87 \text{ }^{\circ}\text{C}$$

So, the condition for Equation 5,

$$\Delta T > T_{i,mold} + \frac{t}{t_{eq}}(T_{m,part} - T_{i,mold}) - T_{m,part} \quad \text{is satisfied.}$$

Hence, ULTEM 1010 can be used as mold material for forming polypropylene parts.

2.7.1 Available materials and their properties

The materials that are available that can be printed with the Fortus 900mc 3D printer and their properties are listed in Table 2.1. From Table 2.1, it is observed that all the materials satisfy the strength required to withstand the thermoforming pressure of 3.45 MPa. However, the materials with high enough glass transition temperature required for thermoforming. Nylon is not thermally stable and hence is not considered suitable for thermoforming. After these eliminations, the remaining thermoplastic materials that can be considered suitable for usage as a mold in thermoforming operations are PPSF/U, ULTEM 9085 and ULTEM 1010. ULTEM 9085 was chosen for further study because it has acceptable strength values, and elastic modulus values, and the glass transition temperature is comfortably higher than the thermoforming temperature of 130 °C.

Table 2.2: Materials available in Stratasys Fortus 900mc for 3D printing.

Material	ABS	ASA	Nylon	PC	PPSF/U	ULTEM 9085	ULTEM 1010
Tensile Strength (MPa)	34.8	30	48	52	55	71.6	110
Tensile Modulus (MPa)	1827	1950	1700	2000	2068	2200	3580
Flexure Strength (MPa)	50	48		97	110	115	165
Flexure Modulus (MPa)	1863	1630	1500	2137	2206	2500	3510
Heat Deflection Temperature (°C)	96	91	177	127	189	153	213
Pressure for given HDT (MPa)	1.82	1.82	1.82	1.82	1.82	1.82	1.82
Glass Transition Temperature Tg (°C)	112	108	181	161	230	186	215

Assuming a contact time of 10 seconds and initial mold temperature of 23 °C, a list of thermoplastic parts that can be formed by using the polymer for the mold can be obtained. No insulation is used for these analyses. The physical and thermal properties of polymers are taken from www.matweb.com website. For properties that have a range, the lower value of the range is taken. For example, the melting temperature of PET is given as 200 °C -260 °C and 200 °C is taken for this analysis.

Table 2.3: Compatibility of available mold polymers for Fortus 900 mc with the parts that can be thermoformed.

Mold Polymer	ABS	ASA	Nylon 12	PC	PPSF/U	ULTEM 9085	ULTEM 1010
Part Polymer							
HDPE	NG	NG	OK	OK	OK	OK	OK
PP	NG	NG	OK	OK	OK	OK	OK
PMMA	NG	NG	OK	NG	OK	OK	OK
POM	NG	NG	OK	NG	OK	OK	OK
PA12	NG	NG	OK	NG	OK	OK	OK
PETG	NG	NG	OK	NG	OK	OK	OK
PET	NG	NG	NG	NG	OK	OK	OK
PA6	NG	NG	NG	NG	OK	NG	OK
PBT	NG	NG	NG	NG	OK	NG	OK
PET-SC	NG	NG	NG	NG	OK	NG	NG
PET-P	NG	NG	NG	NG	OK	NG	NG
PPS	NG	NG	NG	NG	NG	NG	NG

The results of these analyses are shown in Table 2.1. The cells marked “OK” with green fill color satisfy Equation (5) with wide margin, the cells marked “OK” with yellow green fill color satisfy the equation with narrow margin, and the cells marked “NG” with red fill do not satisfy the equation.

2.8 CONCLUSIONS

The following conclusions have been drawn from the research work carried out in this chapter:

1. Several printing parameters affect the mechanical properties of the part created by using FDM 3D printing technique. Care should be taken while selecting these parameters to get optimum mechanical performance from the parts created.
2. A simple formula can be used to ascertain the initial suitability of a thermoplastic material as a mold for thermoforming another thermoplastic material based on the melting point of the part and glass transition temperature of mold material.
3. A temperature of 130°C and a pressure of 3.45 MPa is necessary to thermoform polypropylene reinforced with E-glass fibers up to 13 mm (1/2 inch) thick parts with very small or no curvatures or for parts with 8mm (0.25 inch) thick parts with significant curvatures. The parts formed have continuously varying thickness around the curved areas.
4. The mold formed must be able to withstand a pressure of 3.45 MPa without significant deformation at the thermoforming temperatures to effectively be used as the mold.

CHAPTER 3

MOLD INTERNAL STRUCTURE AND QUASI-STATIC PROPERTIES

One of the opportunities presented by 3D printing is that it allows for modifications of the internal structure of the part to be printed. This creates possibilities to vary the strength and elastic modulus of the part so that an optimal balance can be reached between required mechanical properties, material usage, and time to manufacture the part.

3.1 INTERNAL STRUCTURE OF THE MOLD

The internal structure of the mold was treated as a different material by defining a unit cell as shown in Figure 3.1.

For the purposes of this study, the following parameters were used:

- Width of each layer: 0.51 mm
- Slice height: 0.25 mm
- Number of transition layers from outside cover layer to inner cellular structure: 2
- Raster angle: 45 degrees
- Air gap: 2.03 mm
- Shrink Factors:
 - X-direction: 1.01
 - Y-direction: 1.01
 - Z-direction: 1.01

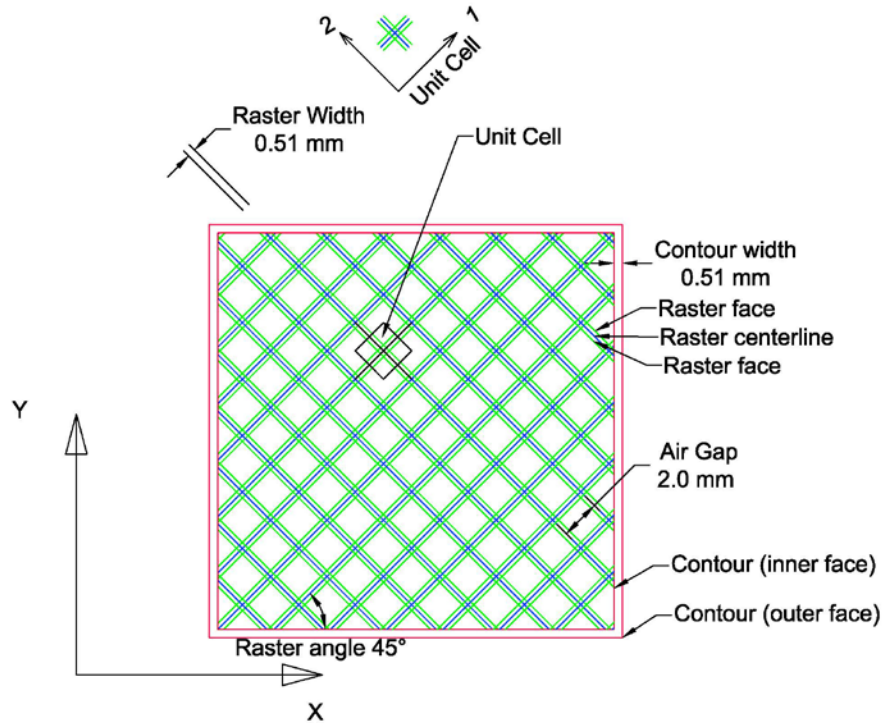


Figure 3.1: The internal structure of the printed material in XY plane (two stacked layers).

These the printing parameters were based on the preliminary tests carried out to determine the forming pressure and temperature that needs to be withstood by the mold. The mold for the preliminary tests was made up of ULTEM 1010 and was 3D printed by Stratasys (the manufacturer of Fortus 900mc systems used for this study). ULTEM 1010 is a commercial name for polyetherimide (PEI). ULTEM 9085 is a proprietary blend of PEI and other additives that make it more suitable for use in 3D printing. The additive reduces the shrinkage for ULTEM 9085 and lowers the melting point. A temperature of 325 °C is maintained at the nozzle of the extruder to liquefy ULTEM 9085. A temperature of 195 °C, which is higher than the glass transition temperature of 186 °C, is maintained in the oven so that the layer deposited earlier bonds better with the newly deposited layer. A better bond between the layers is obtained if they

are kept at a temperature above glass transition temperature but below melting temperature. This concept is explained by Pocius [45] as used in hot melt of adhesives.

Slight changes were made to those parameters to accommodate the fact that the material used for printing had been changed from ULTEM 1010 to ULTEM 9085.

The internal structure of two printed layers stacked one above another in XY plane is shown by Figure 3.2. This structure repeats itself in Z direction for a specified number of layers to create the final part.

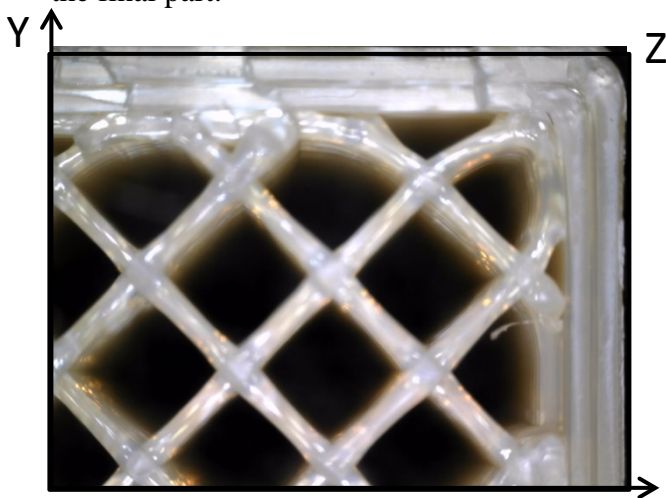


Figure 3.2: Internal structure in XY plane.

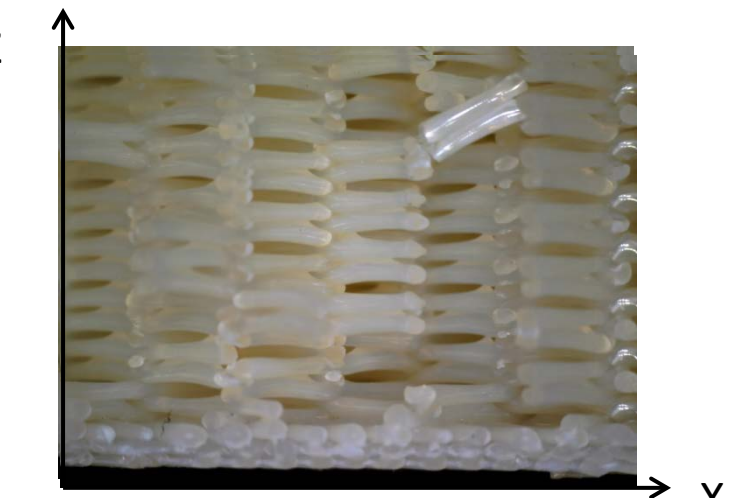


Figure 3.3: Internal structure in XZ plane.

Because the internal rasters were printed at an angle of 45 degrees, the YZ plane and the XZ plane internal structure were identical. Figure 3.3 shows the section of internal structure in XZ plane.

3.2 QUASI STATIC TESTS

Quasi-static tests were carried out to determine the properties of the 3D printed materials.

Filaments of ULTEM 9085 were tested in tension to determine the elastic modulus and strength

of the material. Several 3D printed specimens with lattice internal structure was tested in tension, compression and shear. The specimens were printed with different orientation to determine the mechanical properties (strength and elastic modulus) in different directions. For tension tests, six samples were printed with their Z-direction aligned with the direction of loading. Six additional samples were 3D printed with their X-direction aligned with the direction of loading. These samples were made per ASTM D638 specifications with printing parameters as mentioned in Section 3.1. The samples printed along the X-direction aligned with the direction of loading failed in the transition region between the grips and the middle gauge segment. Therefore, new specimens with modified geometry were printed to ensure that the failure was contained in the gauge region.

Similarly, for compression tests, six samples were printed with their Z-direction aligned with the direction of loading and another six samples were printed with X-direction aligned with the direction of loading. These samples were made per ASTM D6641 specifications.

To determine the properties of the printed structure in shear, eighteen different specimens were printed, six of each with X, Y, Z directions respectively aligned with the loading direction.

ASTM D7078 specifications were used for the geometry of the specimens.

3.2.1 Tension tests of the filament

There are two reasons for carrying out these tests. These tests would allow us to characterize the variability in the elastic modulus of the material used for the test coupons. These tests would also establish a Young's modulus to define the mechanical property of the material itself.

ULTEM 9085 filaments used for printing were drawn out of the canisters and tested in tension for strength and elastic modulus. Six samples, each of 100 mm length, were prepared. The middle 50.8 mm was marked as the gauge section where extensometer would be attached. Three different measurements were taken within the gauge section to measure the diameter of filament using digital calipers.

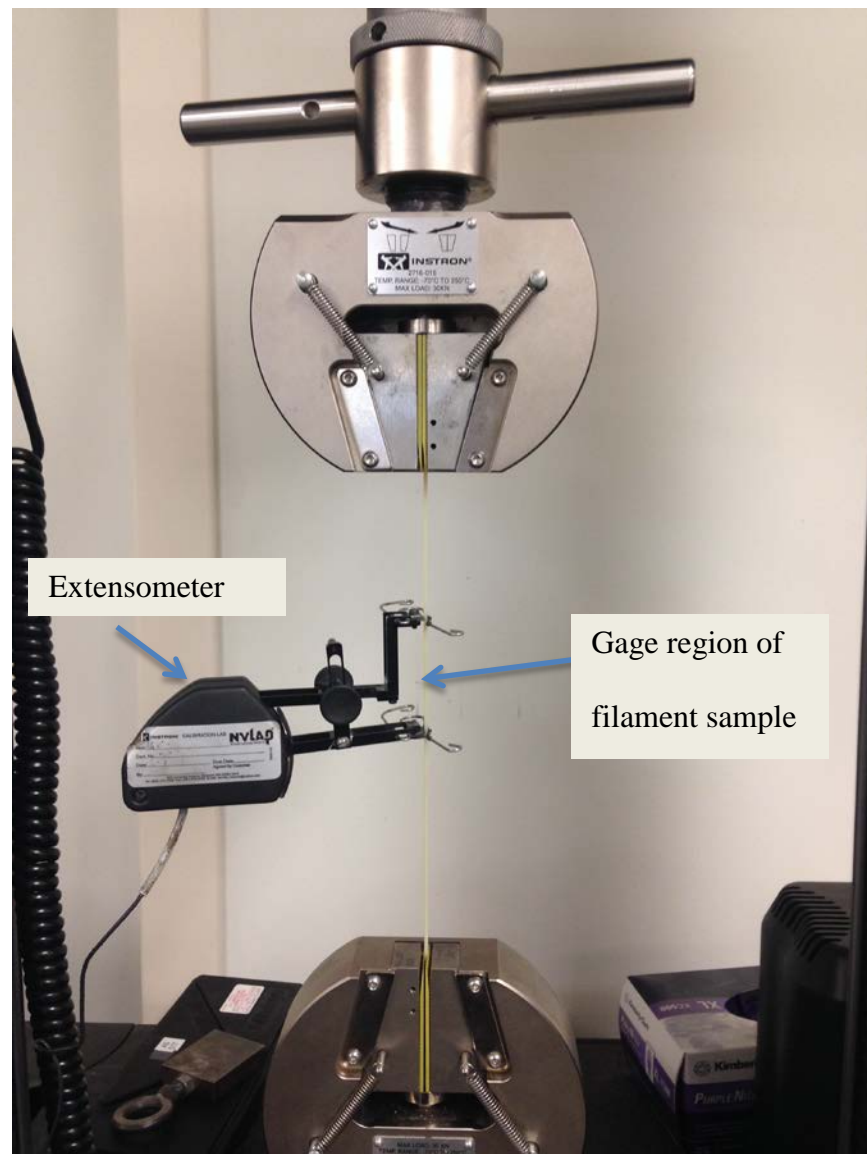


Figure 3.4: Test setup for tension tests of ULTEM 9085 filaments used for printing.

The mean of these measurements was taken as the diameter of the filament. Servo-hydraulic testing frame was used for the tests. An 8.9kN (2 kip) load cell was used to measure the loads. The extension of the filament was measured using an extensometer with gauge length of 50.8 mm (2 in).

Fixtures with clamping jaws were used to clamp the filaments during the test. Shear tabs were used to minimize the deformation of the filaments during clamping. This helped in delaying the initiation of yielding of the filament at the grips. This allowed nonlinear deformation to occur in the gauge region where extension was being recorded.

The rate of loading under displacement control was 0.1 mm per minute. The temperature of the room was 21.1°C during the testing. BlueHill 3 Testing software was used to record the data from the test.

3.2.2 Tension Tests of the printed material

For the tension tests, two different rounds of testing were done. In the first round, coupons of 15mm thickness were produced using 3D printing. The density of the fill in the grip section as well as that in the gauge section was equal for these specimens. The specimens printed with orientation towards Z- direction failed in the gauge section but the specimens printed with orientation towards X- direction failed in the transition region between gauge area and grip area. To ensure failure in gauge area, a second set of specimens was created for evaluating mechanical properties in X-direction. These specimens had a thickness of 5 mm and were printed with orientation along X direction. The fill was twice as dense in the grip region compared to the gauge region to ensure that the failure occurs in the gauge region. The linear cross-sectional

dimensions were measured using digital calipers to ensure that they match with the geometric computer model used for 3D printing.

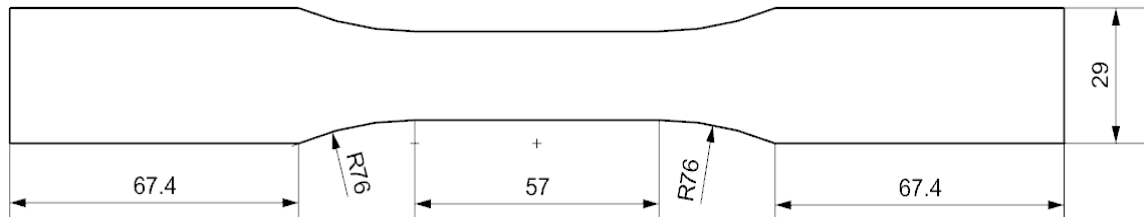


Figure 3.5: Tension test specimen for ASTM D638[47].

The rate of loading with displacement control was 0.1 mm per minute. The temperature of the room was 20.6 °C.

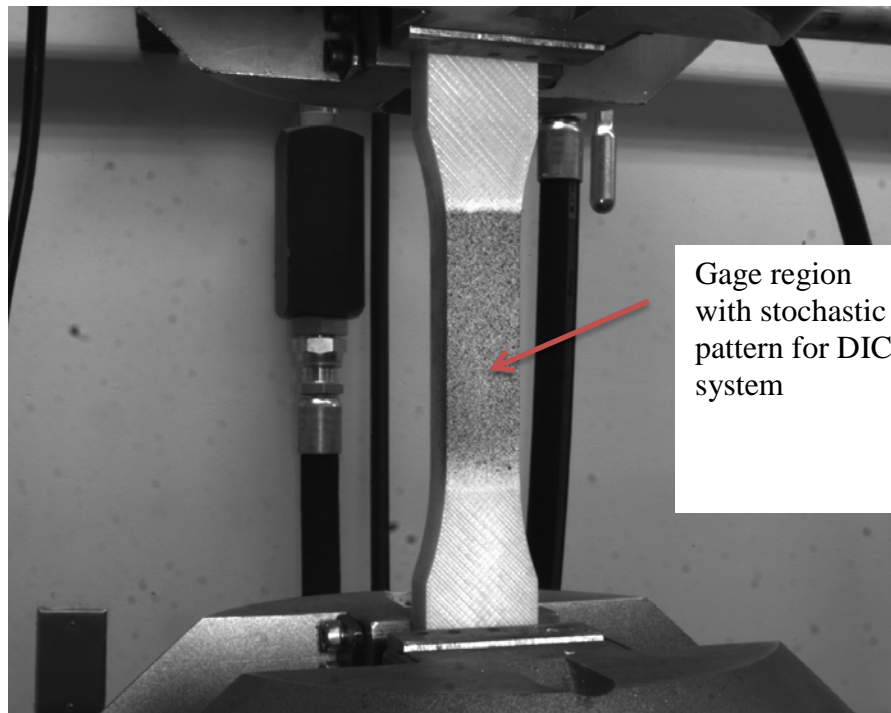


Figure 3.6: Tension test setup for coupons with lattice internal structure printed using ULTEM

9085.

3.2.3 Compression tests of the 3D printed test coupons

The compression tests were carried out in single round of testing. Two sets of samples were created with six specimens in each set. The first set had the Z-direction of the unit cell oriented in parallel with the direction of loading. The second set had X-direction of the unit cell oriented in parallel with the direction of loading. The cross-section of the samples was 12 mm x 12 mm. The gauge length was 13mm. A fixture in accordance with ASTM D6641 was used to ensure that the samples do not fail in buckling.

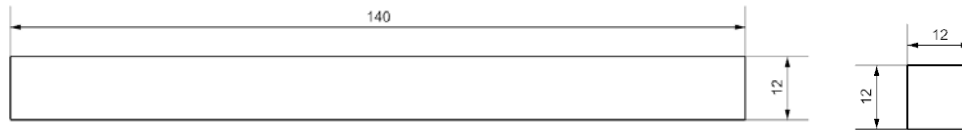


Figure 3.7: Compression test specimen for ASTM D6641 [48].

The rate of loading with displacement control was 0.1 mm per minute. The temperature of the room was 20.8 °C.

3.2.4 Shear tests of 3D printed specimens

The shear tests were also done in a single round of testing. Three sets of samples were made with six specimens in each set. The first set had X-direction of the unit cell oriented in parallel with the direction of loading. The second set had Y-direction of the unit cell oriented in parallel with the direction of loading. Similarly, the third set of specimens had Z-direction of the unit cell oriented parallel to the direction of loading. The rate of loading was 0.1 mm per minute. The temperature of the room was 21.1 °C.

3.2.5 Compression Tests of solid specimens

The solid specimens were tested in compression for two reasons. The first reason was to characterize the variability in the printed coupons due to the printing process of the machine without the effect of printing lattice structure. The second reason was to determine the Poisson's ratio of the ULTEM 9085 material.

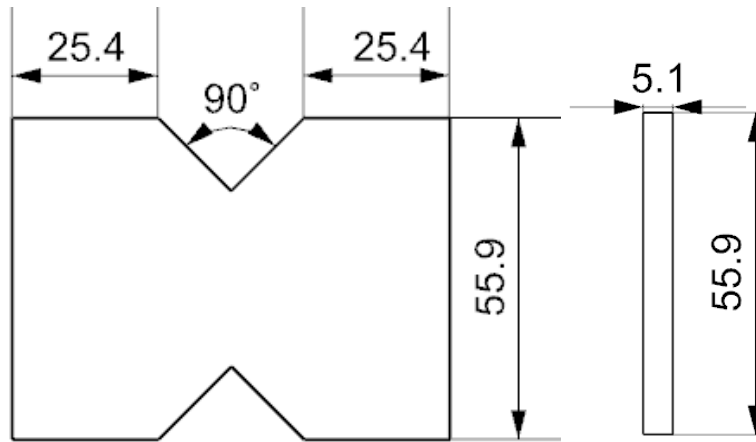


Figure 3.8: Shear Test Specimen for ASTM D7078[49] shear test.

Figure 3.8 shows the dimensions of the coupon specimens used for shear tests. The dimensions in the figure are in millimeters. Figure 3.9 shows the setup for ASTM D7078 rail shear test. The gage region is marked with stochastic pattern of black and white speckles. The changes in this stochastic pattern are analyzed by ARAMIS DIC system to calculate the strains.

A first set of samples were prepared. Two filament canisters were loaded such that when filament ran out of one canister, the machine would draw filament from another canister. The switching of canisters, drawing of filament and heating up of the filament tip took considerable amount of time.

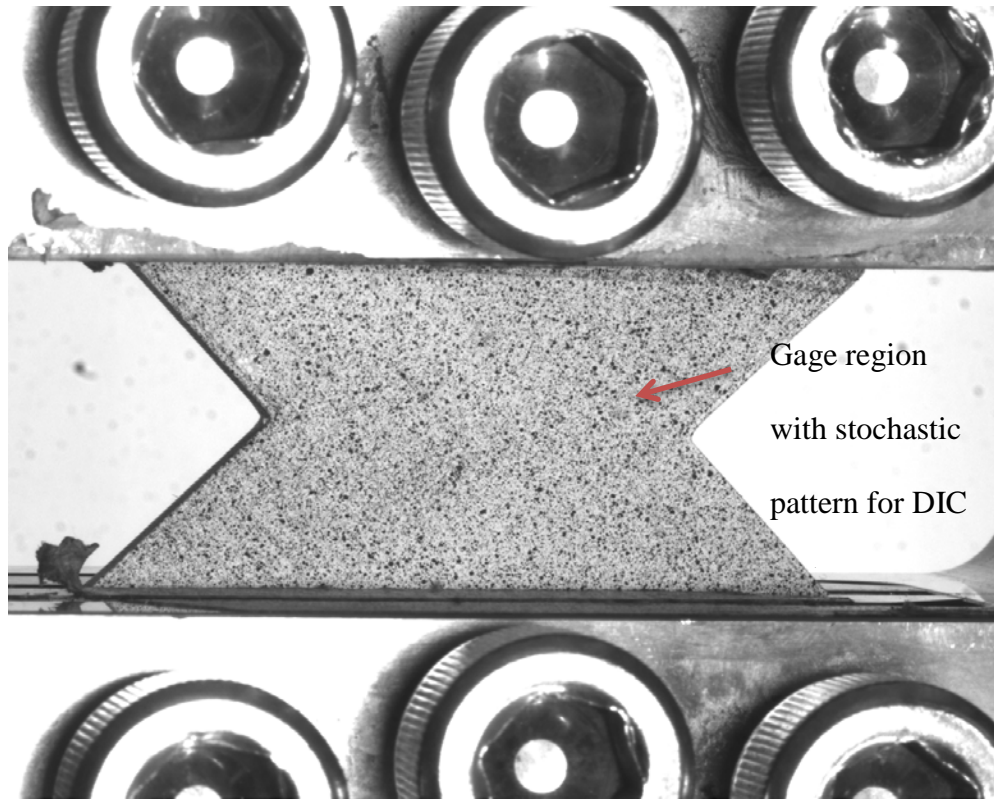


Figure 3.9: Shear Test setup of the specimen with lattice internal structures printed using ULTEM 9085.

During this time, the last deposited layer of filament and the new layer of molten filament would have significant temperature and viscosity differences. This would create inadequate weld between the filaments. There would also be certain amount of shrinkage due to the cooling down of the layers already deposited. This combined with the vibration of the machine when changing materials, would have caused a slight shift in the new layer of material deposited. This shift can be observed clearly in Figure 3.11. These specimens were discarded and new specimens were printed for the compression tests.

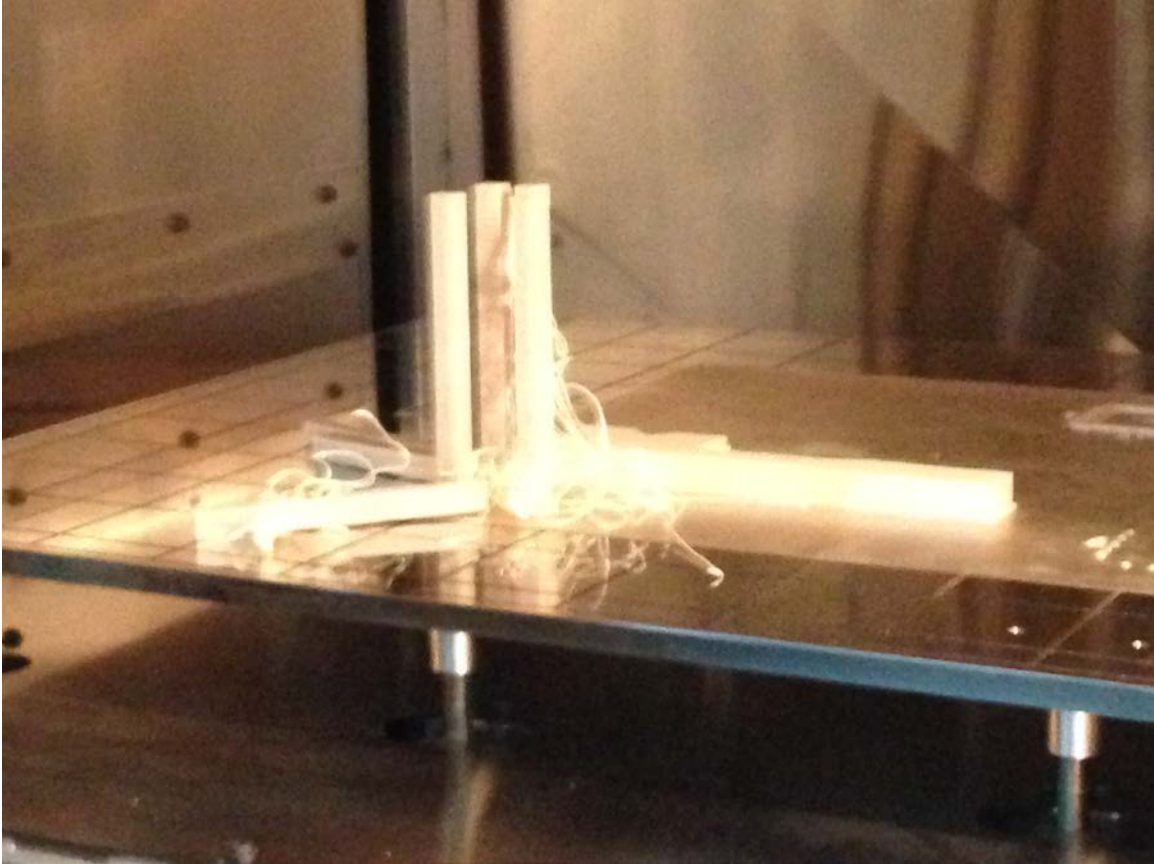


Figure 3.10: Samples showing shift and filament misplaced because of the sudden shifting of layers as seen through the glass window of the 3D printer oven.

It was also observed that such shifting happened two times during the printing. In two of the samples, the top few layers were not connected with each other properly. Hence, the incorrectly deposited layers made the samples unusable.

Another set of specimen were 3D printed. This time, it was ensured that filament from only one canister would be used for deposition. The wiping of tip with the metallic brushes after each layer of material deposition was confirmed. The specimens that were made this time were uniform, without any shift in layers of material deposited.

The specimens were tested using ASTM D6641, with a loading rate of 0.762 mm/min (0.03 inches/min). This value is slower than value prescribed by ASTM D6641. The strain rate was reduced to get more data points in the linear elastic region (between 1000 microstrains and 3000 microstrains) for calculation of elastic modulus. The strains were calculated using Aramis DIC system and load was applied using servo-hydraulic test frame with load being measured with a 100 kN (22 kip) load cell.

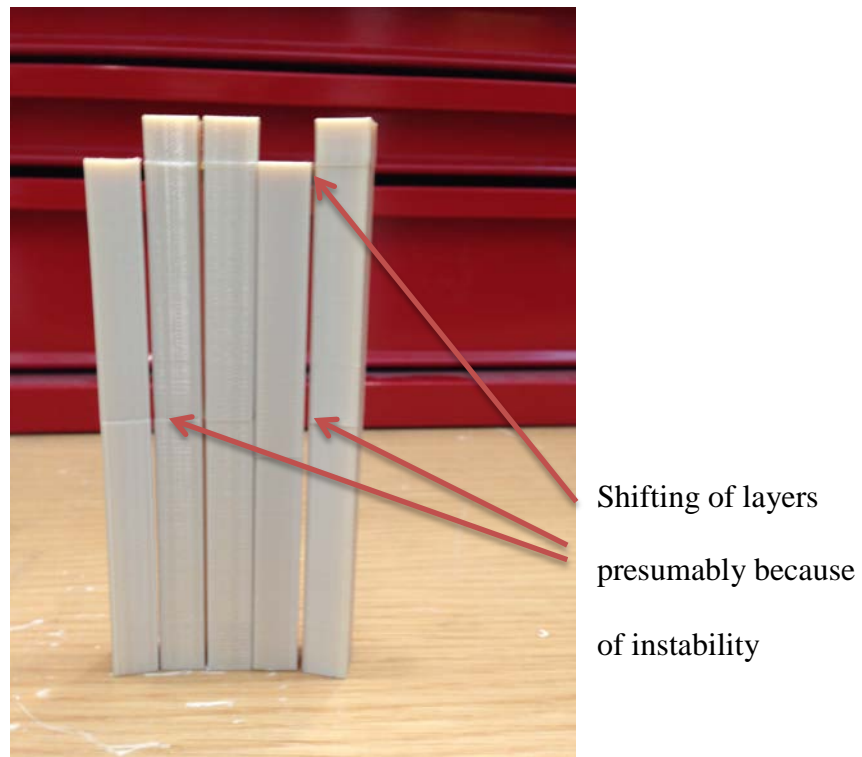


Figure 3.11: Coupons printed for compression tests showing shifting of alignment at certain layers.

3.3 EXPERIMENTAL RESULTS

3.3.1 Quasi Static Tests of samples with lattice internal structure

The results from the quasi-static tests on specimen with lattice internal structure are shown in Table 3.1.

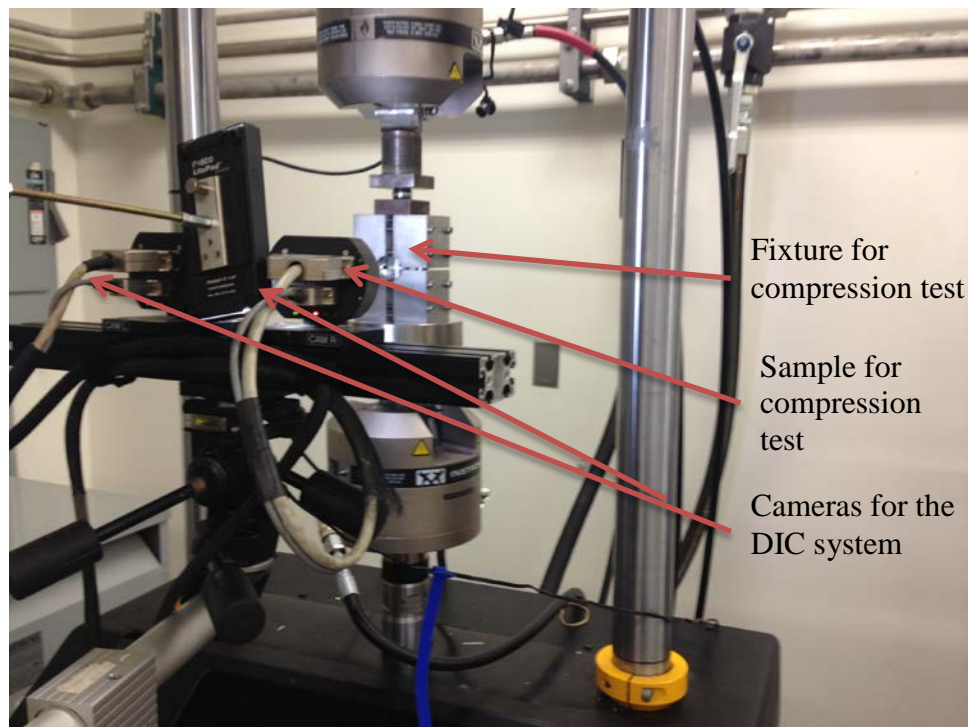


Figure 3.12: Set-up for compression test of solid-fill sample.

3.3.2 Quasi-static compression test of specimen with solid internal structure

An elastic modulus of 2250 MPa with a COV of 4.03% was measured from quasi-static compression test of specimens with solid (no air gaps) internal structure. The offset strength in compression at 2% offset was measured to be 90.4 MPa with a COV of 3.88%. The Poisson's ratio was measured to be 0.285 with a COV of 9.04%.

Table 3.1: Mechanical properties from quasi-static coupon tests with COV in parenthesis.

	Ultimate Strength (MPa)	Offset Strength (MPa)	Elastic Modulus (MPa)	Elastic Modulus Range (MPa)	Poisson's Ratio	Poisson's Ratio Range
ASTM D638 Tension X (or Y)	14.6 (4.51%)	-	1140 (4.92%)	1060 - 1220	0.376 (2.15%)	0.3682 - 0.3864
ASTM D638 Tension Z	13.3 (2.27%)	-	920 (2.89%)	888 - 962	0.242 (12.2%)	0.1856 - 0.2567
ASTM D6641 Compression X (or Y)	23.6 (2.41%)	22.5 (3.10%)	925 (8.75%)	835 - 1030	0.286 (10.8%)	0.2403 - 0.3413
ASTM D6641 Compression Z	38.0 (1.97%)	31.97 (5.79%)	1090 (12.55%)	990 - 1370	0.246 (18.9%)	0.1920 - 0.3077
ASTM D7078 Shear XY	12.5 (5.12%)	-	789 (6.97%)	693 - 838	-	-
ASTM D7078 Shear YZ	12.6 (4.03%)	-	814 (6.52%)	738 - 872	-	-
ASTM D7078 Shear XZ	13.6 (2.45%)	-	796 (4.66%)	766 - 864	-	

An ultimate compressive strength value could not be obtained because the specimens underwent deformation that equaled the gauge length that resulted in the fixtures being exposed to each other.

3.3.3 Tension test of filaments

The tension test of filaments showed elastic modulus to be 2860 MPa. The COV for this measurement was 3.18%. The offset strength of the filaments at 1% offset was determined to be

62.3 MPa with a COV of 4.84%. The ultimate tensile strength for the filaments could not be determined because the specimens slipped at the grips at about 3% strain.

3.4 DISCUSSION OF RESULTS

It was observed for the tension tests, that the elastic modulus in X-direction is higher than elastic modulus in Z-direction. This is a result of sample cross section being different in these two cases. For the samples tested in tension in the X-direction, the ratio of cross section area contributed by the core material to the cross-section area contributed by the wall material is higher compared to that for samples tested in Z- direction. After discounting the effect of wall mathematically, the calculated moduli of elasticity of core for both X and Z directions in tension are similar.

Similar observation is made for elastic modulus in compression. However, the sample sizes are the same. The cause of this observation can be explained by the fact that in compression, the contact area is increased as the voids are expelled, increasing the actual cross section area of the material. This increase in cross sectional area causes a corresponding increase in stiffness. This behavior is consistent with the behavior of cellular solids as mentioned by Gibson and Ashby [50].

From the test results, it was found that there was high variability in elastic modulus of the 3D printed material with lattice internal structure from sample to sample. The ultimate strength values were more consistent than the elastic modulus values.

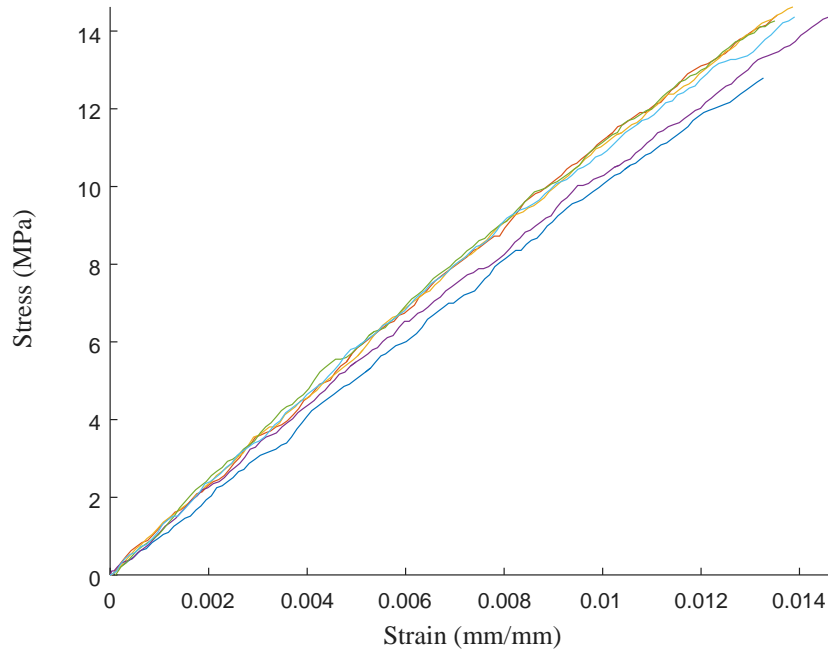


Figure 3.13: Stress Strain curves for samples with lattice internal structure under tension loading in the X-axis.

The samples exhibited brittle nature in tension which is consistent with the behavior of cellular solids as shown by Gibson and Ashby [50]. The stresses reached a peak value and the sample broke into two pieces. There was a clear separation between the two broken pieces and the plane of failure was normal to the plane of loading.

The stress-strain curves for samples with material Z- axis perpendicular to the direction of loading have lower variability compared to the samples with material Z-axis aligned with the direction of loading. The set of samples with low variability had a larger base area on the build sheet upon which the molten filament was deposited compared to that for the set of samples with higher variability.

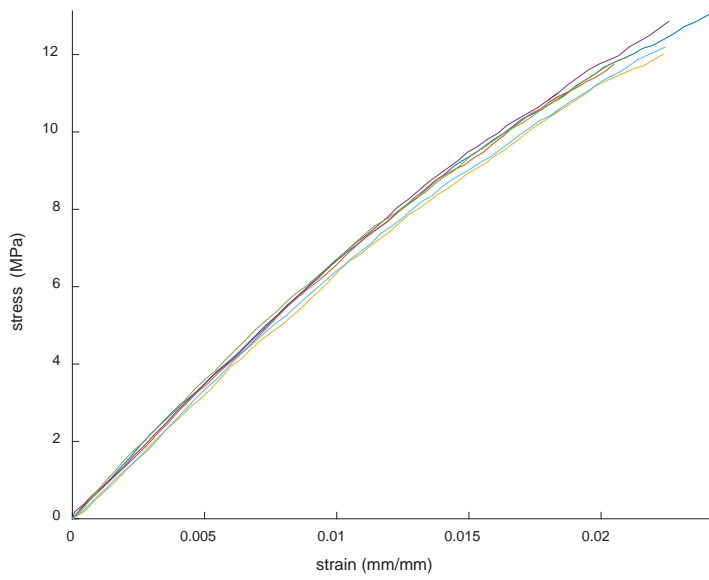


Figure 3.14: Stress-Strain curves for samples with lattice internal structure under tension loading in the Z-axis.

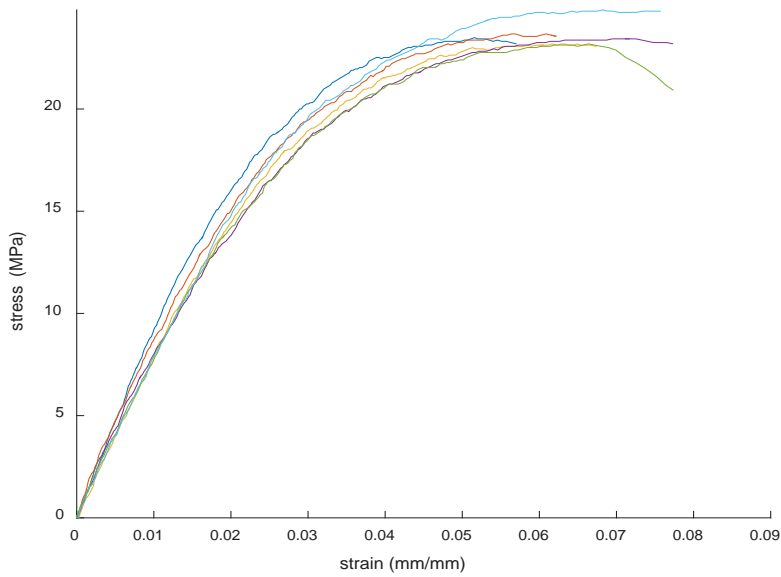


Figure 3.15: Stress-Strain Curves for samples with lattice internal structure under compression loading in the X-axis.

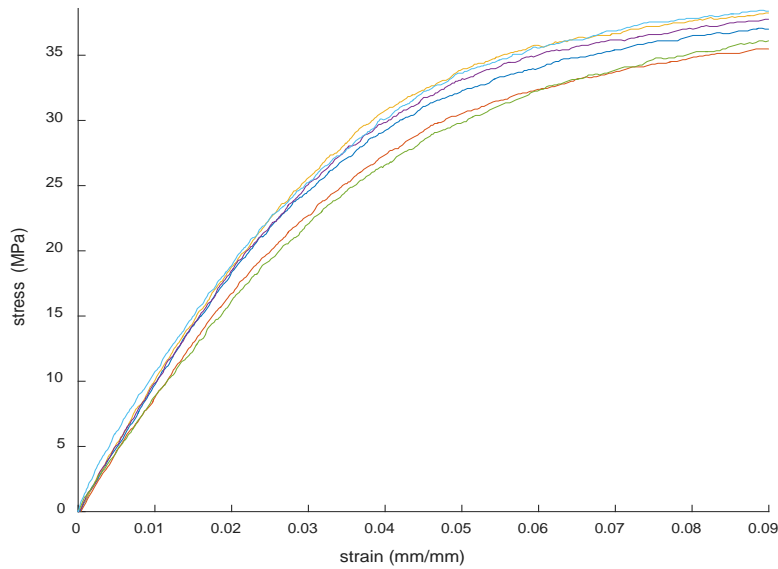


Figure 3.16: Stress-Strain Curves for samples with lattice internal structure under compression loading in the Z-axis.

The samples showed somewhat ductile behavior in compression. The stress-strain curves have an elastic region at low loading. On increasing the strain, the curves flatten out and show non-linear behavior. On further increasing the strain, load increases very slowly. The curves show three distinct regions of progression of failure in the material. This is because of the lattice internal structure. At first, the internal lattice structures undergo progressive failure, closing the air gap in between the material. The outer walls of the specimen start failing as the portion of load taken by the wall is increased. The outer walls buckle and fail, resulting in the failure of the specimen. This behavior is very characteristic of cellular materials as shown by Gibson and Ashby [50]. Another interesting observation was that the variability of elastic modulus among samples was high for set of samples with smaller base area in contact with the build sheet and the variability was smaller for the set of samples with larger base area in contact with the build sheet.

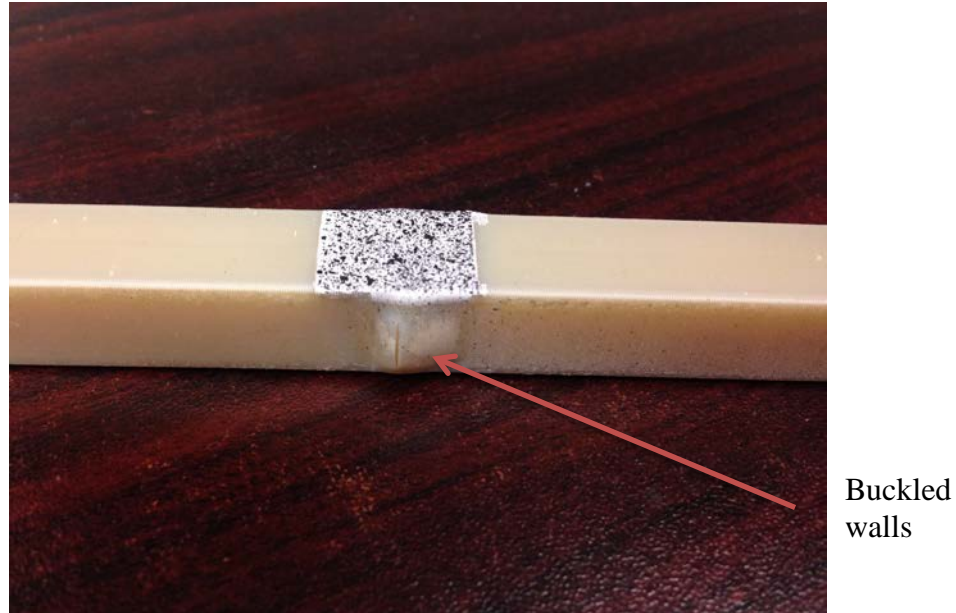


Figure 3.17: Failure of a sample loaded in compression with walls failed in buckling after crushing internal lattice structure.

The shear failures were all brittle failures. For samples of set S3 where the material XY plane aligned with the shear load plane, the failure plane was at the v-notch. For other two sets, where material XY plane was normal to the shear load plane, the failure plane started at the V notch, but it deviated at an angle. It was observed that variability in strength from sample to sample for each set of samples was low. However, the variability in shear modulus from sample to sample, for each set of samples was high and direct correlation was observed with base area in contact with the build sheet.

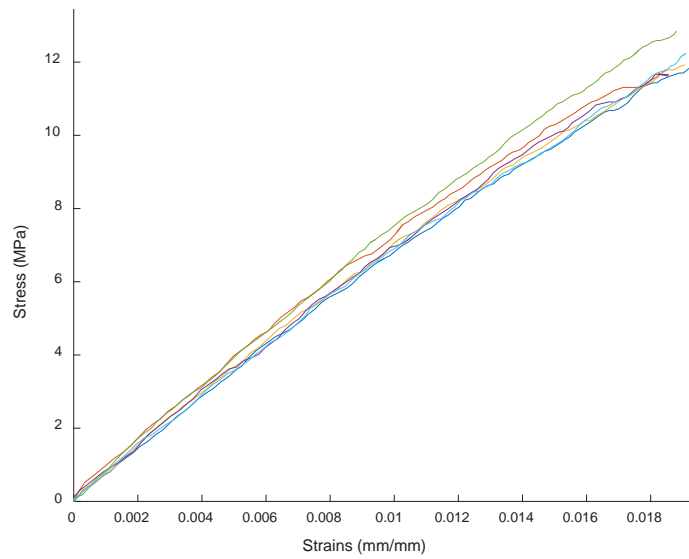


Figure 3.18: Stress-Strain curves for samples with lattice internal structure under shear loading in the the YZ plane.

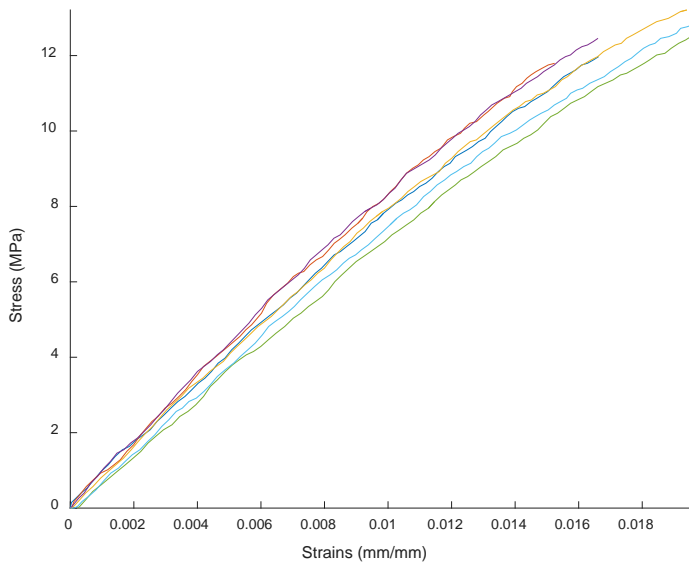


Figure 3.19: Stress-Strain curves for samples with lattice internal structure under shear loading in the XZ plane.

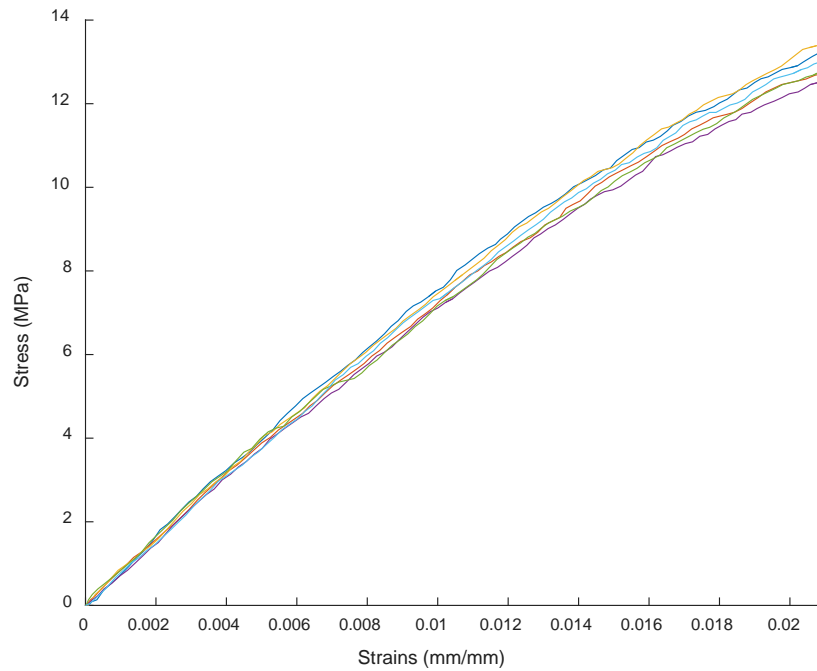


Figure 3.20: Stress-Strain curves for samples with lattice internal structure loaded in shear in the XY plane.

The variability in the elastic modulus of samples appeared to be influenced by two main factors, namely, the base area in contact with the build sheet, and the height of the specimen. Lower variability in elastic modulus of samples was observed when larger area was in contact with the build sheet and vice-versa. Taller samples, with height being measured from the build sheet to the top of the specimen in along the line of action of gravity, experienced higher variability from sample to sample. Assuming the variability is observed attributable to slight misalignment of deposited layers that adds up with increasing number of layers in Z-direction, it appears reasonable that greater base area would reduce variability among samples. This is because a greater base area makes the sample more stable and the misalignments are reduced. Similarly,

taller samples will have more layers and the chances of misalignment increases with increasing the number of layers. Thus, taller samples would have higher variability.

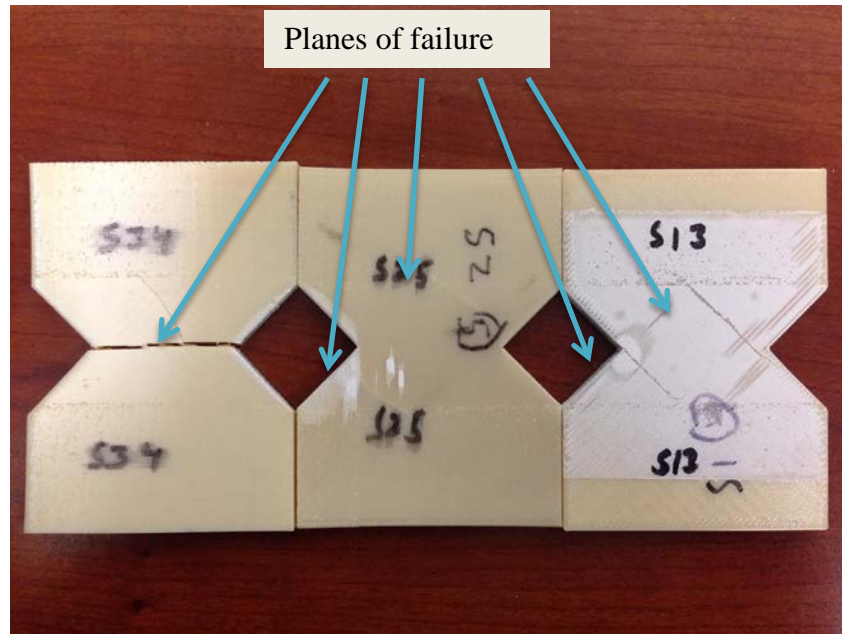


Figure 3.21: Samples showing failure planes on shear loading for different specimen printed with internal structures with different orientation.

To ensure that this variability is a result of the lattice internal structure and that it is not a result of the variability in the material, specimen with solid internal structure were prepared and tested. The configuration was made like samples loaded in compression in the Z-direction because those samples had highest variability in elastic moduli of the specimen. It can be seen from the stress-strain curve in Figure 3.22 that the stress-strain response of the samples has small variability for samples with solid internal fill compared to samples with lattice internal fill. Very low COV in elastic modulus was determined for the sample set with solid internal structure. The COV was

also low in tension tests of the filaments. The major sources of defects and hence variability are man, machine, method, material, measurement, environment.

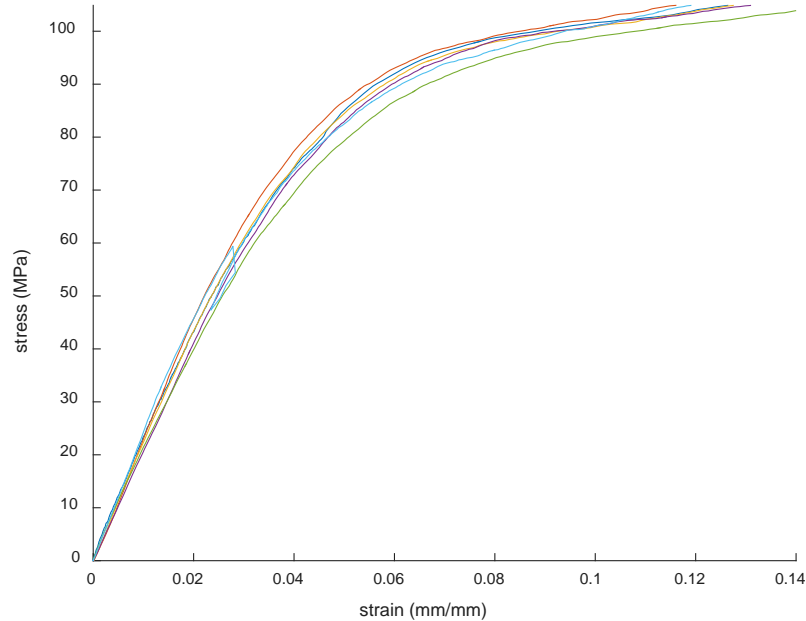


Figure 3.22: Stress-Strain curve for samples with solid internal structure loaded in compression in the Z-direction.

The man (operator) was the same. The machine used was the same Stratasys Fortus 900 mc. The material was shown to have a low COV. The measurement techniques used were the same. The environment is unchanged during manufacturing and testing. Hence, the only source of defect and hence variability was the method that printed the internal lattice structure. This indicates that printing specimens with lattice internal structure results in variability from sample to sample. The compression modulus of 2250 MPa is significantly higher compared to the compression modulus of 1930 MPa provided by the manufacturer. Offset strength at 1% measured as 90.4

MPa was lower compared to the compression strength (at unspecified strain) of 104 MPa provided by the manufacturer.

The material showed nonlinear, ductile stress-strain behavior that is typical of thermoplastic materials. At high strains, the stress-strain curve flattened out showing very little increase in stress with increasing strain. The material was relatively more ductile compared to thermoplastic composite parts with reinforcements that would be made from thermoforming process of the mold. The coupon specimens underwent deformation that equaled the whole gage length of 13 mm (0.5 inch) without reaching ultimate failure state.

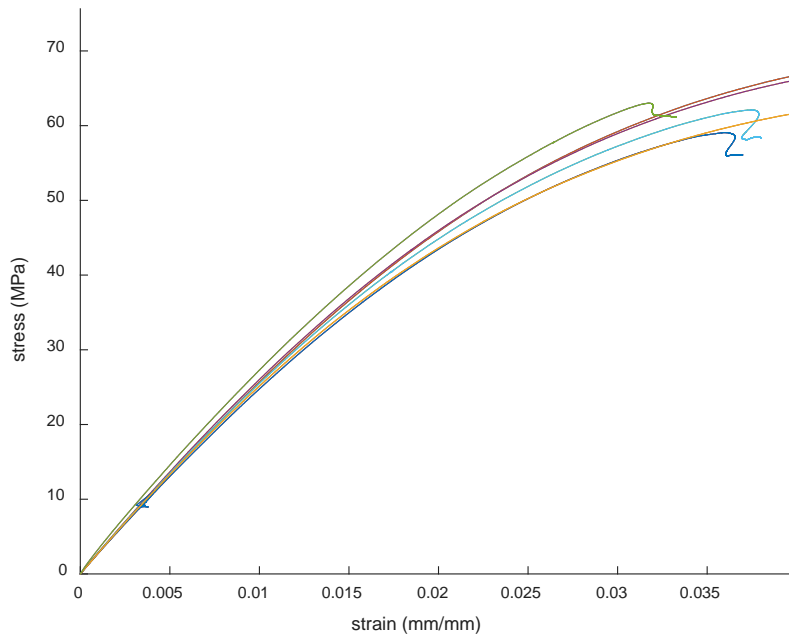


Figure 3.23: Stress-Strain curve for tension tests of filament.

The tension test of the filaments resulted in an elastic modulus of material as 2860 MPa which is significantly higher compared to the elastic modulus of 2220 MPa provided by the manufacturer.

Ultimate tensile strength could not be determined using the testing procedure used because the samples yielded at grips at higher loads. However, comparing the 1% offset strength of 62.3 MPa to the tensile strength of 71.6 MPa, the values are considerably close. The material showed relatively ductile behavior during tensile testing compared to the coupons with lattice internal structure in tensile tests. The curve flattened out with increasing strain. However, the filaments could not be tested to failure and the filaments yielded at grips before they yielded at gage. Hence, a comparison of ductility with compression tests could not be made.

3.5 CONCLUSIONS

The following conclusions were reached from the quasi-static tests:

1. The strength and modulus of elasticity of the material with cellular structure with parameters used for the study are sufficient to carry out thermoforming operations. However, the change in these properties with increase in temperature needs to be studied.
2. Parts printed with lattice internal structures exhibit a high degree of variability in elastic modulus but are in strength. The variability is likely to be the result of misalignment of the molten filament. The variability increases with increase in height and decreases with increase in base area in contact with build sheet. Parts printed with solid internal structures have comparatively very small variability suggesting that void ratio has a role to play in variability in mechanical properties of 3D printed structures.
3. The mechanical property values provided by material supplier differ from the results obtained from the experiments. The elastic moduli obtained from experiments are higher. The value obtained from experiments was 23.1% higher than the values obtained from the value provided by the material supplier. The 1% offset values for strength is close to the

strength values reported by the manufacturer. It would be better to carry out experiments to determine mechanical properties for modelling and other purposes rather than to rely on manufacturer-provided data.

CHAPTER 4

CREEP AND THERMAL PROPERTIES

Thermoforming operations require use of material at elevated temperatures. The mold needs to be able to maintain structural integrity at these elevated temperatures and pressure conditions. Since the thermoplastic material used for molds is a polymer, it exhibits viscoelastic response to external loading. The quasi-static tests only capture the elastic response portion of the material behavior. Characterizing a creep response should enable us to understand the behavior of the material under sustained loading and evaluate its potential use as a mold in the thermoforming process.

4.1 THEORY

4.1.1 Mechanical Behavior of polymers with respect to temperature

Figure 4.1 shows the temperature dependent behavior of the polymers. The crystalline and semi-crystalline polymers become less stiff gradually with increase in temperature. When the melting temperature is attained, the material starts to flow. For amorphous polymers, the glass transition temperature is important as there is a rapid decline in the storage modulus and hence the stiffness of the material.

Dynamical mechanical thermal analysis (DMTA) is one of the methods to determine the glass transition temperature of the polymers. The glass transition temperature is marked by sharp peak in $\tan \delta$, by sharp decrease in storage modulus or by sharp increase in loss modulus. If $T_{g,s}$, $T_{g,l}$, and $T_{g,t}$ are glass transition temperatures determined from storage modulus curve, loss modulus curve, and $\tan \delta$ curve respectively, the relationship between these temperatures can be expressed

as $T_{g,s} < T_{g,l} < T_{g,t}$. The storage modulus curve is used to determine the glass transition temperature as per ASTM standard [51]. Herzog et al [52] also suggest using the storage modulus for calculation of glass transition temperature so that the temperature at which mechanical properties begin to be compromised can be studied.

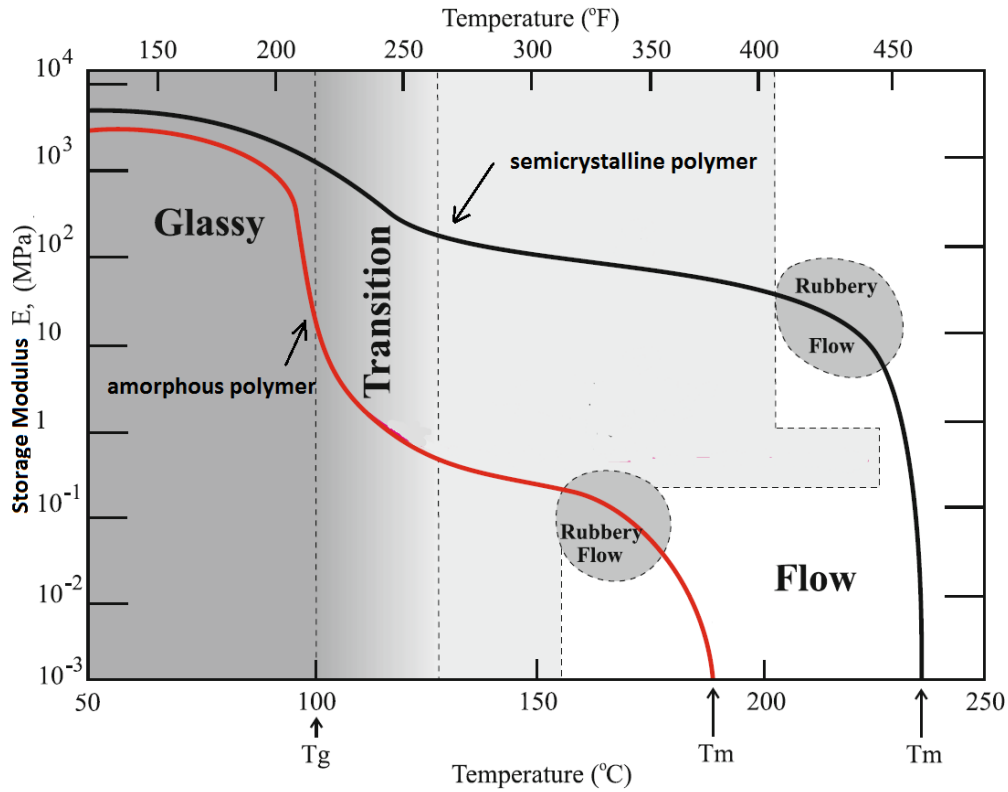


Figure 4.1: Temperature dependent behavior of polymers [46].

4.1.2 Mechanical Behavior of polymers with respect to sustained loading

The response of polymers is time dependent and viscoelastic. This time dependence is inherent to polymers because of their molecular structure. Two tests are commonly used to characterize the viscoelastic nature of the polymeric materials, namely, relaxation test and creep test.

In relaxation test, the polymer sample is given a strain and the stress in the material is measured over time.

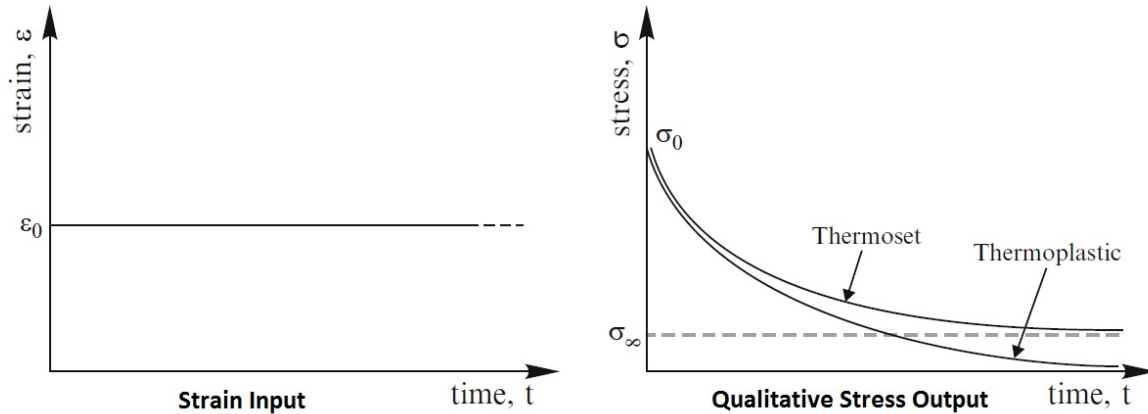


Figure 4.2: Relaxation test [46].

A creep test is another fundamental characterization test for viscoelastic materials. In this test, the sample is loaded at constant stress at zero time. The load is applied quasi-statically so as to avoid inertia effects. The material is considered to have no previous loading history.

Creep compliance is defined by equation (6).

$$D(t) = \frac{\epsilon(t)}{\sigma_0} \quad (6)$$

For thermoplastic materials, strain increases without bound with time for constant stress level.

The viscoelastic behavior of polymer materials can be modelled by using standard linear solid (SLS) model, also known as Zener model. SLS is the simplest model that predicts both creep and stress relaxation. The spring in parallel with the Maxwell unit has stiffness E_0 . It provides the rubbery stiffness that remains after the stress in Maxwell arm relaxes away as the dashpot

extends. The Maxwell arm and the parallel spring undergo equal strain. The total stress is the sum of stresses in each arm.

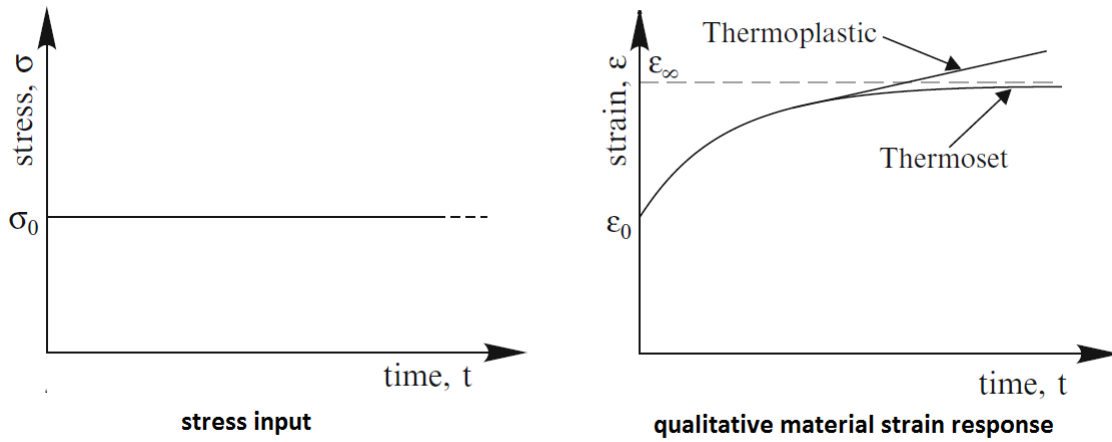


Figure 4.3: Creep Test [46].

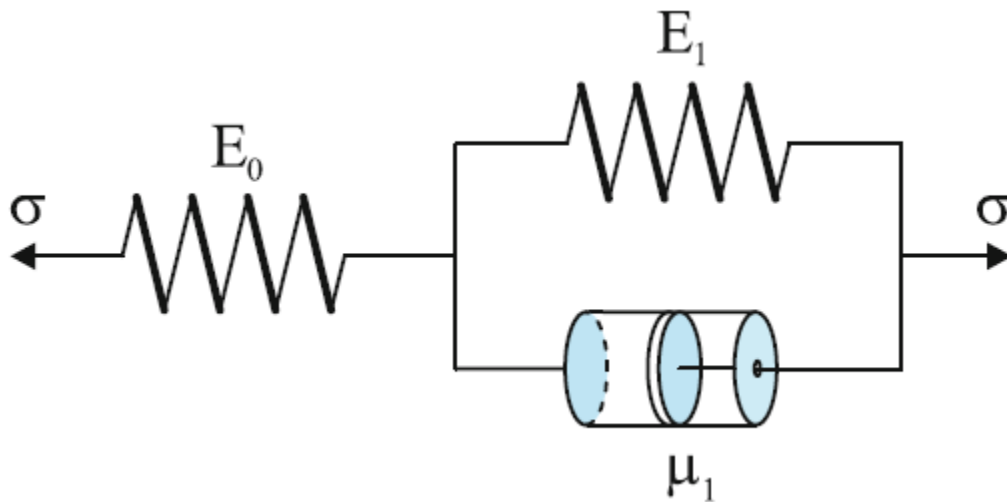


Figure 4.4: Maxwell form of Standard Linear Solid (SLS) model [46].

$$\epsilon(t) = \sigma_0 \left[\frac{1}{E_0} + \frac{1}{E_1} (1 - e^{-t/\tau}) \right] \quad (7)$$

This three-parameter solid model models the response of thermosets. For thermoplastic materials, however, the strain does not approach a fixed value asymptotically [46]. The strain keeps on increasing. To model this behavior, a flow parameter is added to the model, which is modelled by a viscous damper in series to the three-parameter solid model as shown in Figure 4.5.

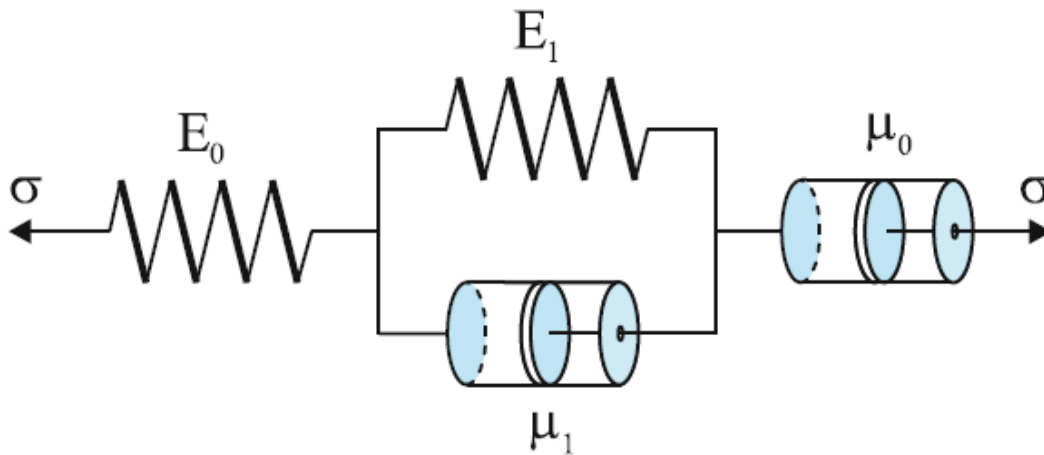


Figure 4.5: Four parameter fluid model [46].

The solution to four parameter fluid model is given by Equation (8).

$$\epsilon(t) = \sigma_0 \left[\frac{1}{E_0} + \frac{1}{E_1} \left(1 - e^{-\frac{t}{\tau}} \right) + \frac{t}{\mu_0} \right] \quad (8)$$

This represents a more general type of linear behavior for viscoelastic materials that is suitable for modeling the viscoelasticity of thermoplastic polymers. It includes instantaneous elasticity, delayed elasticity, and flow.

4.2 EXPERIMENTAL PROCEDURE

4.2.1 Dynamic Mechanical Thermal Analysis (DMTA) of filaments to determine glass transition temperature

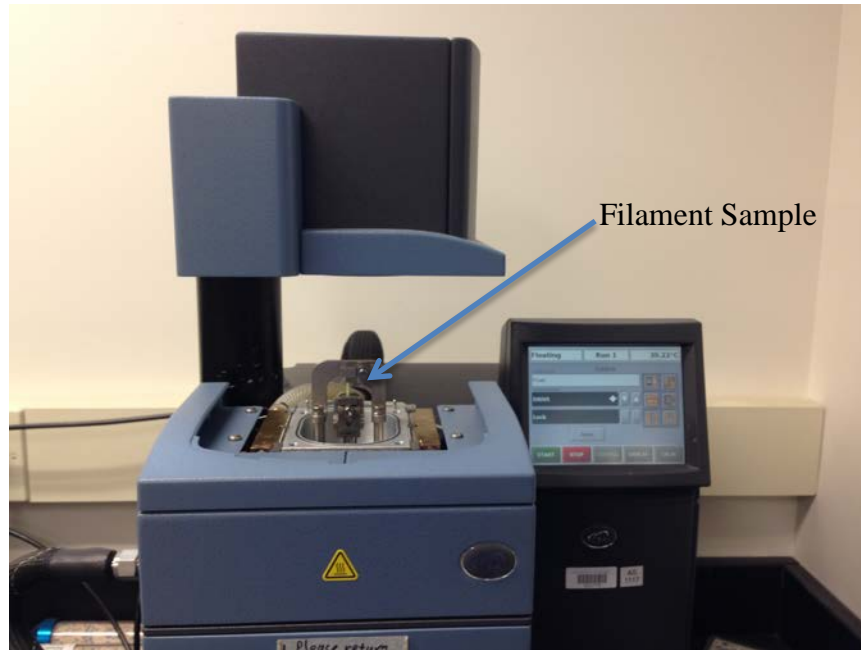


Figure 4.6: DMTA equipment with filament positioned between fixtures.

Five samples of filament were prepared and DMTA was carried out to determine the glass transition temperature of ULTEM 9085 filament materials. The test was carried out using TA Q800 equipment using a tension film fixture. The glass transition temperature provided by the material supplier was 186 °C. The temperature range for testing was from 150 °C to 210 °C. A frequency of 1 Hz was used for testing. The temperature of the oven was raised to 150 °C and was kept isothermal for 5 minutes. Temperature was ramped at the rate of 1 °C per minute and one reading per three cycles of dynamic loading was taken. Amplitude of 10 microstrains was chosen to ensure that the samples were in viscoelastic region of stress-strain response. The

storage modulus curve was used to determine the glass transition temperature. Tangents were drawn to two parts of storage modulus curves where sharp decrease is observed. The point of intersection of these two tangents is taken as the glass transition temperature. The testing procedure suggested by ASTM E1640-13 was followed. Figure 4.6 shows the setup for the tests carried out.

The setup for DMTA tests for filament is shown in Figure 4.6.

4.2.2 Creep tests of samples with lattice internal structure

Nine test samples were prepared with cross sectional dimensions identical to the samples used for compression test. The direction of compression loading was aligned with the Z-direction of the unit cell of the specimen. The compressive testing was conducted in accordance with ASTM D2990-09.

It was ensured that the correct load cell is installed and the correct fixtures were placed. A self-aligning head was prepared by mounting a ball bearing assembly above the platen that applied load to the test sample. The sample was placed at the center of the fixture so that any eccentricity related effects were eliminated. The strain gauges were bonded with the specimen by using epoxy adhesive. Special strain gauges, HBM 1-LD20-6/350 that could measure high strains up to 100,000 $\mu\text{m}/\text{m}$ (10%) were used. The strain at ultimate stress of the material was around 8%.

Using strain gauge that could measure up to 10%, strain would ensure that the measurements obtained would be reliable. A Data Acquisition (DAQ) system was set up using LabView that recorded the load data from the servo hydraulic testing frame with 10kN (2.2 kip) load cell. The voltage output from the strain gauges was used to calculate the strain.

The specimens were marked with numbers and the dimensions of the specimens were measured accurately up to nearest 0.05mm. The dimensions were taken as the mean of three different readings at different locations and were recorded to three significant digits. Three stress levels were used – 0.3, 0.5, and 0.7 times the ultimate compressive strength of the sample, and three specimens were tested at each stress level.

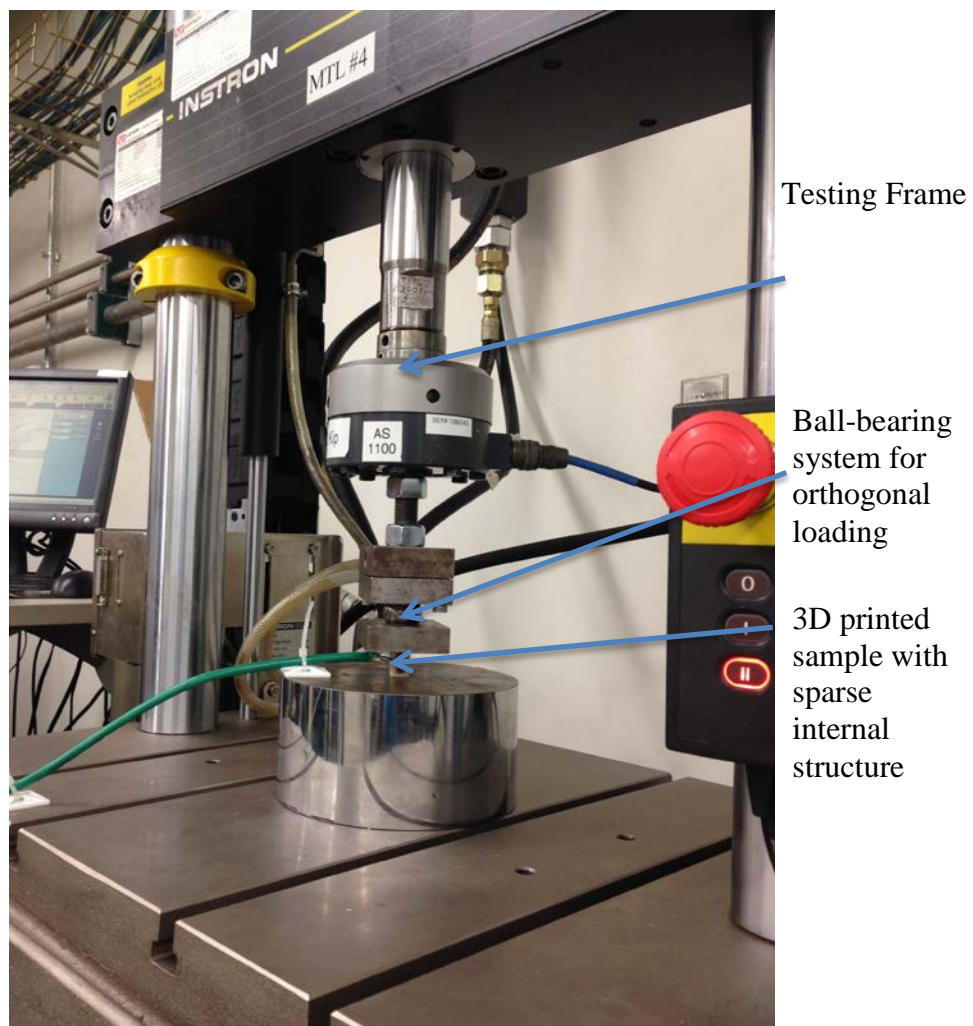


Figure 4.7: Creep test setup for samples with lattice internal structure loaded in compression in Z-direction.

The sample was loaded using a ramp loading function until it reached the required stress level. A strain rate of 0.127 mm/min (0.005 in/min) was used for loading. The loading was switched to load control after that event and a constant load level was maintained for the following 24 hours. The samples were monitored for de-bonding of strain gauge during the ramp loading stage and for the first few minutes of constant loading stage. The samples were also monitored for de-bonding of strain gauge at the end of the test before dismounting the sample from the fixture.

The setup for creep test is shown in Figure 4.7.

4.3 DISCUSSION OF RESULTS

Figure 4.9 shows the results of DMTA carried out on ULTEM 9085 filaments. It can be observed that the storage modulus has been reduced to around 1400 MPa at 150 °C. The elastic modulus of filament was calculated to be 2860 MPa at room temperature. This decrease in elastic modulus to half of its value at room temperature is very significant. This reduction in the elastic modulus should be considered while designing the mold for thermoforming operations.

Three different glass transition temperatures were calculated using storage modulus, loss modulus and $\tan \delta$ curves. The glass transition temperature using storage modulus, loss modulus and $\tan \delta$ were noted as 179.6 °C, 187.6 °C, and 198.7 °C respectively. Even though the glass transition temperature is at 179.6 °C, significant loss in elastic modulus already takes place at this temperature. Based on the glass transition temperature values, it seems prudent to limit the temperature of the mold material to 160 °C to limit the deformation of the sample under sustained loading. This is so that a comfortable gap between the glass transition temperature of the mold and the working temperature of the mold could be ensured. The effect of creep would

also be amplified at these elevated temperatures. This should be taken into consideration when designing the mold. Even though the sustained loads exist for short time (from a few seconds to a few minutes) during thermoforming operations, the elevated temperatures accelerate the creep deformation.

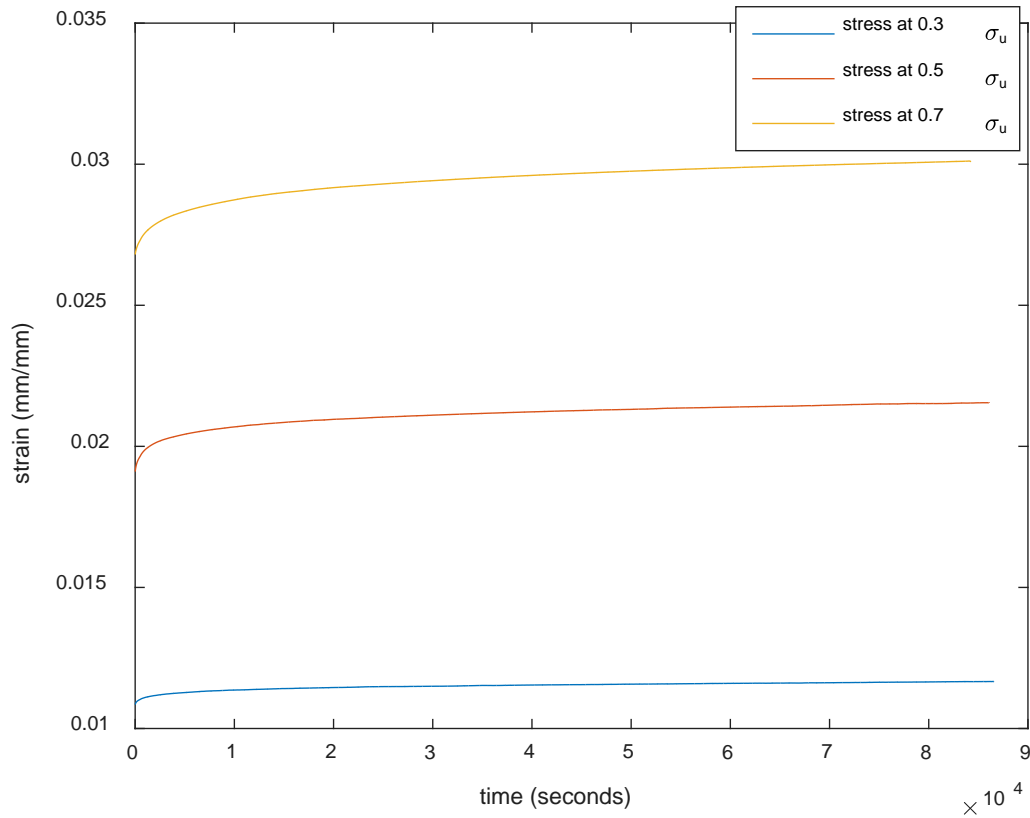


Figure 4.8: Creep response at different stress level for samples with lattice internal structure.

The creep tests carried out showed high variability from sample to sample. The fact that the samples showed high degree of variability in the quasi-static compression test (with a COV of about 19%) indicates some of the variability observed in these creep test is a result of the variability in the material itself. The slight misalignment of the deposited molten filament is

assumed to have caused this variability. It is observed that these misalignments have even morepronounced effects under sustained loads and affect the way the material with lattice internal structure deforms with time.

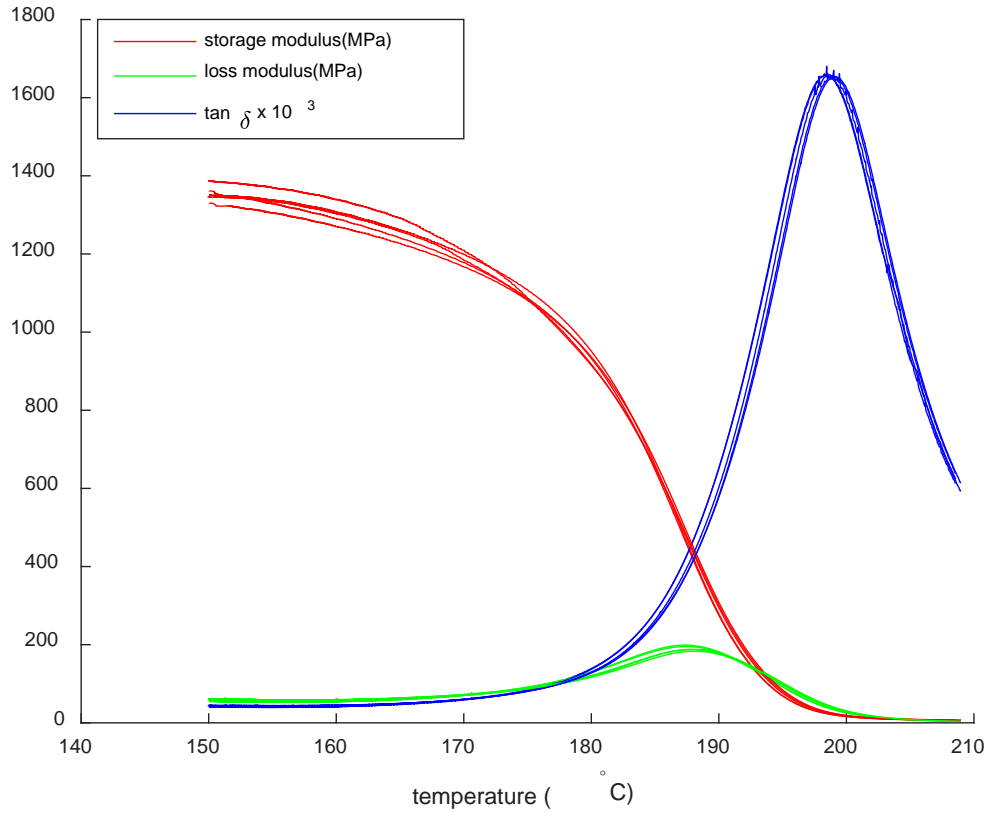


Figure 4.9: DMTA of ULTEM 9085 filaments.

Figure 4.10 shows the strain versus time curve for each of the samples at different stress levels. Figure 4.8 in the results section is created by calculating the average of the three curves at each stress level.

The initial strain at the sustained load value is increasing with increasing sustained load, i.e, initial strain at $0.3 \sigma_U$ is less than the strain at $0.5 \sigma_U$ that is in turn less than the strain at $0.7 \sigma_U$

for all the samples at respective stress levels. The initial strain for samples at each stress levels vary by a wide range. In Figure 4.10, it can also be seen that this range of variability is higher at higher stress levels – the range of initial strain at $0.3 \sigma_u$ is smaller compared to the range of initial strain at $0.7 \sigma_u$.

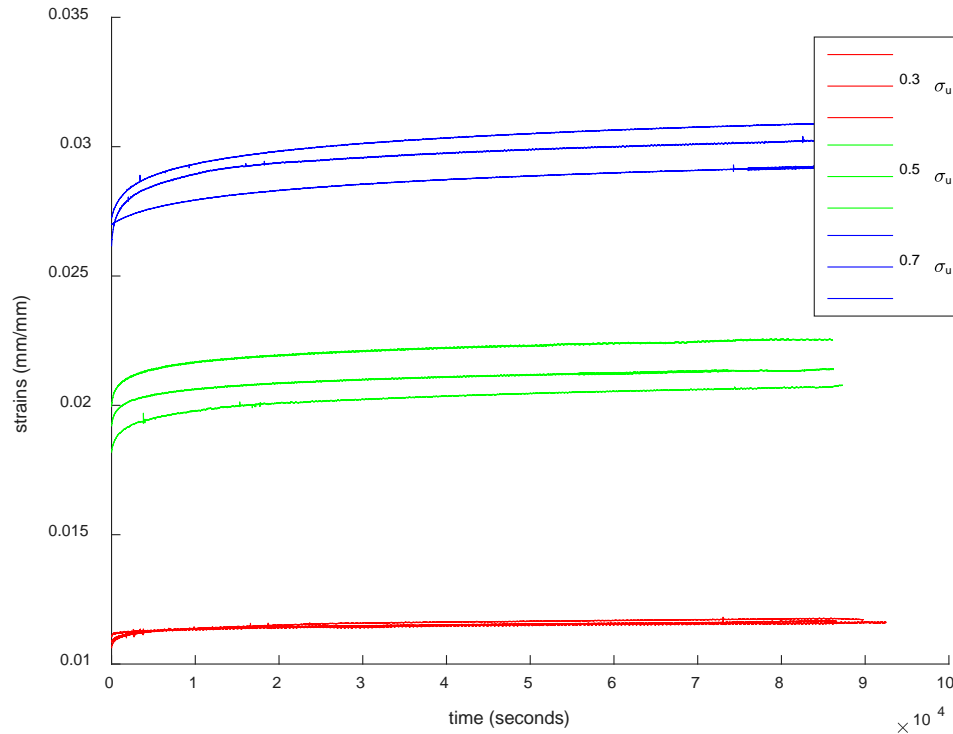


Figure 4.10: Creep Test results from each of individual nine tests.

Another notable feature in Figure 4.10 is that there is slight curvature in the first few thousand seconds during which the creep strain rises and essentially flattens out. This is in the primary creep region. Hence, the primary creep response of the material lasts for the first few thousand seconds. Figure 4.11 shows the creep curve for polymers. Tertiary fracture is not observed in the tests carried out as the tests were stopped at 24 hours of start.

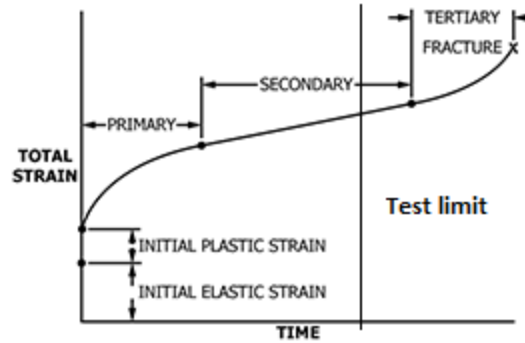


Figure 4.11: Typical creep curve for polymers [47].

This is more notable in samples loaded at $0.7 \sigma_u$. After the few thousand seconds, the rate of increase in creep strain is low. However, even at this slow rate, the creep strain keeps on increasing, which is a typical behavior for thermoplastic polymers.

4.4 DETERMINATION OF CREEP PARAMETERS

Two models were used for the determination of creep parameters. The first model is the three-parameter solid model, which is widely used for plastics, mostly thermosets. Equation (7) is the governing equation for the three-parameter solid model. The second model is the four-parameter fluid model, which is recommended model for thermoplastics. Equation (8) is the governing equation for four parameter fluid model.

The E_0 value used in these models is from the quasi-static compression tests. E_1 and τ for the Equation (7) were calculated using a least-square fitting method. E_1 was calculated to be 10600 MPa and τ calculated to be 1910 seconds. The residual error was 860 mm/mm.

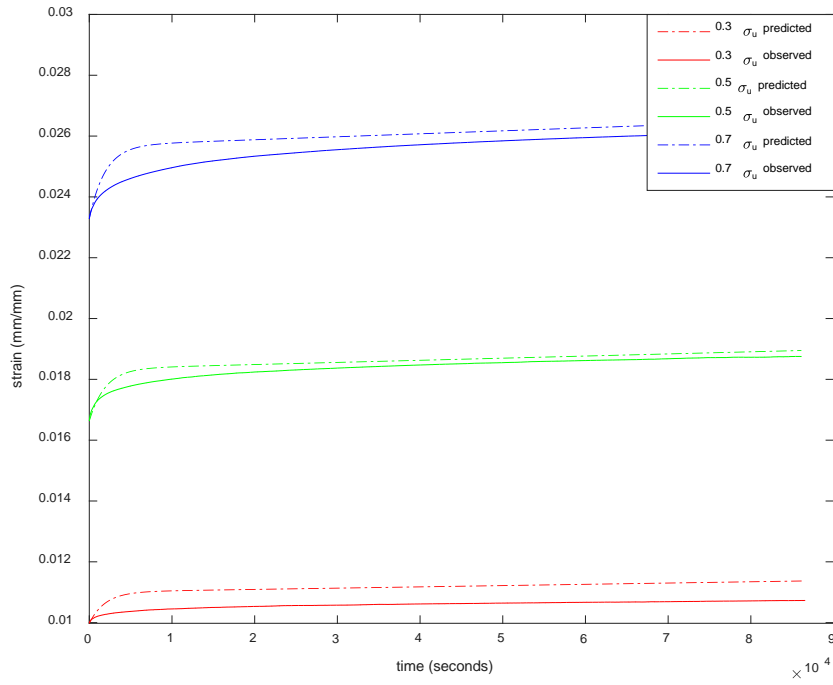


Figure 4.12: Curve fitting for three parameter solid model.

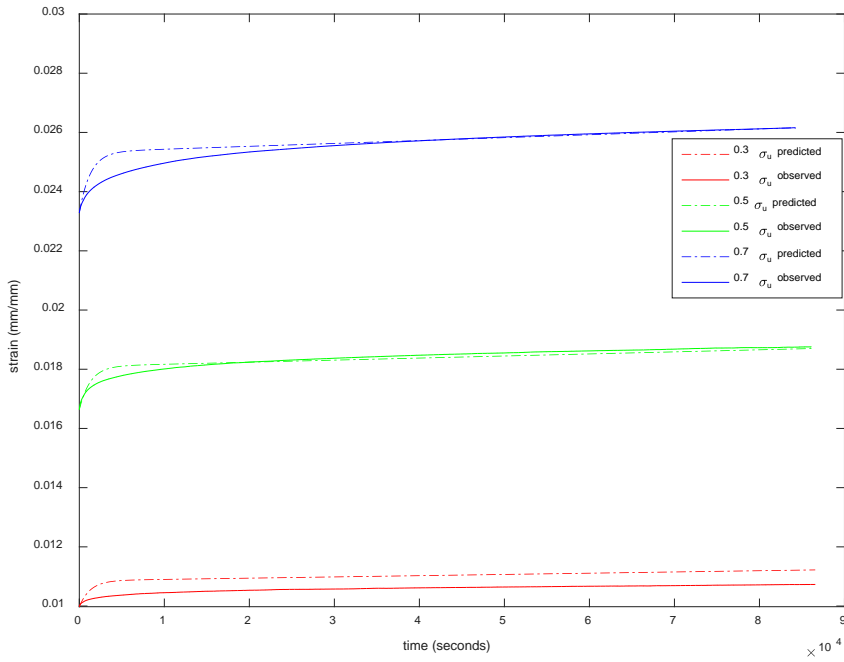


Figure 4.13: Curve fitting for four parameter fluid model.

E_1 , τ , and μ for Equation (8) were also calculated using a least-square fitting method. E_1 was calculated to be 12400 MPa, τ calculated to be 1280 seconds, and μ was calculated to be $2.6 \times 10^{15} \text{Ns/m}^2$. The residual error was 604 mm/mm.

4.5 CONCLUSIONS AND RECOMMENDATIONS

The following conclusions have been drawn and recommendations made from the DMTA and creep tests carried out:

1. There is significant decrease in the modulus of elasticity of the material at elevated temperatures. The elastic modulus was almost halved at 150 °C compared to the elastic modulus at room temperature. The strength of the material is also expected to be affected similarly by elevated temperatures. These facts must be considered while designing the mold. One way to minimize the effect of decrease in modulus of elasticity is to design the internal lattice structure to have increased modulus of elasticity at room temperature. For example, if the thermoforming operations are expected to raise the temperature of the mold made by using ULTEM 9085 material to 150 °C, the internal structure should be changed (the air gap parameter could be reduced) such that the elastic modulus of the generated structure is twice the required value. Because of this increase, the deformation of the mold at thermoforming temperatures would be within required limits.
2. The creep strains are small compared to the elastic strains. Even at the $0.7 \sigma_u$ stress level, the difference in the initial strain and the strain at 24 hours is small. The greatest increase in creep strain takes place during the first few thousand seconds. It can be asserted that at room temperatures, creep strains do not have greatly significant effect on mold behavior. At higher temperatures, however, the creep strains might be significant. But the molds need to carry the

sustained loads for a relatively short amount of time, in the range of a few seconds to a few minutes. Time – temperature superposition principle can be used to predict the effect of elevated temperatures for a few minutes by using the 24-hour creep test data.

3. The material with lattice internal structure is inherently variable and care should be taken while designing molds using these materials. A low value for strength reduction factor ϕ or a high value for factor of safety needs to be used depending upon the design philosophy used.
4. The four-parameter fluid model better suits the material compared to the three-parameter solid model. The viscous flow, although small, is significant. With a fitted value of $2.6 \times 10^{15} \text{Ns/m}^2$, the material is significantly less viscous than glass but highly viscous compared to common fluids.

CHAPTER 5

FINITE ELEMENT MODELING FOR ELASTIC RESPONSE OF 3D PRINTED PART WITH LATTICE INTERNAL STRUCTURE

The process of obtaining the required mechanical properties for a mold by varying the geometry of the lattice internal structure can be time consuming. First, the suitable parameters for air gap, contour width, raster angle, and slice height need to be guessed based on experience. Samples need to be made using these parameters and experiments need to be performed to determine the mechanical properties. Based on the mechanical properties determined from the experiments and the target mechanical properties required for adequate mold performance, further modifications to parameters defining internal structure should be carried out. Further testing needs to be carried out until required mechanical properties are achieved. This process is time consuming and negates the speed advantage of using 3D printing to manufacture the mold. A finite element model that is fast and reasonably reliable would help to speed up the process to determine an initial guess value for the required parameters. A balance between the accuracy of the model and the time taken by the model to compute has to be achieved for this purpose.

5.1 FINITE ELEMENT MODEL

The purpose of this numerical modeling is to create a simplistic model that can be analyzed with minimal computational effort in short time. The results from this model would help to define toolpath parameters like air gap, raster angle, deposition width, and slice height that determine the achieved strength and stiffness for the mold. An optimal lattice internal structure of the mold would result in less material use and manufacturing time.

A numerical model designed to represent the gauge section of the compression test specimen was developed. The model was a 3D space frame model with outer walls made up of shells. Tie constraints, with no relative displacement and rotation at common nodes, were placed between the outer shells and the internal lattice structure. Lattice models have been used to model the mechanical response of anisotropic materials. Davids et al [53] used a lattice model to predict the load-induced failure and damage in wood. Landis et al [54] used a lattice model to simulate microstructural damage in wood. The internal structure here has a physical lattice structure and not just modeled as one. Ashby [55] presents theoretical analyses of cellular structures that are actually lattices. In this chapter, a lattice structure surrounded by a shell is used to calculate the effective elastic modulus and Poisson's ratio for the test coupons.

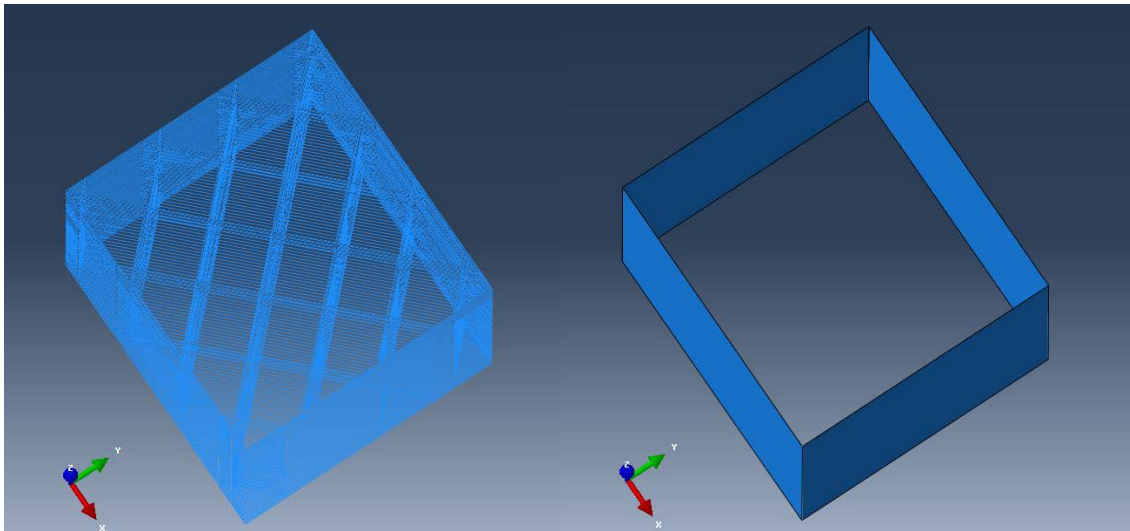


Figure 5.1: Schematic of 3D space frame on the left and shells surrounding the space frame on the right.

5.1.1 Symmetry and Boundary Conditions

The specimen was considered symmetrical and the bottom plane was assumed to have no displacement or rotation.

5.1.2 Materials

The 3D printing filament material was assumed isotropic for the amorphous mold material. The molecules of the polymer will align in the direction of extrusion of the filaments. However, the effect of alignment of molecules of polymer is not considered in this model. The modulus of elasticity from the quasi-static compression tests of the material with solid internal fill was 2860 MPa and the Poisson's ratio from the same test was 0.285. These values were used as input in the finite element model to calculate the deformation for fixed load in the linear-elastic region of the material response to loading.

FDM 3D printing works by depositing one layer of molten filament after another. The interface between these deposited filaments creates anisotropy in the material. The mechanical properties are different in different directions. The degree of this anisotropy depends on the area of the filaments that is in this interfacial area. For the model used here, the contact area between the layers of depositions is limited to the contact region between the deposited layers, which are modeled as columns. For the shells, two layers of filaments are deposited. This would create some anisotropy in the 3D printed parts. However, this was not taken into consideration and an assumption of isotropy for the material was made. This assumption is one of the sources of the discrepancies between the experimental values and the values obtained from finite element modeling.

5.1.3 Geometry and Sections

The internal structure of the specimen was made of stacks of filament, one over another, oriented at +45 and -45 degrees alternatively with respect to the X-axis. This internal structure was modeled using beam-column elements. The elements that were printed as filaments had a width of 0.51 mm (0.02 inch) and a height of 0.25 mm (0.01 inch). The connection points between two layers were modeled as column with a width of 0.51 mm and a height of 0.25 mm. For the external structure, shell elements were used.

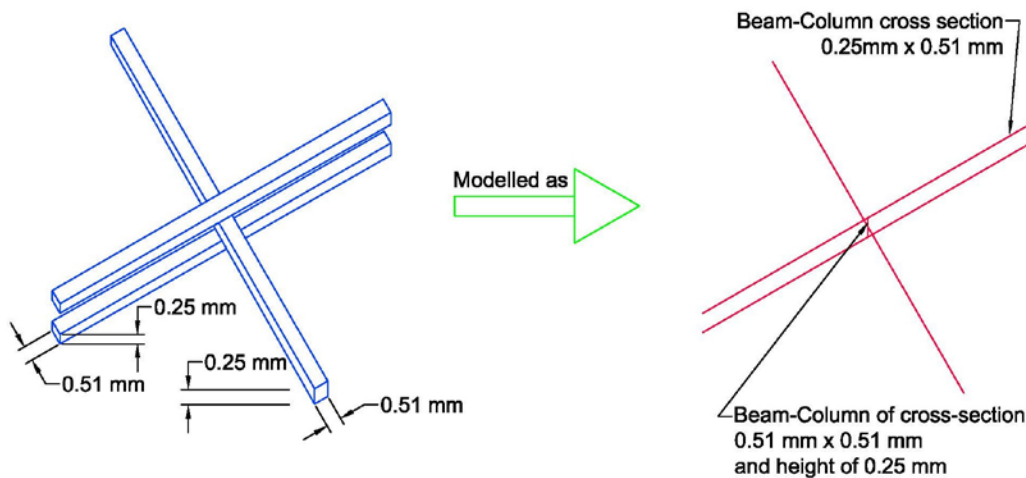


Figure 5.2: Sketch of the unit cell of internal structure and its representation in finite element model.

5.1.4 Compression in X direction

For compression in the X direction, shell elements with two different sections were used. The top nodes at $X = 13$ mm were kinematically coupled such that the displacement in Z-direction would be equal for all these nodes. A unit point load was applied at one of these nodes located near

Y=6.5mm and Z=6.5mm. The side plates on one side were given a thickness of 1.02 mm. The side plates on other side were given a thickness of 0.75 mm. This is because the test samples were printed in X-direction layer by layer. Because of this, the shell elements on the ZX and ZY planes had three layers of material each of width 0.51 mm. The shell elements on XY plane had only one layer of material that was 0.25 mm thick.

5.1.5 Compression in the Z direction

For compression in the Z direction shell elements with same thickness were used. The top nodes at Z = 13 mm were kinematically coupled such that the displacement in the Z direction would be equal for all these nodes. A unit point load was applied at one of these nodes located near=6.5mm and Y=6.5mm. The side plates were all given a thickness of 1.02mm. This is because the test samples were printed in Z-direction layer by layer.

5.1.6 Tension in the X direction

The model for tension in the X direction was similar to the model for compression in the Z direction. The difference was in geometry, which represented the actual tension tests carried. The second difference was in the loading. The unit point load was applied in positive X direction.

5.1.7 Tension in the Z direction

The model for tension in the Z direction was similar to the model for tension in the X direction. The difference was in geometry, which represented the actual geometry of the samples, and in loading, whereby unit load was applied in the positive Z-direction.

5.1.8 Shear in the XY plane

For shear in the XY plane, shell elements with two different sections were used. The side shells on one side were given a thickness of 1.02 mm, while the side shells on the smaller side were given a thickness of 0.75 mm. The top nodes in the model were kinematically coupled to have equal displacement in the Y direction. The boundary conditions of zero displacement in the Y and Z directions were enforced for nodes at $X = 0$ and $Y = 0$.

5.1.9 Shear in the XZ plane

For shear in the XZ plane, shell elements of same thickness were used. All the shell elements had a thickness of 1.02 mm. The top nodes were kinematically coupled to have equal displacement in the Z direction. The boundary conditions of zero displacement in the X and Y directions were enforced for nodes at $X = 0$ and $Z = 0$.

5.1.10 Assembly, elements, and meshing

The frame structure and the plates were assembled using tied translational and rotational constraints. The structure was meshed with maximum element size of 0.25 mm.

The beam elements were modeled as shear-flexible 2-noded linear beam elements. The shell elements were modeled as quadrilateral elements with finite strains. The drilling hourglass scaling factor value was set to zero. Enhanced hourglass control was used. Simpson integration was used as thickness integration rule. Five integration points were used. For the shear test models, triangular elements were used for meshing. This is because of the sharp angle at the V-notch in the geometry which could not be effectively meshed with quadrilateral elements.

A Finite Element model was used to predict the displacement under a uniform load. Then, the elastic modulus of the 3D printed structure was calculated using equation (9).

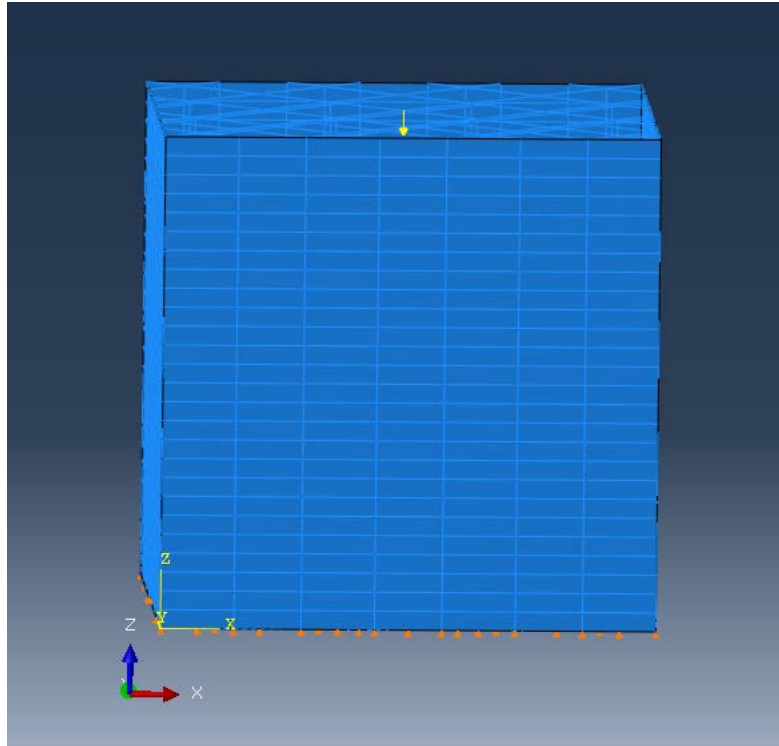


Figure 5.3: FEM element mesh for compression test coupon gage section (Loaded in Z-direction).

$$E = \frac{PL}{Ae} \quad (9)$$

where,

$$E = \text{Elastic modulus of the material} \quad (\text{N/mm}^2)$$

p	=	Force per unit area	(N)
L	=	Length of specimen	(mm)
e	=	Displacement of the top face	(mm)
A	=	Area of the top face where load is applied	(mm ²)

For the finite element of shear tests, the average of shear strains on all the nodes located on the front face were averaged.

$$G_{xy} = \frac{\tau_{xy}}{\gamma_{xy}} = \frac{P}{A_{xy}\gamma_{xy_avg}} \quad (10)$$

where,

G_{xy}	=	Shear modulus of the material in XY plane	(MPa)
τ_{xy}	=	Shear Stress	(MPa)
γ_{xy}	=	Shear Strain	(mm/mm)
P	=	Shear load applied	(N)
A_{xy}	=	Area of the top face where load is applied	(mm ²)
γ_{xy_avg}	=	Average shear strain in XY plane	(mm/mm)

Average shear strains were calculated by exporting the shear strain of all nodes in the front face of the model and using Matlab to calculate the mean of the shear strain values.

5.2 RESULTS

The elastic moduli obtained from FEM and the elastic moduli obtained from the experiments are listed and compared in Table 5.1.

Table 5.1: Comparison of Elastic Modulus from FEM and Elastic Modulus from Experiments.

	Elastic Modulus from Modeling (MPa)	Elastic Modulus from Experiments with range in parenthesis (MPa)	% difference
Compression in Z- direction	1160	1090 (990 -1370)	+5.2
Compression in X- direction	909	925 (835 - 1030)	-1.8
Tension in X - direction	1200	1140 (1060 -1220)	+5.5
Tension in Z- direction	903	921 (888– 962)	-2.0
Shear in XY Plane	726	789 (693 – 838)	-8.0
Shear in XZ plane	785	796 (738 – 872)	-1.4

Alternatively, the elastic modulus for compression in Z-direction can be calculated by using simple mechanics. The value can be obtained by calculating the cross-sectional area of the solid material that is normal to the force applied.

From Table 5.2, the total cross sectional area for the sample in compression in Z-direction is 67.0 mm². The total cross-sectional area for the specimen, including the air-gaps is 169 mm².

We have,

$$\frac{E_s}{E_m} = \frac{PL}{A_s e} * \frac{A_m e}{PL} = \frac{A_m}{A_s} \quad (11)$$

$$E_s = \frac{A_m}{A_s} * E_m \quad (12)$$

Using Equation (12), the value for elastic modulus of the sample can be calculated.

$$E_s = \frac{67.0}{169} * 2860 = 1130 \text{ MPa}$$

Where,

- E_s = Elastic modulus of the specimen
- E_m = Elastic modulus of the material
- P = Load applied on the specimen
- L = Length of the specimen along the direction of load
- A_s = Cross-sectional area of the specimen including the voids
- A_m = Cross-sectional area of the material only
- e = Extension (or compression) of the material along the length

The value of 1130 MPa obtained by using simple mechanics is very close to the value obtained from the finite element analysis with a difference of -2.58% compared to the value from finite element model. However, this simple analysis cannot be used to calculate the elastic modulus in

X-direction or Y-direction because the elements of the internal lattice structures are not aligned along the direction of the loading.

Table 5.2: Total cross-sectional area for compression in Z-direction.

Items	Area (mm²)	Number	Total (mm²)
Walls	13*1.02=13.3	4	53.2
Columns	0.51*0.51=0.260	53	13.8

Figure 5.4 shows the displacement in the direction of applied load for sample loaded in compression in Z-direction. The figure shows gradual variation in displacement with maximum displacement on the top face where the load was applied. Figure 5.5 shows the displacement in the direction of load for the sample loaded in compression X-direction. The displacement is comparable qualitatively in both compression test finite element models. The difference is that the deformation was higher when the coupons were loaded in X-direction than when they were loaded in Z-direction.

Figure 5.6 and Figure 5.7 show the displacements for the finite elements models of coupons loaded in Z-direction and X-direction respectively. The displacements are comparable qualitatively for the models but the displacement in Z-direction was found to be lower compared to displacement in X-direction. The mesh in X-direction has some triangular elements because the thickness of the coupon loaded in X-direction was thinner compared to the coupon loaded in Z-direction.

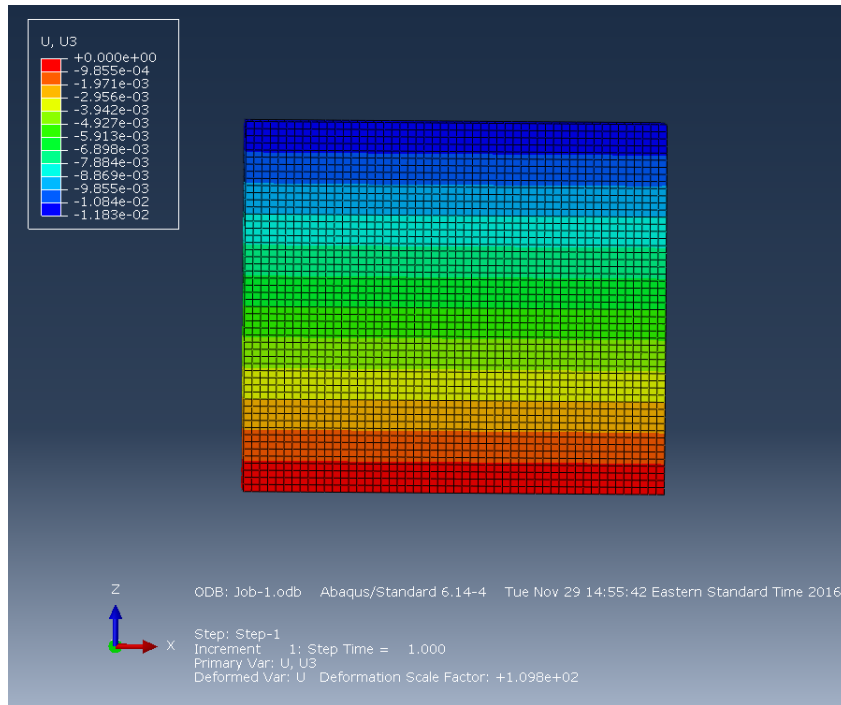


Figure 5.4: Displacements with compression loading in Z direction.

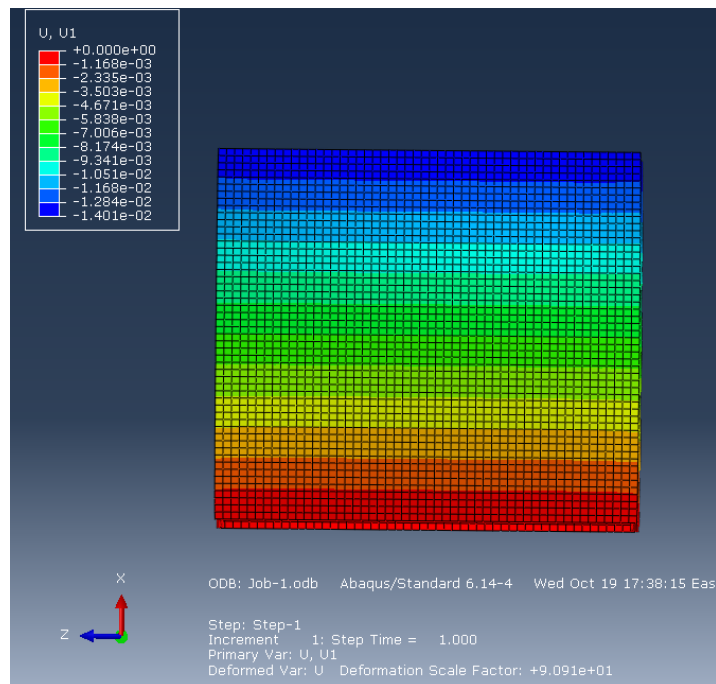


Figure 5.5: Displacements with compression loading in the X direction.

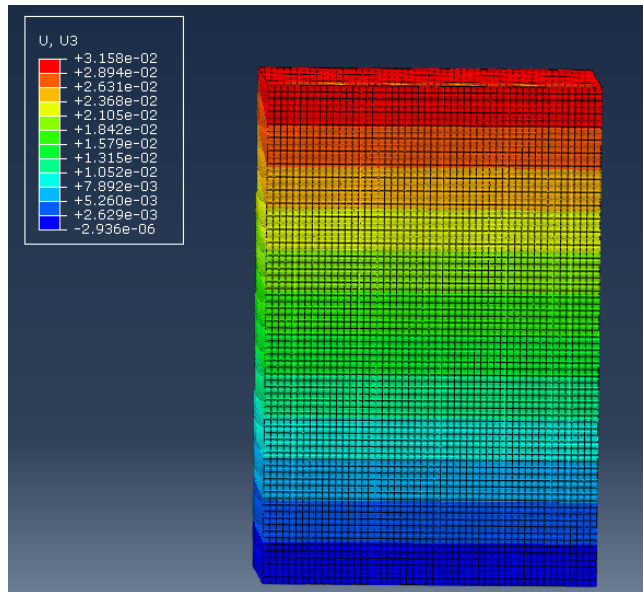


Figure 5.6: Displacement in the Z direction for the Finite Element Model loaded in tension.

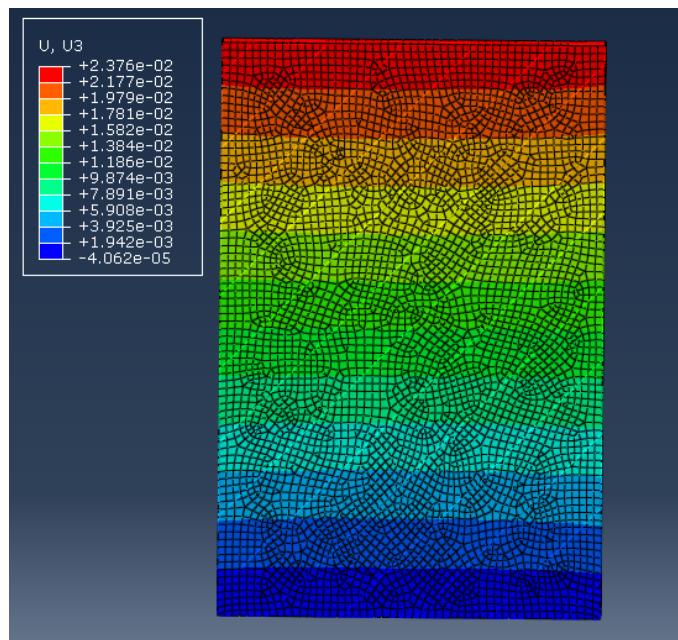


Figure 5.7: Displacement in the X direction for the Finite element model loaded in tension.

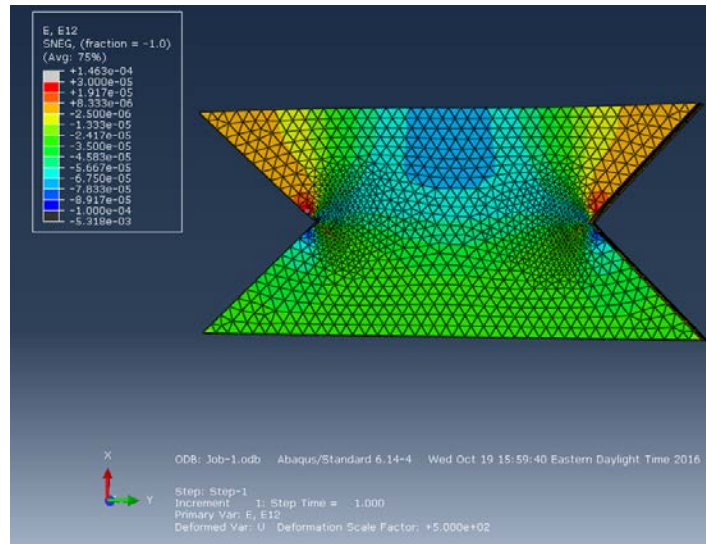


Figure 5.8: Shear Strains in the XY plane for the Finite Element model loaded in shear.

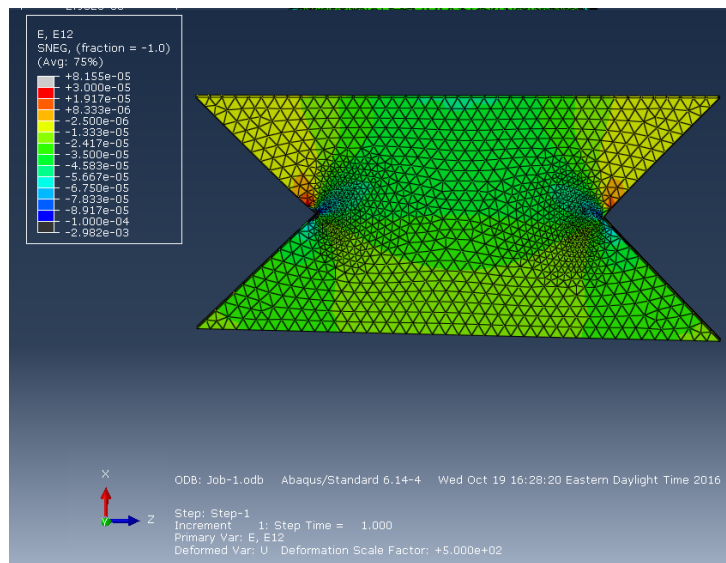


Figure 5.9: Shear Strain in the XZ plane for the Finite Element model loaded in shear.

Figure 5.8 and

Figure 5.9 show the coupons loaded in shear in XY and XZ planes respectively. It was observed that the stresses are concentrated around the V-notch corners. The mesh is significantly finer

around the V-notch to capture the stress concentration around the corners. For shear in XY plane, it was observed that the shear strains are higher at the area of application of the shear load and they gradually go down towards the V-notch.

The Poisson's ratios obtained from experiments is compared with those obtained from the finite element model are compared in Table 5.3.

Table 5.3: Poisson's ratio from FEM compared to Poisson's ratio from experimental results.

	Poisson's Ratio from Modeling	Poisson's Ratio from Experiments	% difference
ν_{XY} (compression test)	0.248	0.246	+0.80
ν_{XZ} (compression test)	0.235	0.286	-17.8
ν_{XZ} (tension test)	0.350	0.376	-6.9
ν_{XY} (tension test)	0.189	0.235	-19.6

5.3 DISCUSSION OF RESULTS

The values obtained from finite element modeling are considered reasonably close to the actual elastic modulus values determined from the experiment. The model is solved in a very short time (less than 4 minutes) on a decently powered laptop computer. The laptop computer had an Intel core i7 2860QM processor with four physical cores and 12 gigabytes of RAM.

When increasing the number of nodes, the change in the calculated values was insignificant. The model used here is a linear elastic model with a fixed value for elastic modulus and Poisson's ratio. A typical graph for convergence of the model is shown in Figure 5.10.

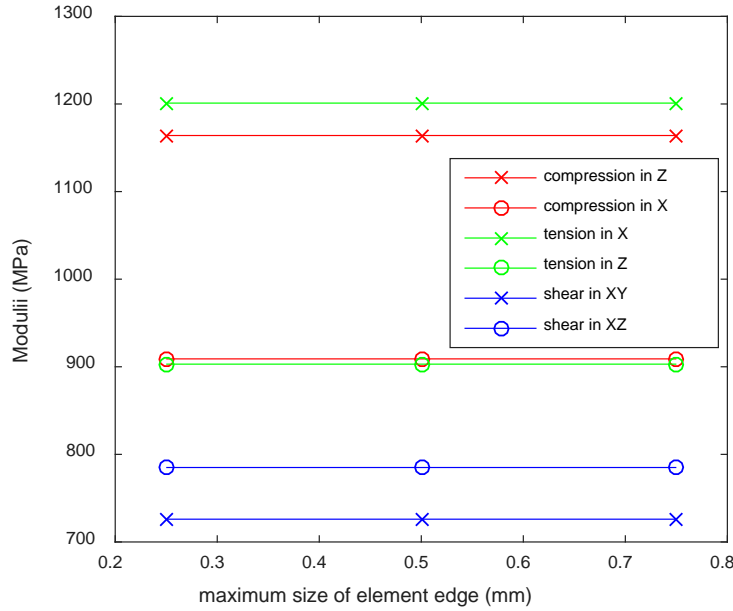


Figure 5.10: Convergence plot for E_z in compression.

5.4 CONCLUSIONS AND RECOMENDATIONS

1. A finite element model that is very basic and economical in terms of usage of computational resources can be used to characterize the linear elastic response of a 3D lattice printed coupon with reasonable accuracy. The finite element model can be used to determine the initial estimate of processing parameters of the 3D print. A more refined finite element model needs to be created if a more accurate response needs to be predicted or if the non-linear behavior of the material is expected because the loading is high.

2. The finite element model also does not consider the temperature and creep effects. The thermoforming operations are expected to be at temperatures higher than room temperatures. Effective modification to elastic modulus and Poisson's ratio in the input of the model should be made at temperatures below the glass transition where viscoelastic behavior of the material is less significant.
3. The model does not account for the anisotropy caused by the interfacial regions created when one filament deposition merges with the other. However, such interfacial regions are minimal in the lattice internal region and mostly present in the outer shell. This effect is also less significant in the 3D printer used because the diameter of the filament is very small and gaps between layers are insignificant. Hence, an assumption of anisotropy for the material itself is made and such assumption results in small errors. However, for solid fills and for parts printed with larger printers that extrude filaments with larger diameters, the assumption of anisotropy could result in greater errors and must be accounted for in modeling.
4. The elastic modulus obtained from tension test of the filament and the Poisson's ratio obtained from the compression test of solid samples are used in the Finite Element Model developed to predict the elastic response of the sample with lattice internal structure. The results from compression tests of the samples with lattice internal structure were compared with the results obtained from the finite element model and were found to be comparable.

CHAPTER 6

MOLD DESIGN AND MANUFACTURE

A part was created to highlight the advantage of using 3D printing for manufacturing molds. The web of a beam with sine wave web was chosen for this purpose. This is because it allows highlighting the features that can be implemented by using 3D printing to create a mold. The mold was designed to be a stamp-forming mold. Several dry runs were made to assess the problems that might arise during thermoforming and design features were added as a result. A finite element model of the mold was made with the cellular mold material modeled as an orthotropic material with an outer skin. The strains in the finite element model are compared with the strains observed during the experiments.

6.1 MOLD DESIGN

The part was designed to be a web of a sine wave web beam. Sine wave web beams are known to have high impact resistance [56] that is comparable to tubular sections. In a study performed by Hanagud et al [56], the sine wave beams gave similar energy absorption values compared to the tubular beams under bending. They are also shown to be more resistant to buckling of web and the buckling of the flange. They are used in wingspan spar for aircraft to eliminate the need for vertical stiffeners and hence reduce weight [57]. This part also has a complicated geometry that cannot be manufactured by well-established methods of thermoplastic composites manufacture. As a result, this part allows to showcase the advantages of using 3D-printing to design and manufacture molds for stamp forming of thermoplastic composites. A beam with sine wave web is shown in Figure 6.1. This beam was printed in the lab using Stratasys Fortus 900 mc printer

using ASA as the polymer. The part was printed as a demonstration for the final part that can be made using stamp forming.

The mold was designed using Siemens NX CAD software. A basic matched mold with male and female parts with the sine wave shape was first made. Several dry-run tests were carried out to determine the problems that might be encountered during thermoforming. Design features were added to counter the anticipated problem.

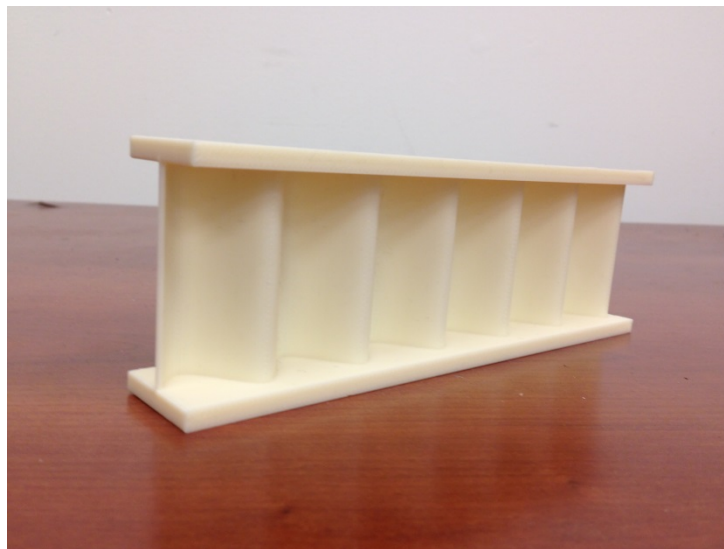


Figure 6.1: A beam with sine wave web printed using Stratasys Fortus 900 mc printer.

Several dry run tests were carried out to anticipate the problems that might be encountered while forming. A stack of pre-preg tapes were pressed without heating in a acrylonitrile styrene acrylate (ASA) mold. In this case, as shown in Figure 6.3, the central part was bending. In the next design iteration, bending was minimized by creating solid circular section at the center during the 3D printing process.

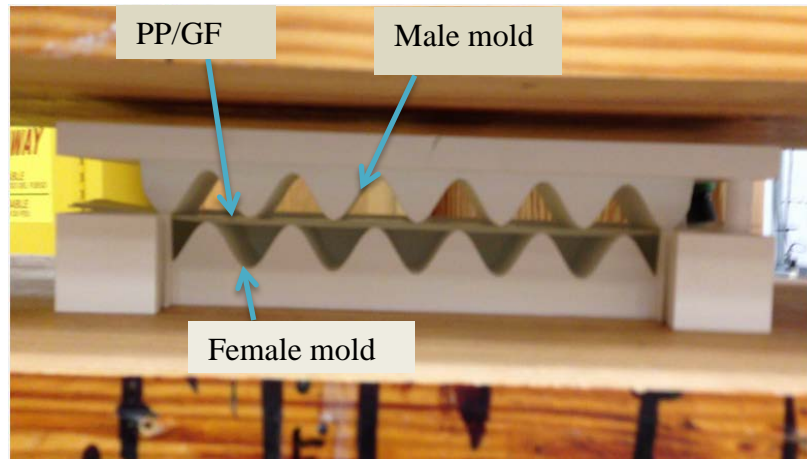


Figure 6.2: Typical setup for dry-run experiments.

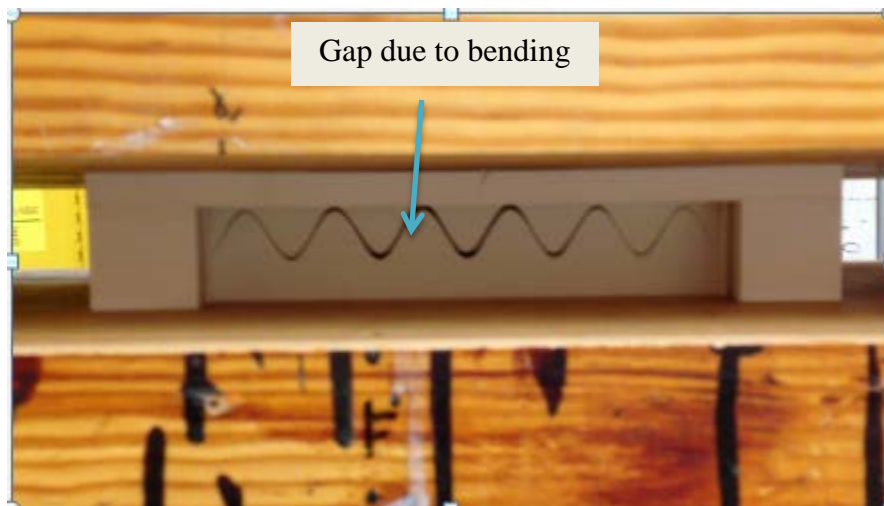


Figure 6.3: Bending at center during stamping of unheated prepreg tape stack.

Many other design features were added as a result of insight gained from these trial dry-runs.

The edge walls were converted to a parabolic section to avoid pinching of prepreg tapes. Release pin holes were added to enable removal of formed parts that stick to the female mold. A slot was made to fit a transparent polycarbonate sheet to allow viewing the deformation of the mold during thermoforming.

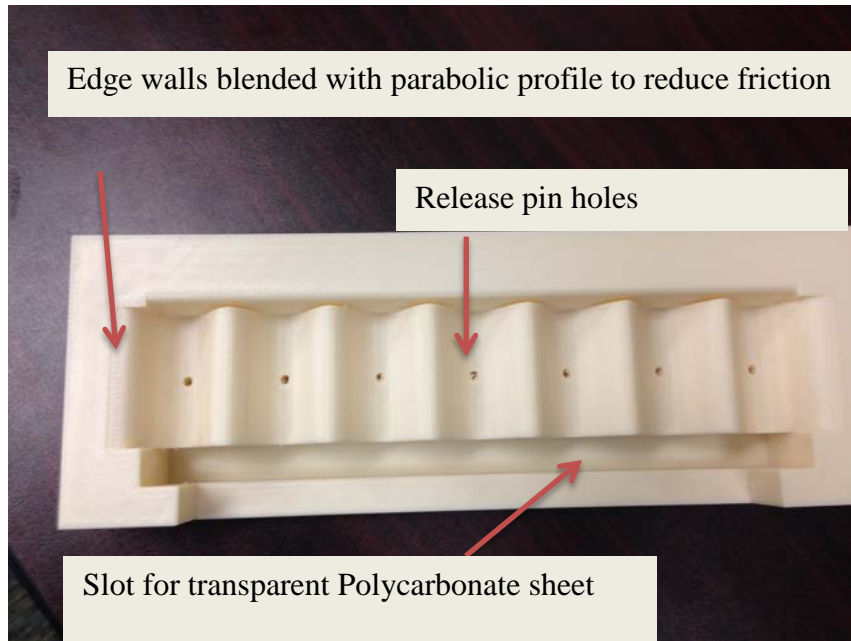


Figure 6.4: Female mold with design features.

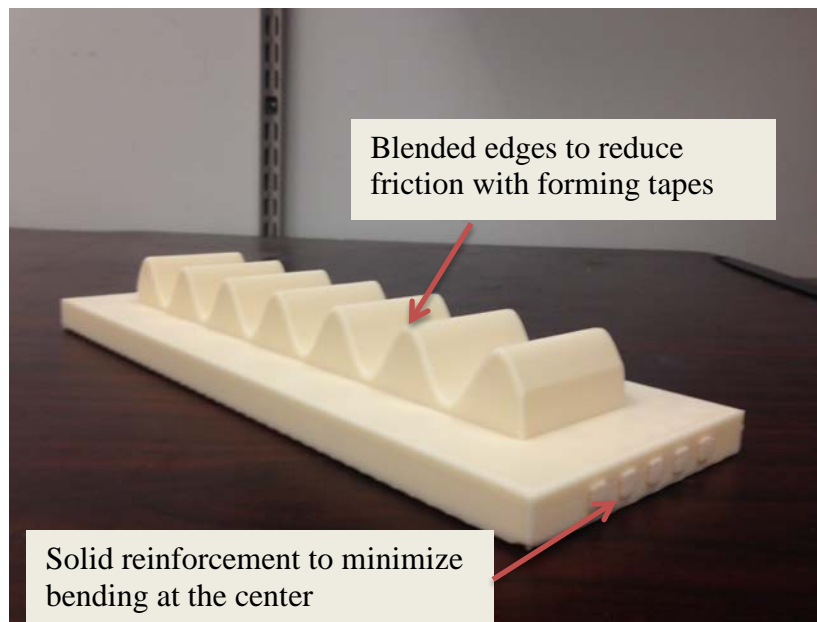


Figure 6.5: Male mold with design features.

However, a polycarbonate sheet was not used during the actual thermoforming experiments because the light reflected by the polycarbonate sheet interfered with the image taken by the ARAMIS cameras. This resulted in poor quality images being recorded for strain computation. Hence, the polycarbonate sheet was removed in the final experiment.

The edges of male mold were also blended to a circular profile to prevent any pinching with the sidewalls. Solid reinforcements were added through the male mold to reduce bending of the mold. As a result, the bending of the mold was reduced during the dry run experiments. Figure 6.2 shows a typical set-up for the dry run experiments. The amount of bending in Figure 6.3 can be compared with that in Figure 6.6 and the reduction in bending can be noticed. There gap at the center is still larger than that at the ends, but comparing the gaps at the center after modifications to the ones after the modifications, the gap was considerably smaller.



Figure 6.6: Bending reduced due to reinforcements in male mold.

6.2 FINITE ELEMENT MODEL

A finite element model was created using the internal structure of the material created in Chapter 5. The mold was modeled as an orthotropic solid with a skin of ULTEM 9085 material. The mechanical properties for the orthotropic solid were generated from the finite element model created in Chapter 5.

6.2.1 Determination of material properties for the orthotropic solid

Five finite element models were created to determine the material properties for the orthotropic solid. E_z , E_x , ν_{xy} , ν_{yz} , G_{xy} , G_{xz} , and G_{yz} were the engineering constants determined from the space frame model.

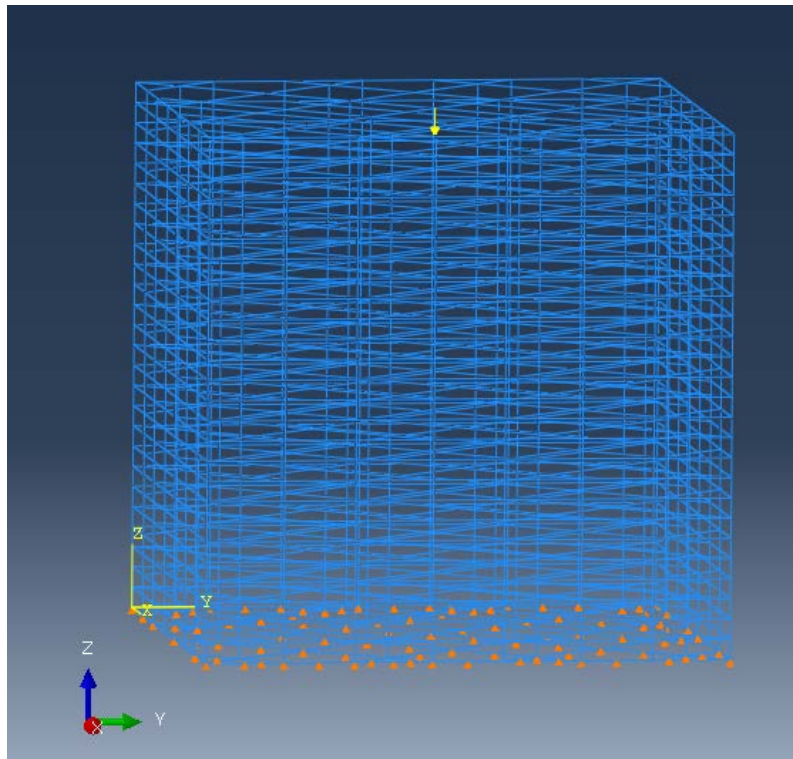


Figure 6.7: Finite element model to determine E_z and ν_{zy} .

Figure 6.7 shows the space frame model used to calculate E_z and v_{zy} . Unit loading was applied in the Z direction. The nodes at $Z = 0$ have the boundary condition of displacement in the Z direction equals zero. A node at $Z = 0$, $X = 6.5$ and $Y = 6.5$ had additional boundary condition of displacements in the X and Y direction that equal zero for the stability of the structure. Kinematic coupling of all the nodes at $Z = 13$ enforces equal displacement of these nodes in the Z direction. E_z was calculated using equation (13).

$$E_z = \frac{PL}{A_{xy} U_z} \quad (13)$$

where,

E_z	=	Elastic modulus in the Z direction	(MPa)
P	=	Loading	(N)
A_{xy}	=	Area of the model in XY plane	(mm ²)
U_z	=	Displacement in z direction	(mm)
L	=	Height of the model in Z direction	(mm)

For calculation of v_{zy} , ε_y and ε_z were calculated by taking an average of ratio of total displacement to original length in the Y and the Z direction respectively. The lines that corresponded to the nodes were considered. Average of such values was taken. The average of ε_y and ε_z were calculated. v_{zy} was calculated per equation (14).

$$v_{zy} = -\frac{\varepsilon_y}{\varepsilon_z} \quad (14)$$

Figure 6.8 shows the process adopted for calculation of Poisson’s ratio. Lateral deformation between two nodes, with equal X-coordinates but at the opposite faces with different Y-coordinate, was calculated. An average value for the deformation was calculated by taking such deformations at nodes on the face shown at different X-coordinates.

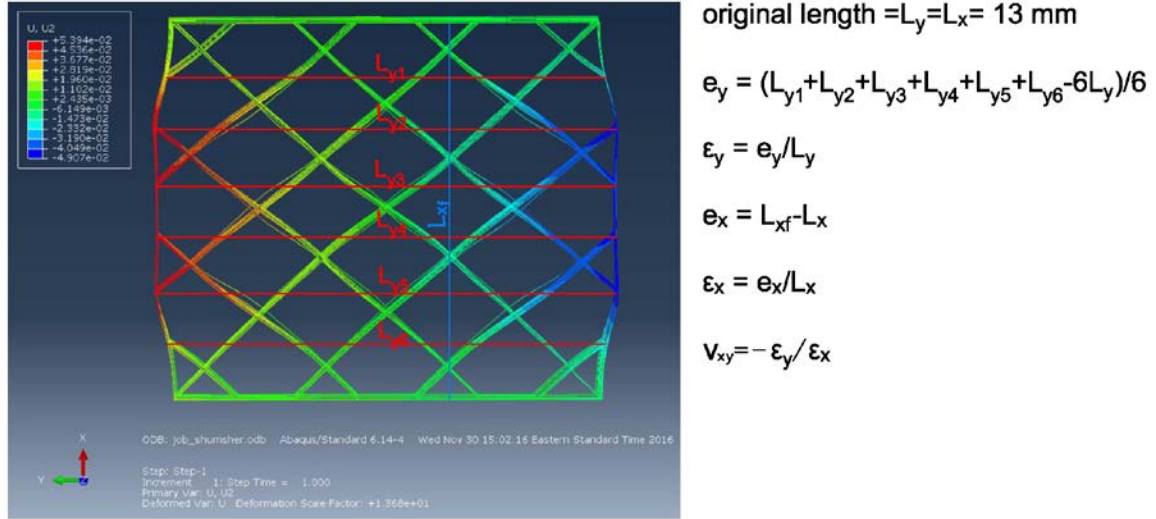


Figure 6.8: Calculation of poissions ratio of internal structure using the lattice structure finite element model for ν_{xy} .

Similarly, for the model to calculate E_x and ν_{xy} , unit loading was applied in the X direction. The nodes at $X=0$ have boundary condition of displacement in X direction equal zero. A single node in $X=0$ was given an additional boundary condition of $Y=0$ and $Z=0$ for stability of the model. A kinematic coupling with all nodes at $X = 13$ was used to enforce equal displacement in the X direction. E_z was calculated using equation (15).

$$E_x = \frac{PL}{A_{zy} U_x} \quad (15)$$

where,

E_x	=	Elastic modulus in the X direction	(MPa)
P	=	Loading	(N)
A_{zy}	=	Area of the model in the ZY plane	(mm ²)
U_x	=	Displacement in the X direction	(mm)
L	=	Height of the model in the X direction	(mm)

ν_{xy} , ε_y and ε_x were calculated. The average of ε_y and ε_x were calculated. ν_{xy} was calculated per equation (16).

$$\nu_{xy} = -\frac{\varepsilon_y}{\varepsilon_x} \quad (16)$$

Figure 6.9 shows the finite element model used for the calculation of G_{xy} . Unit loading was applied at the corner nodes at $X=13$, $Y= 13$, and $Z = 13$, and $X=13$, $Y = 13$, $Z = 0$. The loading was in the Y direction. All nodes at $X = 0$ were enforced a boundary condition of no displacement in the Y direction. One node at $X = 0$ was given an additional boundary condition of $Y = 0$ and $Z = 0$ for stability conditions. The nodes at $Z = 13$ were enforced with a kinematic coupling of equal displacement in the Y direction. Figure 6.9 shows the finite element model used for the calculation of G_{xy} . Unit loading was applied at the corner nodes at $X=13$, $Y= 13$, and $Z = 13$, and $X=13$, $Y = 13$, $Z = 0$. The loading was in the Y direction. All nodes at $X = 0$ were enforced a boundary condition of no displacement in the Y direction. One node at $X = 0$ was

given an additional boundary condition of $Y = 0$ and $Z = 0$ for stability conditions. The nodes at $Z = 13$ are enforced with a kinematic coupling of equal displacement in the Y direction.

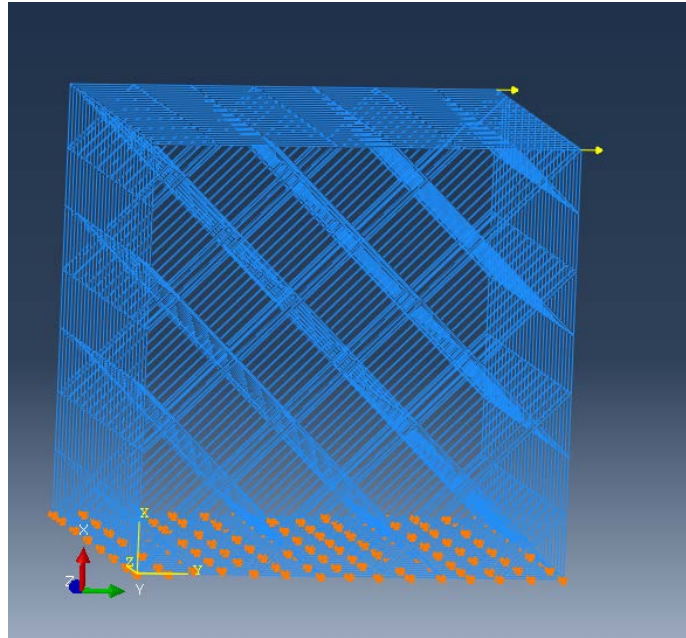


Figure 6.9: Finite element model for calculation of G_{xy} .

Shear modulus G_{xy} was calculated according to Equation (17).

$$G_{XY} = \frac{\tau_{XY}}{\gamma_{XY}} = \frac{2PL}{A_{ZY}x} \quad (17)$$

where,

- | | | | |
|----------|---|-----------------------------------|--------------------|
| G_{XY} | = | Shear modulus in XY plane | (MPa) |
| P | = | Loading | (N) |
| A_{XZ} | = | Area of the model in the XZ plane | (mm ²) |
| x | = | Displacement in the X direction | (mm) |

L	=	Height of the model in the Z direction	(mm)
γ_{XY}	=	Shear strain	(rad)
τ_{XY}	=	Shear stress	(MPa)

The model variables are shown clearly in Figure 6.10.

G_{yz} and G_{xz} were calculated similarly. The model used in calculation of G_{yz} and G_{xz} differed in loading, boundary condition, and the kinematic constraint applied. These loadings, boundary conditions, and the kinematic constraints are applied appropriately such that G_{yz} and G_{xz} can be calculated from the results.

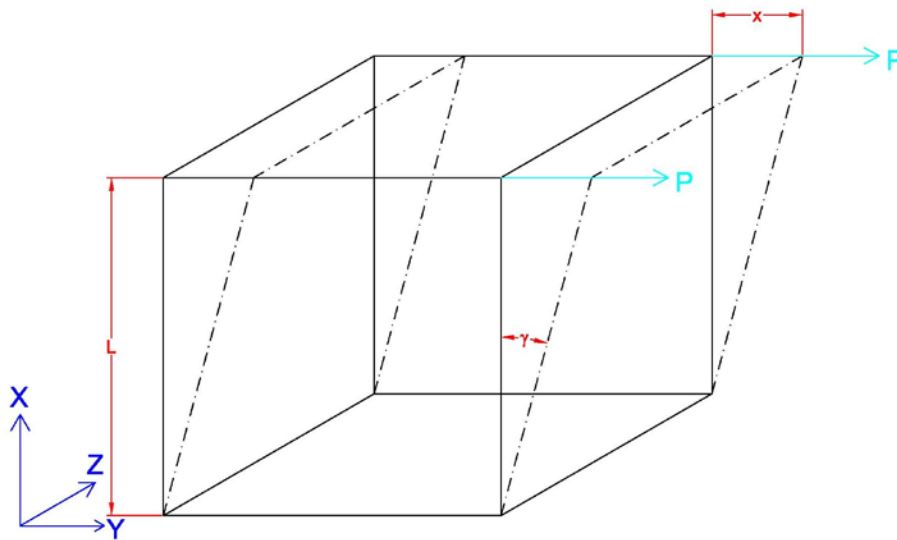


Figure 6.10: Figure showing variables for shear modulus calculation.

The values obtained for the properties are listed in Table 6.1.

Table 6.1: Table showing the mechanical properties of the orthotropic solid used to replace the internal cellular structure for the printing parameters used

Mechanical Property	Value
E_x	132 MPa
E_y	132 MPa
E_z	186 MPa
ν_{xy}	0.824
ν_{xz}	0
ν_{yz}	0
G_{xy}	5.27 MPa
G_{xz}	34.3 MPa
G_{yz}	34.3 MPa

6.2.2 Properties of the part skin

The material properties for the skin were same as the one for the ULTEM 9085 material. The material was isotropic with elastic modulus of 2860 MPa and Poisson's ratio of 0.285. The skin had a thickness of 1.02 mm.

6.2.3 Finite element model of the mold assembly

The finite element model for the matched mold system is shown in Figure 6.11.

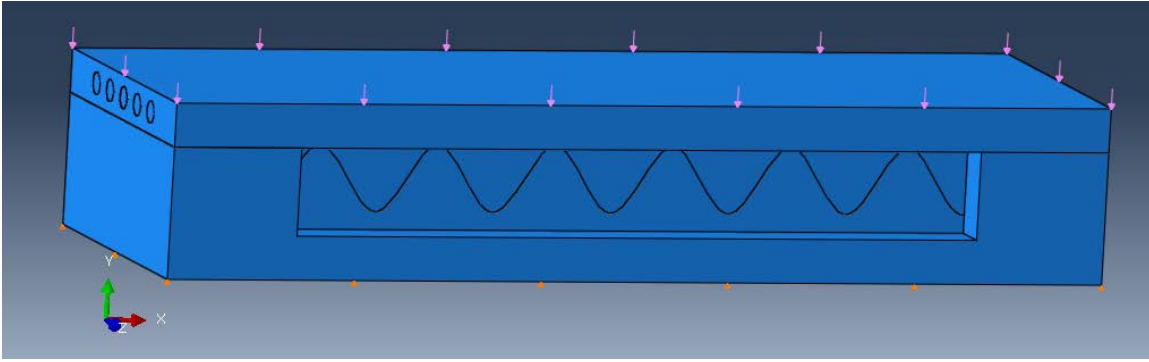


Figure 6.11: Finite Element Model of the mold assembly.

6.2.3.1 Parts

The finite element model consisted of three main parts, viz, the male mold, the female mold, and the reinforcement bars. The geometry for these models was created in Siemens NX CAD software and is exported to *iges* format. This model was imported in Abaqus. Material orientation was defined for the internal structure. An outer skin was applied to the male and female molds. The reinforcement bars were modelled as isotropic solids.

6.2.3.2 Assembly

The assembly consists of the male mold, the female mold and the five solid circular internal reinforcement sections. A uniform load of 3.5 MPa was applied on top of the male mold. The bottom of the female mold allowed no movement in the Y direction as a boundary condition. One node at the bottom of the female mold was restrained against movement in the X and Z direction for stability. The nodes at the interface were merged for all the components.

6.2.3.3 Meshing

Ten-noded quadratic tetrahedral elements were used for meshing with elements having maximum edge length of 4 millimeters.

6.2.3.4 Model Constraints

Three model constraints were defined for the assembly. The first one is a tie constraint with shared nodes between the solid reinforcement and the cellular structure in the male mold.

Another tie constraint was defined at the interface of male mold and female mold. A kinematic coupling with equal displacement in the Y direction was defined for the top surface of the male mold to enforce the equal displacement created by the movement of the press.

6.2.3.5 Results

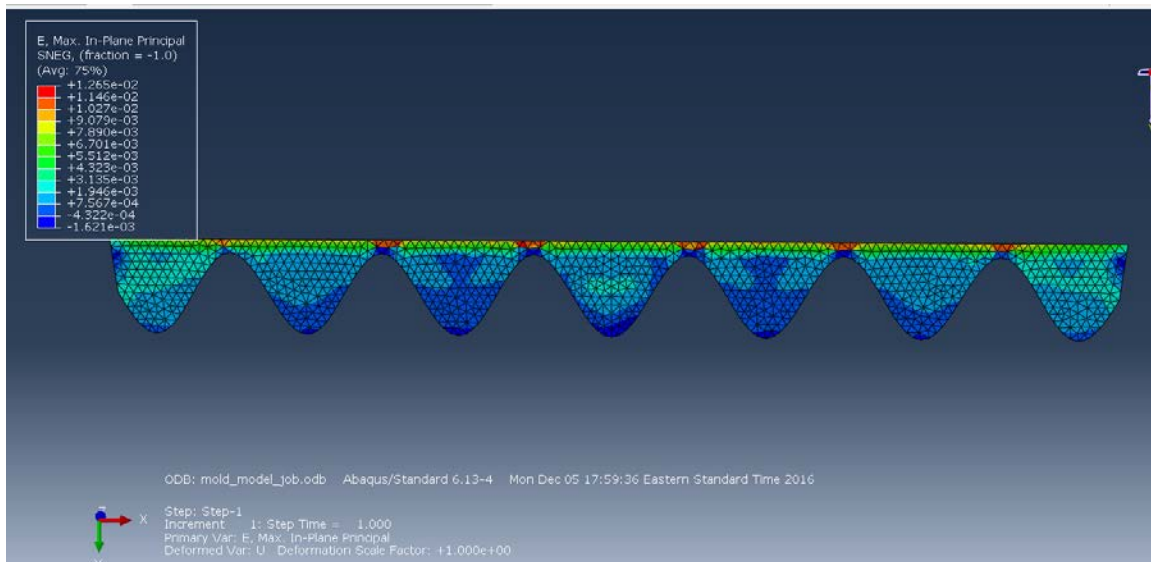


Figure 6.12: Major in-plane strain for sinusoidal part of the male mold.

Figure 6.12 shows the displacement computed using the finite element model. The maximum displacement observed was at the tip of the mold. The displacements gradually decrease and are zero at the top. Figure 6.13 shows the strains on the molds in the Y direction. The maximum strains observed were at the tips of the sine wave at the tips of the mold where the deformations are also highest. The strains were lowered when moving away from the tips. The strains in the sine wave curve where the parts are formed are still in the linear elastic range when compared with values from Figure 3.16. This ensures that the model is still valid since the material is in the linear elastic region.

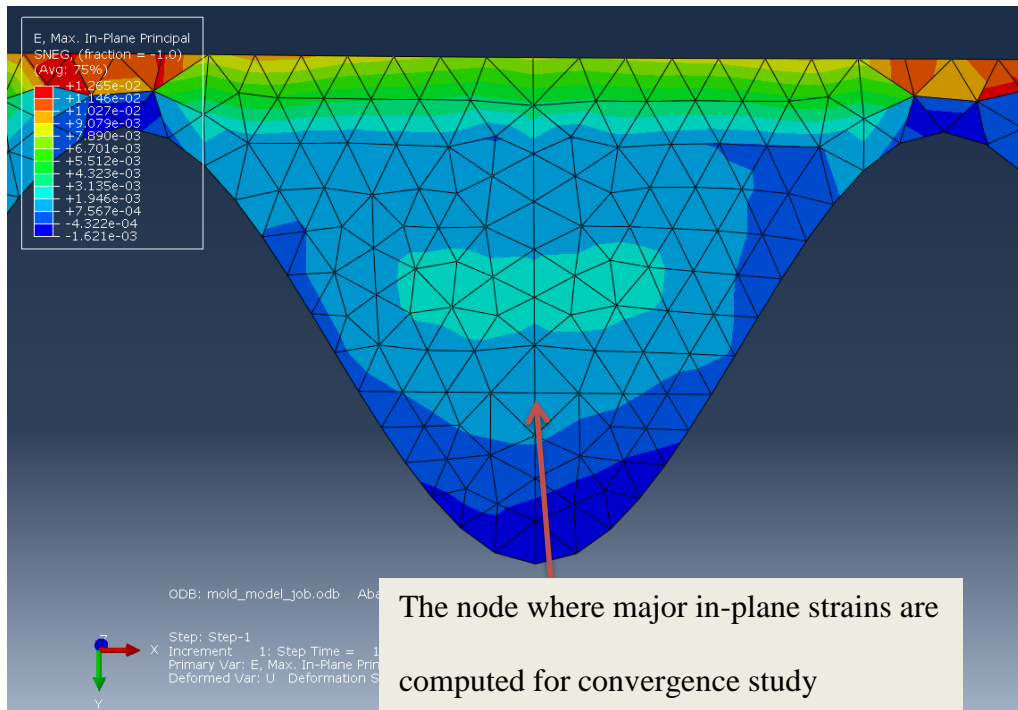


Figure 6.13: Strain of the finite element model in the Y direction.

A single node, as mentioned in Figure 6.13, of the central protrusion of the male mold was studied for major in-plane strains in models with four different sizes of the edge of element. The

values for the maximum size of the edge of element were taken as 10 mm, 8 mm, 6 mm, 4 mm, 3 mm, and 2 mm. Figure 6.14 shows the convergence of the model with decreasing the mesh size. The model converges smoothly with decreasing mesh size. The value for major in-plane strain at the node was found to be 1.413×10^{-3} mm/mm for the mesh with maximum size of edge of the element of 2 mm.

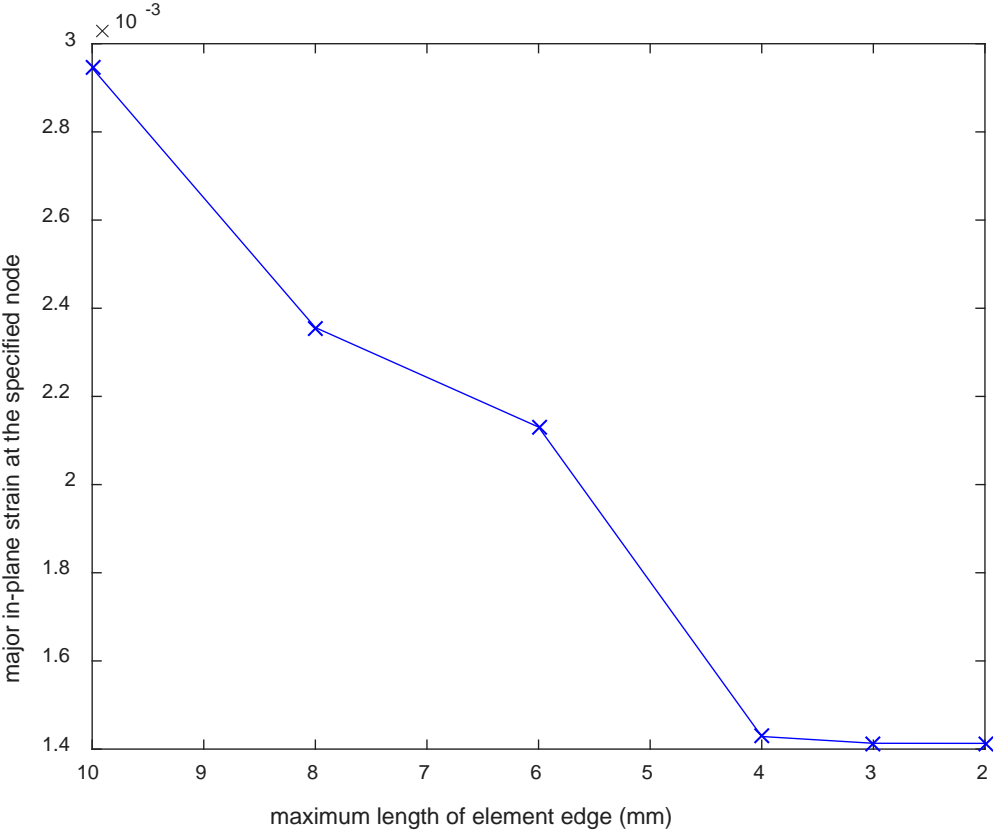


Figure 6.14: Convergence plot the finite element model of the mold.

6.2.4 Experimental verification of the strains

Testing was carried out for the experimental verification of the strains in the mold. Figure 6.15 shows the experimental setup used for the experimental verification of the finite element model used in Section 6.2.3.

6.2.4.1 The verification process

The mold was placed in the platen so that it would be aligned properly. The position of the mold was secured by using a narrow double-sided tape. The mold was sprayed with Dupont Teflon penetrating lubricant as a mold release agent. The front face of the mold was painted with a stochastic pattern of black and white speckles. ARAMIS DIC system was set up by focusing the cameras on the black and white speckles and carrying out the calibration procedure.



Figure 6.15: Setup for experimental verification of the finite element model.

PP/GF unidirectional tapes were used for the thermoforming process. The tapes used were TENCATE CETEX TC960 PP/GF tapes. The resin content by weight was marked as 40% by the manufacturer. The composite density was provided by the manufacturer as 1.49 g/cm^3 . The tape had a width of 164 mm (6.5 inches) and a thickness of 0.27 mm (0.011 inches). Five different stacks of prepreg tapes were made with following stacking sequences:

- a. [+45/-45]
- b. [+45/-45]₂
- c. [+45/-45]₃
- d. [+45/-45]₄
- e. [+45/-45]₅

The tapes were cut to size using a pair of scissors so that they fit entirely within the mold. These stacks were heated in the heating platen. A layer of parchment paper was used to separate the tape stacks from the heating platen. This made it easier to quickly pick up the tape stack and place it on the mold. Silicone rubber foam was used as an insulator. The probe for the digital thermometer was placed above the topmost tape and below the silicone rubber foam. The stacks were heated until a temperature of $160 \text{ }^\circ\text{C}$ was attained. The tapes were quickly removed from the platen and put on the press. The press was set to apply a maximum pressure of 3.45 MPa (500 psi) on the mold. The tape stack was pressed and the pressure was held for 2 minutes. Images were taken at the rate of two images per second using the ARAMIS DIC system so that strains could be computed. The press was opened after two minutes and the formed part was

removed. The part formation for a six-layer tape stack after removing pressure is shown in Figure 6.16.

The thickness of the part made a difference in how the parts were formed. The part with only two layers did not form properly. The clearance between the male mold and the female mold was higher than the combined thickness of the two layers. As a result, complete transfer of pressure to the part did not occur. There is also observable lowering in the width of the part with smaller thickness. This effect is reduced and almost negligible in part with ten layers of tape. Figure 6.17 shows the parts formed during the thermoforming experiments.



Figure 6.16: The formed part stuck to the male mold after pulling the mold to the top.



Figure 6.17: Parts formed with increasing thickness from right to left.

6.2.5 Comparison of results experiments and the finite element model

The strains computed from the finite element model are compared with the strains from the experiment. From Figure 6.18 and Figure 6.20, it is observed that the strains are comparable. The negative strains are highest at the tip of the mold for both finite element model and the experimental results. The positive strains are present towards the center of the mold. The maximum strains are at the regions shown in Figure 6.20.

The experimental strains deviate from the strains from the FE model in that there is a region where positive strains peak on the left side. Also, the maximum negative strains recorded in the experiment are lower than that in the finite element model. The strains at the tip of the mold could not be captured effectively during forming because parts of the tape came out and interfered with the field of vision of the DIC cameras.

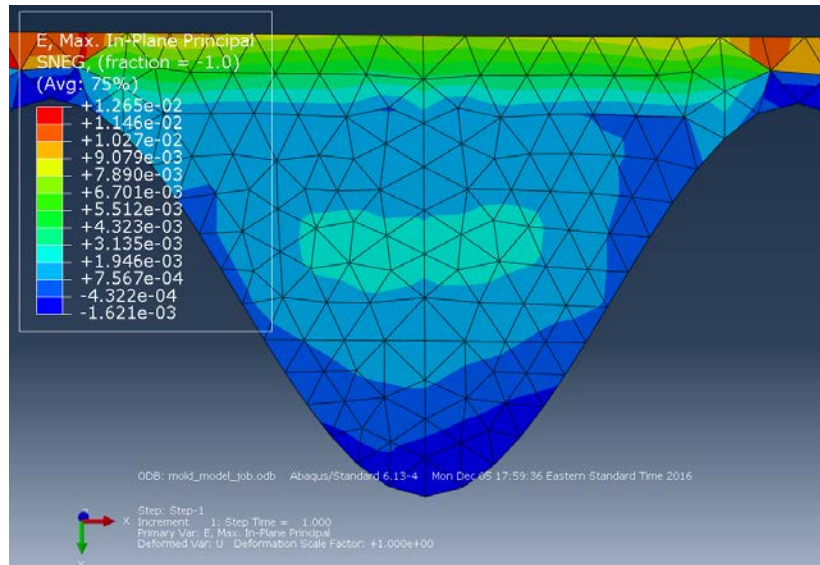


Figure 6.18: Max In-Plane Principal Strains on the central part of the mold.

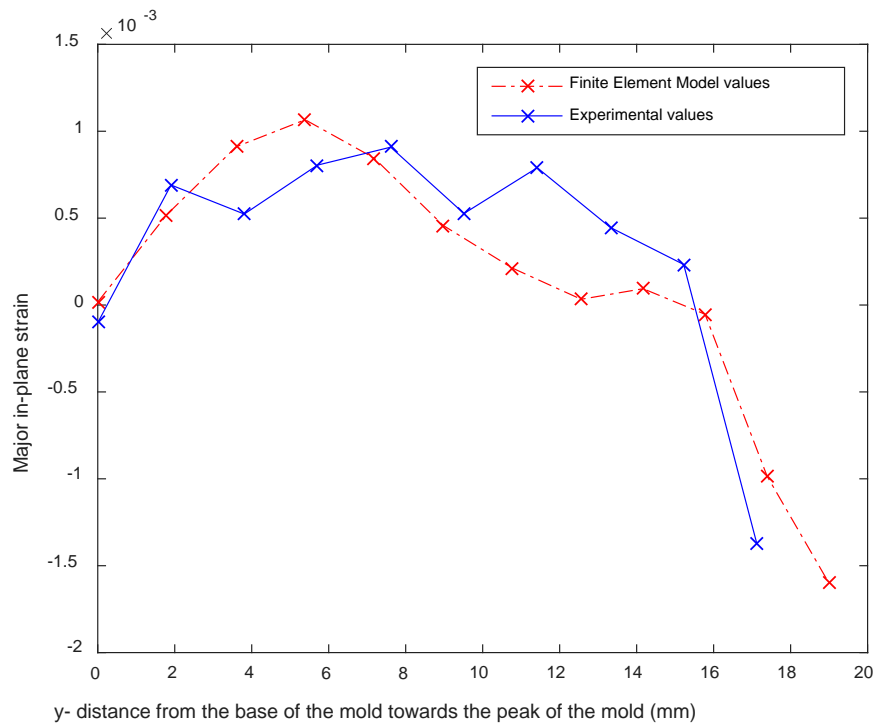


Figure 6.19: Comparison of the Major in-plane strain from the FE model to those observed experimentally.

Figure 6.19 shows the comparison of the major in-plane strain along the section shown in Figure 6.20. The experimental values were taken from the first stage after the pressure is applied for the 8-layer layup of tapes. The strain at the tip of the mold could not be determined because the layup interfered with the tip. There are many reasons for the deviation of the values obtained from the finite element model to the values obtained from the experiment. The model does not incorporate the stiffness of the part to be formed. The model also does not take into the account the effects of heating of the ply.

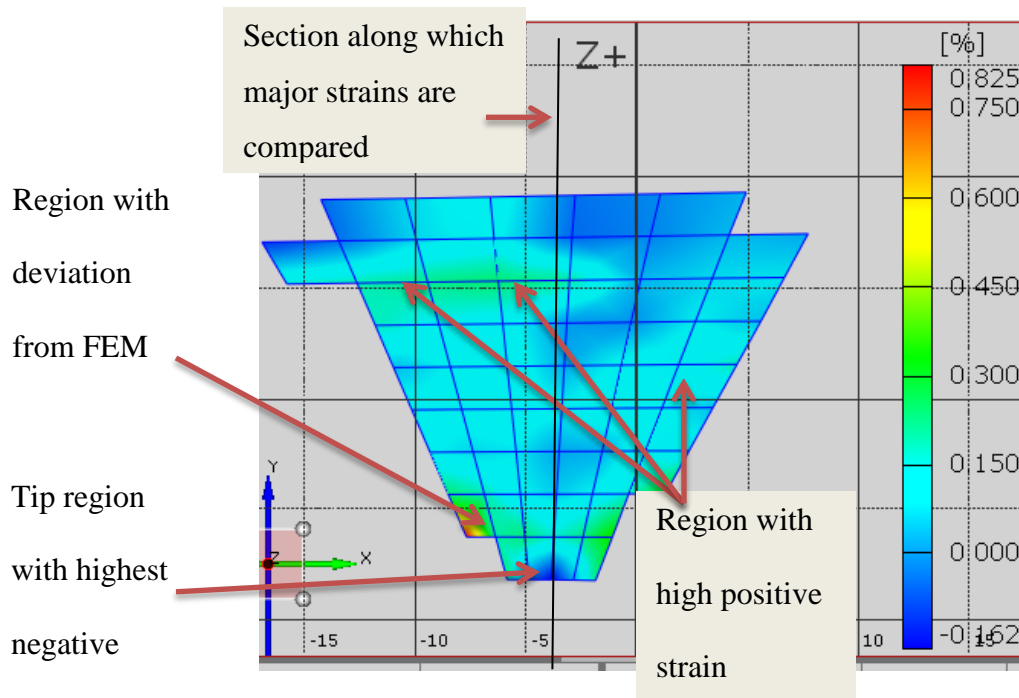


Figure 6.20: Maximum In-Plane Principal Strains on the central part of the mold from experiments.

6.3 CONCLUSIONS AND RECOMMENDATIONS

1. 3D printing can be used for iterative mold design to determine the problems that might arise during thermoforming and to help refine design and manufacture of molds. The speed of 3D printing for prototyping helps to carry out the iterative process more rapidly than it would have been using conventional subtractive manufacturing techniques.
2. A finite element model can be used to predict the strains in the mold while thermoforming, during the initial stages of forming when the mold just encounters the prepreg tapes. The constraint here is that the strains are within the linear elastic response of the material. With time and heating of the mold, however, the strains change as the elastic modulus and other engineering properties change with increase in temperature of the material. A model that takes the change in properties of the material with increase in temperature is needed to predict the mold deformations at the end of forming cycle.

CHAPTER 7

CONCLUSIONS AND RECOMMENDATIONS

7.1 MATERIAL SELECTION FOR 3D PRINTED MOLD

Material selection for 3D printed mold was discussed in Chapter 2. The mold material depends upon the part material being thermoformed. The melting temperature of the part material and the pressures that need to be maintained during thermoforming limit the range of materials that can be used as mold material. The temperature experienced by the mold needs to be lower than the glass transition temperature of the mold material. In addition, at the temperature experienced by the mold, the material should have an elastic modulus at the operational temperature that would prevent excessive deformation of the mold. Preliminary tests can be carried out to determine these forming temperatures and pressures. For polypropylene reinforced with glass fibers used for this study, a forming pressure of 3.45 MPa and a forming temperature of 130 °C was necessary. The forming temperature can be used to determine the suitability of a thermoplastic as a mold material using the suggested approach developed in Chapter 2.

7.2 MECHANICAL PROPERTIES OF 3D PRINTED LATTICE STRUCTURE

The printing time and material usage can be reduced by using the lattice internal structure. The mechanical properties of the 3D printed specimen can be altered by the use of cellular internal structure. The general idea is that more hollow the inside of the material is, the weaker the part is. The cellular internal structure is associated with considerably high variability in elastic modulus compared to the solid (completely filled) internal structure. The strength values, however, are consistent from sample to sample. The variability in elastic modulus was found to be affected by two parameters, namely, height of the specimen and the base area of the

specimen. Because of the high variability observed, a high factor of safety needs to be considered when designing molds.

The creep tests carried out showed that at low stress levels and short times of sustained pressure for thermoforming, creep deformations are small. Their effects on the thermoforming process can thus be neglected, at least for the material used ULTEM 9085, the specified internal lattice structure, and the specified thermoforming process parameters.

The effect of temperature on the storage modulus of the material was found to be significant, which is expected for thermoplastic polymers. This should be considered during the design of the mold. For ULTEM 9085, the storage modulus was almost halved at 150 °C compared to that at the room temperature. As a result, the internal cellular structure could be made denser so that the storage modulus at room temperature is twice the required value so that at forming temperature, the required storage modulus value is maintained.

7.3 FINITE ELEMENT MODELING FOR INTERNAL STRUCTURE

A fairly accurate and computationally economical finite element model was developed using 3D space frames and plates to represent the internal structure of the 3D printed material. This model can be used to determine the printing parameters that would result in the required elastic modulus of the material. As a result, several rounds of testing can be avoided and the overall mold design process can be sped up.

7.4 SUGGESTED MOLD DESIGN PROCESS

The suggested mold design process is in the flowchart from Figure 7.1 and Figure 7.2

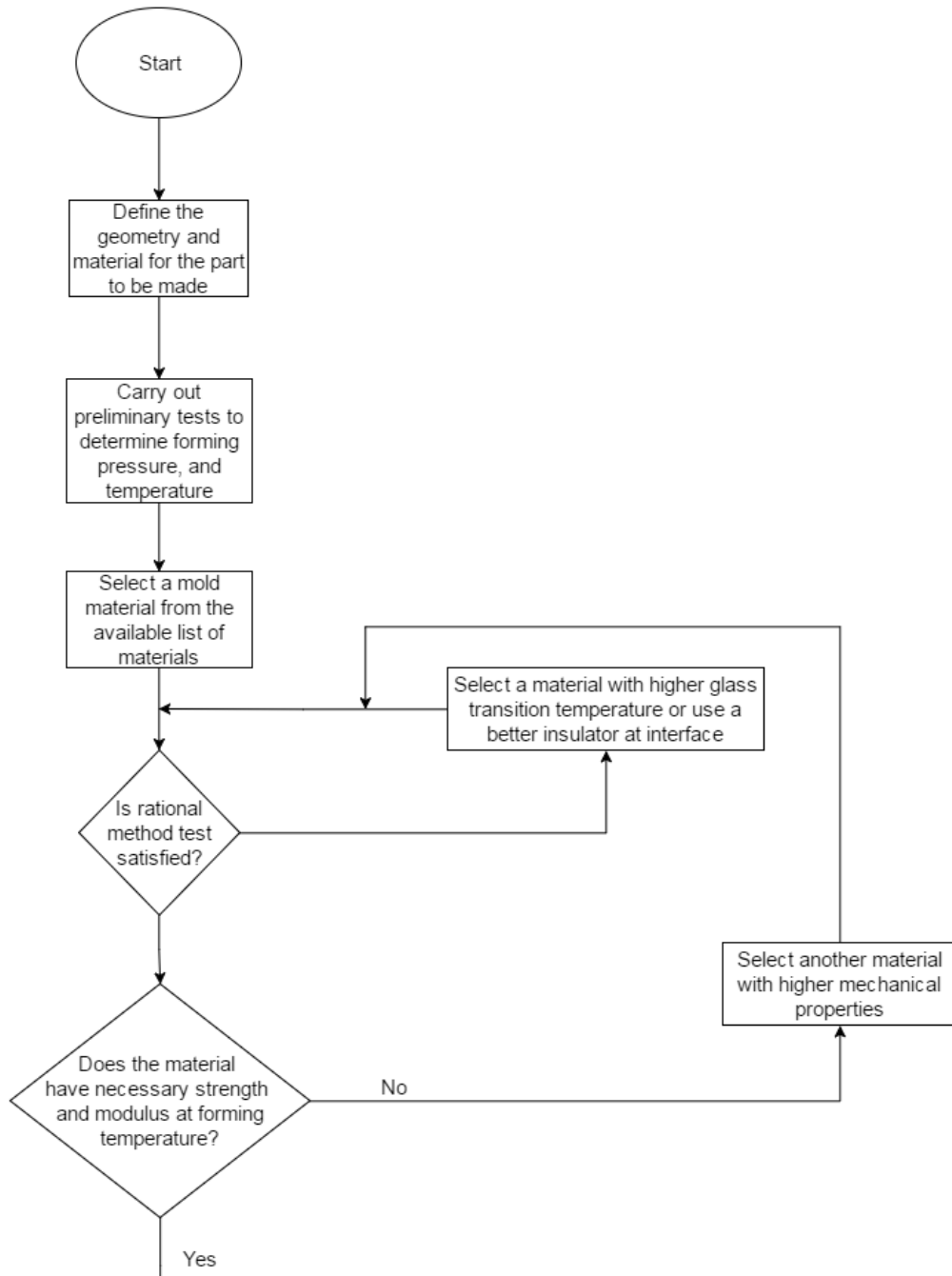


Figure 7.1: Flowchart describing the mold design process - part 1.

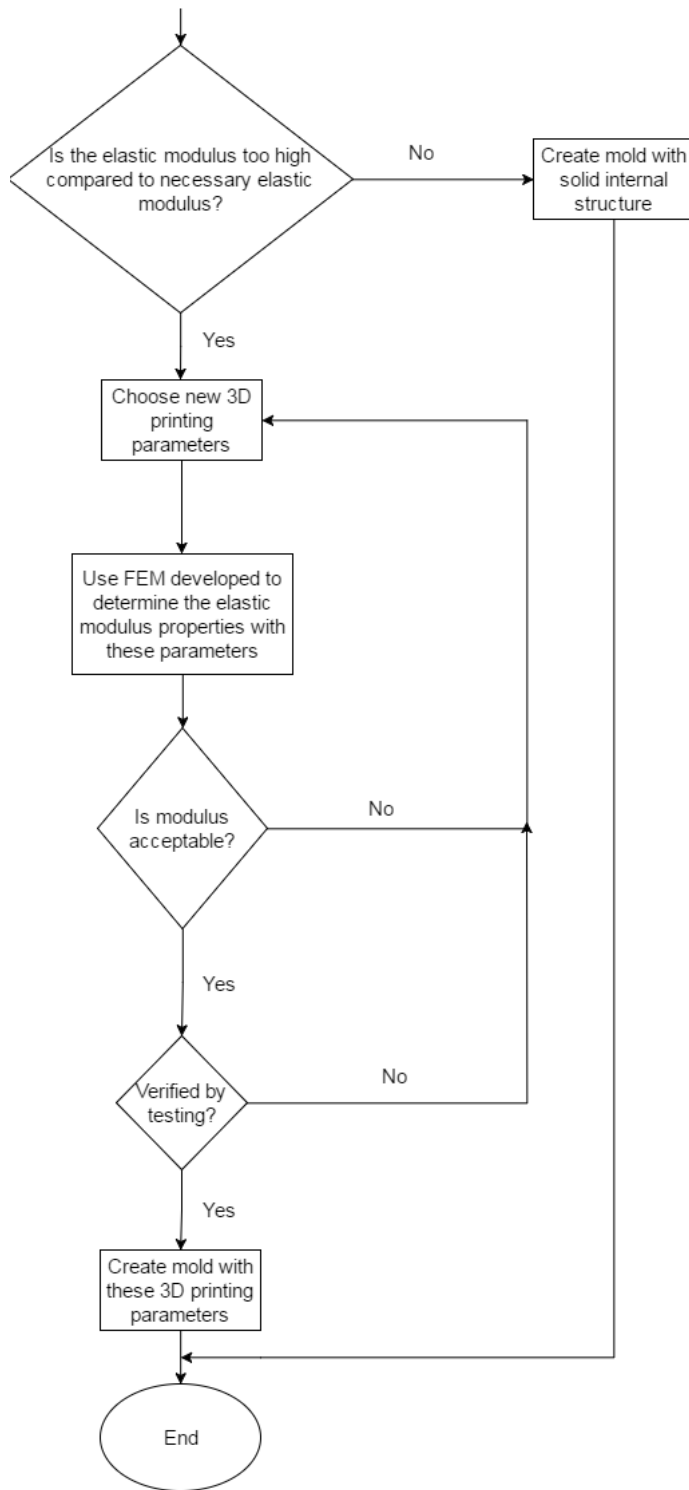


Figure 7.2: Flowchart describing the mold design process - part 2.

7.5 EXAMPLE OF MOLD DESIGN OPTIMIZATION PROCESS

The internal structure of the mold can be optimized for the stamp forming process using the developed finite element model. An example is explained below. Considering a male mold for rubber stamp forming of the web of a sine wave web beam, where the maximum deformations need to be limited to 1.5mm. The optimization problem is stated as the minimization of objective function defined by Equation (18).

$$f(x) = \text{abs}(\max(u(x)) - 1.5\text{mm}) \quad (18)$$

Where, u = magnitude of displacement

the domain is the bounding volume of the mold

x is the air gap between the beam elements in the lattice

A finite element model is made whereby the internal cellular structure is represented as a anisotropic solid. The outer shell was applied as a skin to the solid. Uniform pressure was applied on the surface in contact with the part. Boundary conditions are set to be zero displacement in the Y-direction for the top of male mold. The model was run and the displacements are found to be excessive as shown in Figure 7.3.

A new finite element model for the internal structure was created with reduced air gap. The air gap was reduced from 2.0mm edge to edge to 1 mm edge to edge. Virtual experiments were run on this model to determine the material properties to use for the anisotropic solid.

The properties of the new equivalent anisotropic solid are shown in Table 7.1.

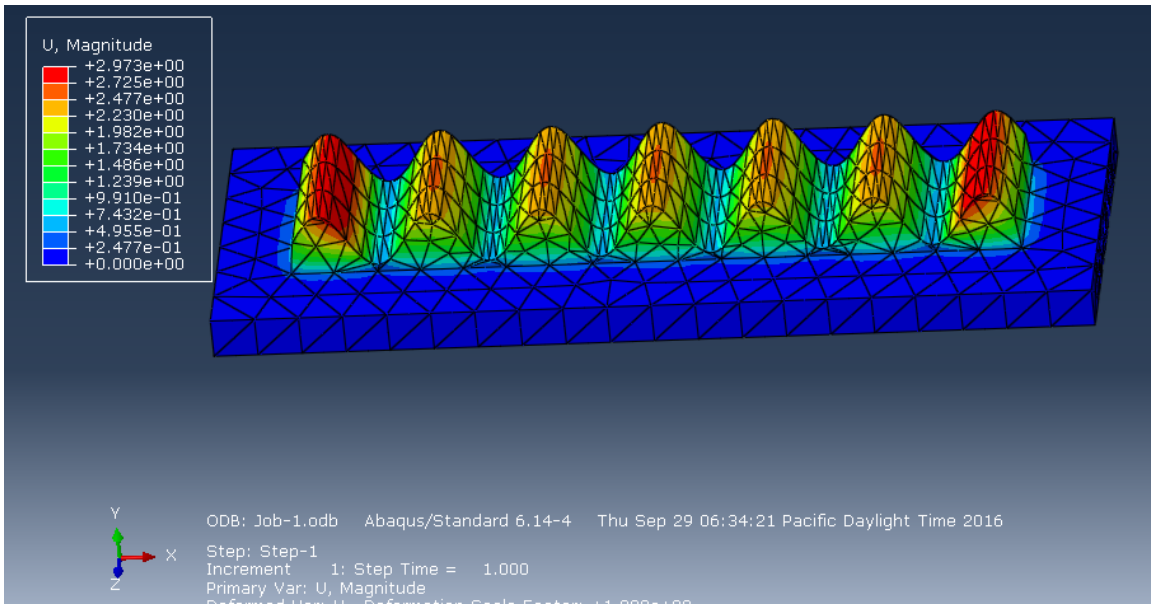


Figure 7.3: Deformations predicted in rubber stamp forming of the mold.

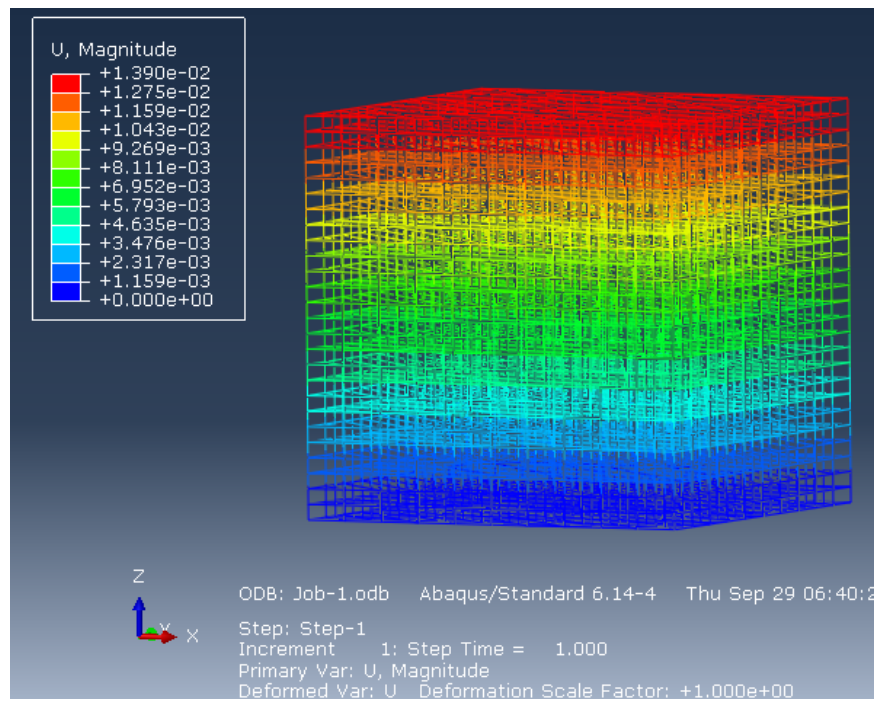


Figure 7.4: Finite Element model E_z and v_{zx} for internal structure with reduced air gap.

Table 7.1: Properties of the equivalent anisotropic solid when air gap is changed from 2.0 mm to 1.0 mm.

Property	Value
E_x	518 MPa
E_y	518 MPa
E_z	935 MPa
ν_{xy}	0.851
ν_{xz}	0
ν_{yz}	0
G_{xy}	66.5 MPa
G_{xz}	18.4 MPa
G_{yz}	66.5 MPa

These values were applied to the anisotropic solid in the previous model and the model is run again. The deformation values are checked and they were found to be within required limits, i.e. the magnitude of maximum deformation was less than 1.5 mm, as shown in Figure 7.5. If the maximum magnitude of the deformation was more than 1.5 mm, a new iteration would have been carried out with a reduced value for air gap.

7.6 RECOMMENDATIONS FOR FUTURE WORK

7.6.1 Study of factors affecting the variability in 3D printing of parts with lattice internal structure

Significant variability was observed in the parts created by 3D printing when the parts had lattice internal structure. This variability was attributed to the misalignment of the deposited filament. The height of the part and the base area of the part seemed to have significant effect in the COV of the parts created. Other factors that affect the variability, and ways to reduce this variability in parts produced by 3D printing need to be further researched.

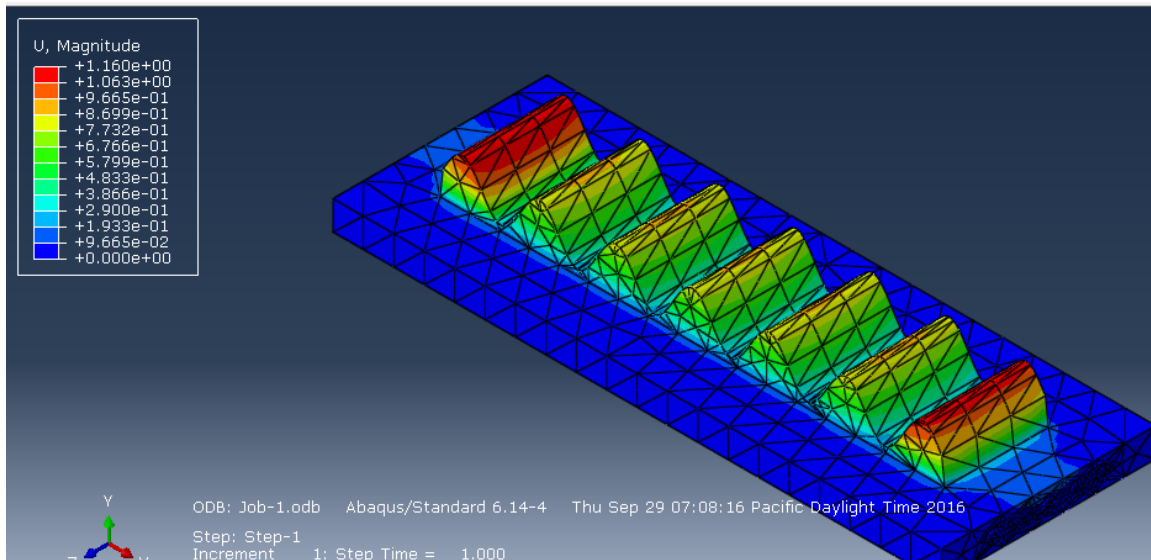


Figure 7.5: Deformations predicted with the new internal structure.

7.6.2 Creating a more versatile Finite Element Model

A more versatile finite element model that can predict the non-linear behavior of the lattice internal structure needs to be investigated. Gibson and Ashby [50] have an analytical model to predict this behavior for cellular solids. However, a finite element model would be more useful for thermoforming simulations. This model would be useful to make the strength predictions for the parts with lattice internal structure. It is also necessary to keep the computational costs low while extending the current model, to obtain useful results in short time.

7.6.3 Automation of the mold optimization process

The mold optimization process described in Section 7.5 can be automated so that optimum values for the printing parameters of internal structures could be determined. Such automation routine would consist of two optimization steps. The first step would be to determine the material properties of the equivalent anisotropic material that would satisfy the design criteria of deformation. The second optimization step would give the printing parameters that result in the internal structure with material properties calculated from the first optimization step.

7.7 FINAL CONCLUSIONS

The following conclusions have been arrived to from the study carried out during thesis work:

1. An equation has been developed based on the thermal properties of the 3D printed mold polymer and the thermal properties of the part polymer to decide whether the 3D printed mold polymer could be used for thermoforming the part polymer.
2. A finite element model consisting of space frame and shell has been developed to predict the elastic properties of a 3D printed mold with lattice internal structure. This model has been

verified through material characterization experiments. This finite element model also has been used in virtual experiments to determine the mechanical properties of an orthotropic solid representing the 3D printed material in another computationally inexpensive finite element model.

3. It was verified that the properties of an extruded filament can be used for the material properties in the finite element model when considering 3D printed parts made from amorphous polymers.
4. For structures with lattice internal structure the interactions in the planes of deposition can be neglected because the region where interaction occurs is very small compared to the overall area in the lattice region.
5. This finite element model can be used to optimize the internal structure of the mold to get the required mechanical properties of the mold. This optimization can be utilized, not just in mold making, but also in other applications of 3D printing. As 3D printing becomes faster and gets used more widely, this optimization technique will be available in designing parts.

REFERENCES

- [1] Long AC. Composites forming technologies: Elsevier; 2014.
- [2] Friedrich K, Hou M. On stamp forming of curved and flexible geometry components from continuous glass fiber/polypropylene composites. *Composites Part A: Applied Science and Manufacturing*. 1998;29(3):217-26.
- [3] Fallböhmer P, Rodríguez C, Özel T, Altan T. High-speed machining of cast iron and alloy steels for die and mold manufacturing. *Journal of Materials Processing Technology*. 2000;98(1):104-15.
- [4] Altan T, Lilly B, Kruth J-P, König W, Tönshoff H, Van Luttervelt C, et al. Advanced techniques for die and mold manufacturing. *CIRP Annals-Manufacturing Technology*. 1993;42(2):707-16.
- [5] Hu W, Poli C. To Injection Mold, to Stamp, or to Assemble? A DFM Cost Perspective. *Journal of Mechanical Design*. 1999;121(4):461.
- [6] Pham D, Gault R. A comparison of rapid prototyping technologies. *International Journal of machine tools and manufacture*. 1998;38(10):1257-87.
- [7] Sachs E, Wylonis E, Allen S, Cima M, Guo H. Production of injection molding tooling with conformal cooling channels using the three dimensional printing process. *Polymer Engineering & Science*. 2000;40(5):1232-47.
- [8] Zonder L, Sella N. Precision Prototyping, The role of 3D printed molds in the injection molding industry. White Paper by Stratays Inc. 2013.
- [9] Milberg E. ONRL, Boeing Complete First Successful Autoclave Testing of Fully 3D-Printed Tools. *Composites Manufacturing*, 2016.
- [10] Wendel B, Rietzel D, Kühnlein F, Feulner R, Hülder G, Schmachtenberg E. Additive Processing of Polymers. *Macromolecular Materials and Engineering*. 2008;293(10):799-809.
- [11] Ladd C, So JH, Muth J, Dickey MD. 3D printing of free standing liquid metal microstructures. *Adv Mater*. 2013;25(36):5081-5.
- [12] Hod Lipson MK. *Fabricated: the New World of 3d Printing*: Wiley; 2013.
- [13] Kenney ME. Cost Reduction through the Use of Additive Manufacturing (3D Printing) and Collaborative Product Lifecycle Management Technologies to Enhance the Navy's Maintenance Programs. DTIC Document; 2013.
- [14] Appleton RW. *Additive Manufacturing Overview For The United States Marine Corps*. RWAppleton & Company, Inc. 2014.

- [15] ISO/ASTM. Additive Manufacturing - General principles - Terminology. Processes Categories: ISO; 2015.
- [16] Gibson I, Rosen DW, Stucker B. Additive manufacturing technologies: Springer; 2010.
- [17] Kruth J-P, Leu M-C, Nakagawa T. Progress in additive manufacturing and rapid prototyping. *CIRP Annals-Manufacturing Technology*. 1998;47(2):525-40.
- [18] Pearce JM, Blair CM, Laciak KJ, Andrews R, Nosrat A, Zelenika-Zovko I. 3-D printing of open source appropriate technologies for self-directed sustainable development. *Journal of Sustainable Development*. 2010;3(4):17.
- [19] Pearce JM. Building research equipment with free, open-source hardware. *Science*. 2012;337(6100):1303-4.
- [20] Yousefpour A, Hojjati M, Immarigeon J-P. Fusion bonding/welding of thermoplastic composites. *Journal of Thermoplastic Composite Materials*. 2004;17(4):303-41.
- [21] Biron M. Thermoplastics and thermoplastic composites: William Andrew; 2012.
- [22] Chang I, Lees J. Recent development in thermoplastic composites: a review of matrix systems and processing methods. *Journal of thermoplastic composite materials*. 1988;1(3):277-96.
- [23] Allen KA. *Processing of Thermoplastic Composites, Polymer and Composites Processing*, 2012.
- [24] Kazmi S, Das R, Jayaraman K. Sheet forming of flax reinforced polypropylene composites using vacuum assisted oven consolidation (VAOC). *Journal of Materials Processing Technology*. 2014;214(11):2375-86.
- [25] Harkin-Jones E, Macauley NJ, Murphy WR. Thermoforming of polypropylene. In: Karger-Kocsis J, editor. *Polypropylene: An A-Z reference*. Dordrecht: Springer Netherlands; 1999. p. 847-52.
- [26] Hwang S-F, Hwang K-J. Stamp forming of locally heated thermoplastic composites. *Composites Part A: Applied Science and Manufacturing*. 2002;33(5):669-76.
- [27] Rowe J. *Advanced materials in automotive engineering*: Elsevier; 2012.
- [28] Van Rijswijk K, Joncas S, Bersee H, Bergsma OK, Beukers A. Sustainable vacuum-infused thermoplastic composites for MW-size wind turbine blades—preliminary design and manufacturing issues. *Journal of solar energy engineering*. 2005;127(4):570-80.
- [29] Van Rijswijk K, Bersee H. Reactive processing of textile fiber-reinforced thermoplastic composites—An overview. *Composites Part A: Applied Science and Manufacturing*. 2007;38(3):666-81.

- [30] Durai Prabhakaran RT. Are Reactive Thermoplastic Polymers Suitable for Future Wind Turbine Composite Materials Blades? *Mechanics of Advanced Materials and Structures*. 2013;21(3):213-21.
- [31] Lorriot T, El Yagoubi J, Fourel J, Tison F. Non-conventional Glass fiber NCF composites with thermoset and thermoplastic matrices.
- [32] Fossati D, Aronica A. Effects of resin and processing on mechanical properties of carbon fiber composites. 2015.
- [33] Bhudolia SK, Perrotey P, Joshi SC. Experimental investigation on suitability of carbon fibre thin plies for racquets. *Proceedings of the Institution of Mechanical Engineers, Part P: Journal of Sports Engineering and Technology*. 2015:1754337115598489.
- [34] (AMO) DsAMO. Additive Manufacturing: Pursuing the Promise.
- [35] The printed world. *The Economist*, 2011.
- [36] Petrovic V, Vicente Haro Gonzalez J, Jorda Ferrando O, Delgado Gordillo J, Ramon Blasco Puchades J, Portoles Grinan L. Additive layered manufacturing: sectors of industrial application shown through case studies. *International Journal of Production Research*. 2011;49(4):1061-79.
- [37] Nimbalkar S, Cox D, Visconti K, Cresko J. Life cycle energy assessment methodology and additive manufacturing energy impacts assessment tool. *LCA XIV International Conference*. San Francisco, CA2014. p. 130-41.
- [38] Ferreira J, Mateus A. Studies of rapid soft tooling with conformal cooling channels for plastic injection moulding. *Journal of Materials Processing Technology*. 2003;142(2):508-16.
- [39] *PlasticsNews*. Current Resin Pricing - Thermosets. 2015.
- [40] *PlasticsNews*. Current Resin Pricing - Commodity Thermoplastics. 2015.
- [41] Eric O, Mark C. 3D Printing: A Powerful Technology, but No Panacea. *Financial Times*2014.
- [42] Bogue R. 3D printing: the dawn of a new era in manufacturing? *Assembly Automation*. 2013;33(4):307-11.
- [43] Tymrak BM, Kreiger M, Pearce JM. Mechanical properties of components fabricated with open-source 3-D printers under realistic environmental conditions. *Materials & Design*. 2014;58:242-6.
- [44] Warren KC, Lopez-Anido RA, Freund AL, Dagher HJ. Resistance welding of glass fiber reinforced PET: Effect of weld pressure and heating element geometry. *Journal of Reinforced Plastics and Composites*. 2016;35(12):974-85.

- [45] Pocius AV. Adhesion and adhesives technology: an introduction: Carl Hanser Verlag GmbH Co KG; 2012.
- [46] Brinson HF, Brinson LC. Polymer Engineering Science and Viscoelasticity: An Introduction: Springer US; 2015.
- [47] ASTM. D2990-09. Standard Test Methods for Tensile, Compressive, and Flexural Creep and Creep-Rupture of Plastics
- [48] ASTM. D6641/D6641M. Standard Test Method for Compressive properties of Polymer Matrix Composite Materials Using a Combined Loading Compression (CLC) Test Fixture.
- [49] ASTM. D7078/D7078M-12. Standard Test Method for Shear Properties of Composite Materials by V-Notched Rail Shear Method.
- [50] Gibson LJ, Ashby MF. Cellular solids: structure and properties: Cambridge university press; 1999.
- [51] ASTM. E1640-13. Standard Test Method for Assignment of the Glass Transition Temperature By Dynamic Mechanical Analysis
- [52] Herzog B, Gardner DJ, Lopez-Anido R, Goodell B. Glass-transition temperature based on dynamic mechanical thermal analysis techniques as an indicator of the adhesive performance of vinyl ester resin. *Journal of applied polymer science*. 2005;97(6):2221-9.
- [53] Davids WG, Landis EN, Vasic S. Lattice models for the prediction of load-induced failure and damage in wood. *Wood and fiber science*. 2007;35(1):120-34.
- [54] Landis EN, Vasic S, Davids WG, Parrod P. Coupled experiments and simulations of microstructural damage in wood. *Experimental mechanics*. 2002;42(4):389-94.
- [55] Ashby M. The properties of foams and lattices. *Philosophical Transactions of the Royal Society of London A: Mathematical, Physical and Engineering Sciences*. 2006;364(1838):15-30.
- [56] Hanagud S, Craig J, Sriram P, Zhou W. Energy absorption behavior of graphite epoxy composite sine webs. *Journal of Composite Materials*. 1989;23(5):448-59.
- [57] Black S. Reinforced thermoplastics in aircraft primary structure. *Composites World*, 2011.

APPENDIX :

MATLAB PROGRAM FILES USED FOR ANALYSIS

All the files used for this study can be found in the server at Advanced Structures and Composites Center, University of Maine. The codes written in Matlab along with the tasks they perform are written below.

1. CompressionC1.m

This matlab script reads the output generated by ARAMIS DIC system for compression test carried out in C1 direction (material Z-axis perpendicular perpendicular to the direction of loading) and calculates the strength, elastic modulus, and the COVs for these values. This script also plots the stress vs strain curves C1 direction samples.

2. CompressionC3.m

This matlab script reads the output generated by ARAMIS DIC system for compression test carried out in C3 direction (material z-axis parallel to the direction of loading) and calculates the strength, elastic modulus, and the COVs for these values. This script also plots the stress vs strain curves C3 direction samples.

3. TensionT1.m

This matlab script reads the output generated by ARAMIS DIC system for tension test carried out in T1 direction (material z-axis perpendicular to the direction of loading) and calculates the strength, elastic modulus, and the COVs for these values. This script also plots the stress vs strain curves T1 direction samples.

4. TensionT3.m

This matlab script reads the output generated by ARAMIS DIC system for tension test carried out in T3 direction (material z-axis parallel to the direction of loading and calculates the strength, elastic modulus, and the COVs for these values. This script also plots the stress vs strain curves T3 direction samples.

5. ShearS1.m

This matlab script reads the output generated by ARAMIS DIC system for shear test carried out in S1 direction (material unit cell x-axis parallel to loading) and calculates the strength, elastic modulus, and the COVs for these values. This script also plots the stress vs strain curves S1 direction samples.

6. ShearS2.m

This matlab script reads the output generated by ARAMIS DIC system for shear test carried out in S2 direction (material unit cell y-axis parallel to the loading) and calculates the strength, elastic modulus, and the COVs for these values. This script also plots the stress vs strain curves S2 direction samples.

7. ShearS3.m

This matlab script reads the output generated by ARAMIS DIC system for shear test carried out in S3 direction (material unit cell z-axis parallel to the loading) and calculates the strength, elastic modulus, and the COVs for these values. This script also plots the stress vs strain curves S3 direction samples.

8. CompressionC3Solid.m

This matlab script reads the output generated from ARAMIS DIC system for compression test carried out on samples with solid fill. It calculates the strength, elastic modulus, and the COVs for these values. This script also plots the stress vs strain curves for these samples.

9. DMTAslow.m

This matlab script reads the output from the TA800 DMTA equipment for DMTA tests carried out on the filaments. It also calculates the glass transition temperatures based on storage modulus, loss modulus, and tan delta for each sample. An average of these values for the samples and a COV is also calculated. This script also plots the storage modulus, loss modulus, and tan delta values vs temperature for all of the samples.

10. filament_tension_tests.m

This matlab script reads the output from tension tests carried out on filaments of ULTEM 9085 material. It calculates offset strength, and elastic modulus for the samples. It computes the mean of these values and the COVs for each of the value. It plots the stress vs strain curves for each of the samples.

11. creepCompression.m

This matlab script reads the output from the setup created for the creep tests. It reads the files, calculates the time when loading is switched to load control and uses the data after that time to plot the strain vs time plot for creep.

12. Abaqus_calcute_poissions_C_x.m

This script reads the strain outputs in X and Z direction from the file generated from abaqus and uses these strains to calculate the Poisson's ratio in X direction.

13. Abaqus_shear_X.m

This matlab script reads the output file from abaqus with shear strain values YZ plane and calculates the average shear strain from these values.

14. Abaqus_shear_Z.m

This matlab script reads the output file from abaqus with shear strain values in XZ plane and calculates the average shear strain from these values.

BIOGRAPHY OF THE AUTHOR

Sunil Bhandari was born in Nepal on August 15, 1989. He grew up in different cities in Nepal including Pokhara and Kathmandu. He graduated from Budhanilkantha School, Kathmandu, Nepal in 2007. He attended Pulchowk Campus, Institute of Engineering, Tribhuvan University in Nepal from 2008 to 2012. He graduated with a Bachelor's Degree in Civil Engineering in 2012. He started his graduate studies at the University of Maine in the fall of 2014. He is a candidate for the Master of Science degree in Civil Engineering from the University of Maine in May 2017.